SANDIA REPORT

SAND97-0788 • UC-721
Unlimited Release
Printed May 1997

INTRAVAL Phase 2 WIPP 1 Test Case Report: Modeling of Brine Flow Through Halite at the Waste Isolation Pilot Plant Site

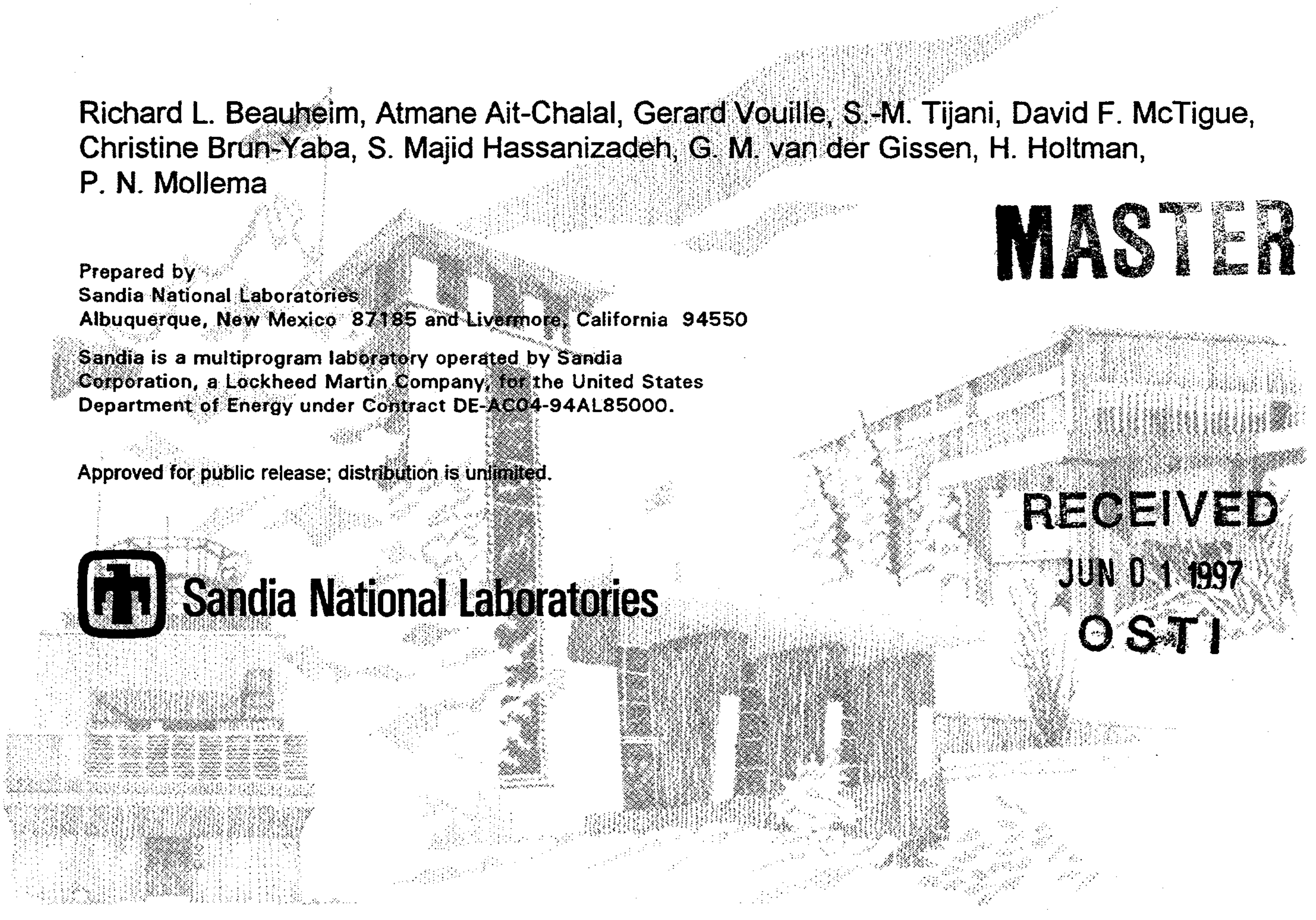

Richard L. Beauheim, Atmane Ait-Chalal, Gerard Vouille, S.-M. Tijani, David F. McTigue, Christine Brun-Yaba, S. Majid Hassanizadeh, G. M. van der Gissen, H. Holtman, P. N. Mollema

Prepared by
Sandia National Laboratories
Albuquerque, New Mexico 87185 and Livermore, California 94550

Sandia is a multiprogram laboratory operated by Sandia Corporation, a Lockheed Martin Company, for the United States Department of Energy under Contract DE-AC04-94AL85000.

Sandia National Laboratories

Issued by Sandia National Laboratories, operated for the United States Department of Energy by Sandia Corporation.

Available to DOE and DOE contractors from
Office of Scientific and Technical Information
P.O. Box 62
Oak Ridge, TN 37831

Prices available from (615) 576-8401, FTS 626-8401

Available to the public from
National Technical Information Service
U.S. Department of Commerce
5285 Port Royal Rd
Springfield, VA 22161

NTIS price codes
Printed copy: A06
Microfiche copy: A01

DISCLAIMER

SAND97-0788
Unlimited Release
Printed May 1997

Distribution
Category UC-721

INTRAVAL Phase 2 WIPP 1 Test Case Report: Modeling of Brine Flow through Halite at the Waste Isolation Pilot Plant Site

Richard L. Beauheim, Editor

Contributors:

Atmane Aït-Chalal, Gerard Vouille, and S.-M. Tijani
École Nationale Supérieure des Mines de Paris
Centre de Géotechnique et d'Exploitation du Sous-Sol
Fontainebleau, France

Richard L. Beauheim
Sandia National Laboratories
Geohydrology Department
Albuquerque, New Mexico, USA

David F. McTigue
University of Washington
Department of Geological Sciences
Seattle, Washington, USA

Christine Brun-Yaba
Commissariat à l'Energie Atomique
Institut de Protection et de Sûreté Nucléaire
Fontenay-aux-Roses, France

S. Majid Hassanizadeh
National Institute of Public Health and Environmental Protection
Bilthoven, the Netherlands

G.M. van der Gissen, H. Holtman, and P.N. Mollema
Utrecht University
Institute of Earth Sciences
Utrecht, the Netherlands

HH

ABSTRACT

This report describes the WIPP 1 test case studied as part of INTRAVAL, an international project to study validation of geosphere transport models. The WIPP 1 test case, analyzed by teams from the Netherlands (National Institute of Public Health and Environmental Protection [RIVM]), France (École Nationale Supérieure des Mines de Paris [EdM]), and the USA (Sandia National Laboratories [SNL]), involved simulation of measured brine-inflow rates to boreholes drilled into the halite strata surrounding the Waste Isolation Pilot Plant repository. The goal of the test case was to evaluate the use of Darcy's law to describe brine flow through halite. The general approach taken was to try to obtain values of permeability and specific capacitance that would be: (1) consistent with other available data and (2) able to provide reasonable simulations of *all* of the brine-inflow experiments performed in the Salado Formation.

All of the teams concluded that the average permeability of the halite strata penetrated by the holes was between approximately 10^{-22} and 10^{-21} m^2. The EdM team identified a single value of specific capacitance, 6.7×10^{-11} Pa^{-1}, from fitting to one set of brine-inflow data, and used that value to simulate the other brine-inflow tests. The RIVM team also used a single value of specific capacitance, 3.0×10^{-11} Pa^{-1}, to simulate the brine-inflow experiments. The SNL team found individual values of specific capacitance from each of the brine-inflow experiments ranging from 2.6×10^{-12} to 3.9×10^{-9} Pa^{-1}. Specific capacitances greater than 10^{-10} Pa^{-1} are inconsistent with the known constitutive properties of halite and are attributed to deformation, possibly ongoing, of the halite around the WIPP excavations.

All project teams found that Darcy-flow models could replicate the experimental data in a consistent and reasonable manner. Discrepancies between the data and simulations are attributed to inadequate representation in the models of processes modifying the pore-pressure field in addition to the experiments themselves, such as ongoing deformation of the rock around the excavations. Therefore, the conclusion from the test case is that Darcy-flow models can reliably be used to predict brine flow to WIPP excavations, provided that the flow modeling is coupled with measurement and realistic modeling of the pore-pressure field around the excavations. This realistic modeling of the pore-pressure field would probably require coupling to a geomechanical model of the stress evolution around the repository.

ACKNOWLEDGMENTS

The editor would like to thank Majid Hassanizadeh, Peter Bogorinski, Kurt Larson, and Peter Davies for their helpful review comments. The contributions of all other members of the INTRAVAL (Salt) Working Group 3 are also acknowledged. The assistance of Rick Bower and Tim Peterson with manuscript preparation is appreciated.

CONTENTS

1. INTRODUCTION 1

2. SITE DESCRIPTION 3

3. TEST CASE DESCRIPTION 9
   3.1 Small-Scale Brine-Inflow Experiments 11
      3.1.1 Description of the DBT Boreholes 11
      3.1.2 Description of the L4 Boreholes 13
   3.2 Pore-Pressure and Permeability Tests 15
   3.3 Integrated Large-Scale Experiments in Room Q 16
   3.4 Validation Issues 18

4. ANALYSES OF SMALL-SCALE BRINE-INFLOW EXPERIMENTS 21
   4.1 RIVM Project Team 21
      4.1.1 Modeling Purpose/Strategy 21
      4.1.2 Codes Used 23
      4.1.3 Modeling Approach 27
      4.1.4 Results 33
      4.1.5 Problem Areas 38
   4.2 EdM Project Team 42
      4.2.1 Modeling Purpose/Strategy 42
      4.2.2 Modeling Approach 44
      4.2.3 Code Used 48
      4.2.4 Results 51
      4.2.5 Problem Areas 59
   4.3 SNL Project Team 60
      4.3.1 Modeling Purpose/Strategy 61
      4.3.2 Code Used 61
      4.3.3 Modeling Approach 63
      4.3.4 Results 75
      4.3.5 Problem Areas 93
   4.4 Comparison and Summary of Project Teams' Interpretations 96

5. SUMMARY 101
   5.1 Status of Validation Issues 101
   5.2 Recommendations 102
   5.3 Conclusions 103

6. REFERENCES 105

Figures

2-1 Location of the WIPP site. 4
2-2 WIPP area stratigraphic column. 5
2-3 Detailed stratigraphy near the WIPP underground facility. 6
2-4 Schematic of typical WIPP underground rooms showing stratigraphic positions 8

3-1 Map of the WIPP underground facility showing test locations. 10
3-2 DBT boreholes brine-inflow rate: DBT10 to DBT13. 14
3-3 Plots of brine-inflow rate to L4B01 and L4X01. 15
3-4 As-built profile of Room Q with inferred stratigraphy. 17
3-5 Stratigraphic locations of test boreholes 19

4-1 Sensitivity of brine inflow to the distance to a constant-pressure boundary. 30
4-2 Sensitivity of brine inflow to the initial pore pressure. 31
4-3 Sensitivity of brine inflow to permeability. 32
4-4 Sensitivity of brine inflow to specific capacitance. 32
4-5 Comparison of observed and RIVM-calculated flow rates and volumes of borehole DBT10 for a period of 1000 days. 34
4-6 Comparison of observed and RIVM-calculated flow rates and volumes of borehole DBT11 for a period of 1000 days. 35
4-7 Comparison of observed and RIVM-calculated flow rates and volumes of borehole DBT12 for a period of 1000 days. 36
4-8 Comparison of observed and RIVM-calculated flow rates and volumes of borehole DBT13 for a period of 1000 days. 37
4-9 Mesh used for RIVM calculation of pressure distribution around the room 40
4-10 Distribution of pressure along a line perpendicular to the room wall after 10 years. 40
4-11 Change of pressure with time at various distances from the room wall. 41
4-12 Approximation of equipotential lines beneath Room D 43
4-13 Boundary conditions of the first calculation 45
4-14 Boundary conditions of the second calculation 46
4-15 First model mesh 50
4-16 Second model mesh 50
4-17 Average value of flow in DBT13 steady-state system 52
4-18 K_2 as a function of K_1 54
4-19 Comparison of observed and EdM-calculated flow rates and volumes of borehole DBT10 for a period of 1000 days. 56
4-20 Comparison of observed and EdM-calculated flow rates and volumes of borehole DBT11 for a period of 1000 days. 57
4-21 Comparison of observed and EdM-calculated flow rates and volumes of borehole DBT13 for a period of 1000 days. 58
4-22 Calculated hydraulic head beneath the room as a function of vertical position 60
4-23 Definition sketch for radial flow to a borehole. 66

Figures (Continued)

4-24 Pore pressure profiles at various times based on Eq. 4-33 radial coordinate, *r*, is normalized by borehole radius, *a*; pressure, *p*, is normalized by initial value p_∞. 69

4-25 Comparison of late-time approximations (Eq. 4-42) and “exact” solution (Eq. 4-48) for fluid flux at a borehole; time, *t*, is normalized by characteristic diffusion time, a^2/c; flux, $^3q_r^3(a,t)$, is normalized by $q_0 = kp_\infty/\mu a$ 73

4-26 Comparison of “exact” and late-time, asymptotic solutions for inverse of borehole flux; time, *t*, is normalized by characteristic diffusion time, a^2/c; flux, $^3q_r^3(a,t)$, is normalized by $q_0 = kp_\infty/\mu a$ 74

4-27 Comparison of model fit to data for full flux history, hole DBT10. 77

4-28 Comparison of model fit to data for full flux history, hole DBT11. 77

4-29 Comparison of model fit to data for full flux history, hole DBT12. 78

4-30 Comparison of model fit to data for full flux history, hole DBT13. 78

4-31 Comparison of model fit to data for full flux history, hole L4B01. 79

4-32 Comparison of model fit to data for cumulative volume history, hole DBT10 81

4-33 Comparison of model fit to data for cumulative volume history, hole DBT11 82

4-34 Comparison of model fit to data for cumulative volume history, hole DBT12 82

4-35 Comparison of model fit to data for cumulative volume history, hole DBT13 83

4-36 Comparison of model fit to data for cumulative volume history, hole L4B01. 83

4-37 Comparison of model fit to data for late-time flux, hole DBT10. Points included in linear regression are shaded. 84

4-38 Comparison of model fit to data for late-time flux, hole DBT11. Points included in linear regression are shaded. 84

4-39 Comparison of model fit to data for late-time flux, hole DBT12. Points included in linear regression are shaded. 85

4-40 Comparison of model fit to data for late-time flux, hole DBT13. Points included in linear regression are shaded. 85

4-41 Comparison of model fit to data for late-time flux, hole L4B01. Points included in linear regression are shaded. 86

4-42 Comparison of model fit to data for late-time flux, hole L4X01. Points included in linear regression are shaded. 86

4-43 Comparison of permeability values determined by various methods. Perfect correlations lie on the solid line. 94

4-44 Comparison of capacitance values determined by various methods. Perfect correlations lie on the solid line line. 94

Tables

3-1 Construction Information for Vertical Boreholes DBT 10, 11, 12 and 13 12
3-2 Strata Intersected by Borehole DBT10 12
3-3 Strata Intersected by Borehole DBT11 12
3-4 Strata Intersected by Borehole DBT12 13
3-5 Strata Intersected by Borehole DBT13 13

4-1 Parameters Used for RIVM Simulations 23
4-2 Brine-Inflow Rate after 1000 Days Calculated with Different Mesh Lengths 29
4-3 Measured and Calculated Amounts of Brine Inflow 38
4-4 Parameters Derived from Fits to Full Flux Through January 1990 79
4-5 Parameters Derived from Fits to Cumulative Volume 81
4-6 Parameters Derived from Fits to Late-Time Flux 87
4-7 Diffusion Length Scales for Various Diffusivities 90
4-8 Parameters for DBT10 by Various Fitting Schemes 92
4-9 Elastic Properties of Salt and Brine 95
4-10 Comparison of Permeabilities Calculated by Different Teams 98
4-11 Comparison of Specific Capacitances Calculated by Different Teams 99

NOTATION

The following notation is used for variables in equations in Chapter 4. In some cases, additional subscripts are used to denote specific times or conditions.

B = source term in Skempton's coefficient

b = thickness of bed or tested interval (L)

C_s = specific capacitance (LT^2/M)

c = hydraulic diffusivity (L^2/T)

c_f = fluid or brine compressibility (LT^2/M)

c_m = rock or media compressibilty (LT^2/M)

G = shear modulus (M/LT^2)

$\mathbf{g}$ = gravity vector (L/T^2)

h = head change in tested formation (L)

J_0 = Bessel function of first kind, zero order

K = hydraulic conductivity (L/T)

K_f = bulk modulus of fluid (M/LT^2)

K_m = bulk modulus (drained) (M/LT^2)

K_s = bulk modulus of solid grains (M/LT^2)

$\mathbf{k}$ = permeability tensor

k = permeability (L^2)

L_D = diffusion length (L)

p = pressure (M/LT^2)

p_∞ = boundary or initial pressure (M/LT^2)

Q = mass balance source term

$\mathbf{q}$ = Darcy flux velocity vector (L/T)

$\mathbf{q}_{\mathbf{borehole}}$ = steady-state brine flux to borehole (L/T)

r_i = radius of influence (L)

r_w = radius of well (L)

S_s = specific storage (I/L)

t = time (T)

$\mathbf{v}_f$ = fluid velocity (L/T)

$\mathbf{v}_s$ = solid skeleton velocity (L/T)

Y_0 = Bessel function of second kind, zero order

z = depth (L)

β = exp(γ)

γ = Euler's constant

ε = volumetric strain

ϕ = porosity

γ_f = material density of fluid (M/L^3)

γ_s = material density of solid (M/L^3)

μ = fluid or brine viscosity (M/LT)

ν_s = dilation rate (L/T)

ρ = brine or fluid density (M/L^3)

ρ_f = partial density (M/L^3)

ρ_r = brine or fluid reference density (M/L^3)

ρ_0 = total density (M/L^3)

σ_0 = reference mean total stress (M/LT^2)

υ = Poisson ratio

1. INTRODUCTION

INTRAVAL is a cooperative international project organized to evaluate conceptual and mathematical models of groundwater flow and radionuclide transport used in performance assessment of radioactive waste repositories. The purpose of the INTRAVAL project is to increase understanding of how mathematical models can describe various geophysical, geohydrological, and geochemical phenomena that may affect radionuclide transport from a repository to the biosphere. The INTRAVAL studies use information from laboratory tests, field experiments, and natural analog studies as input for mathematical models, which are used to validate the underlying conceptual models and study the model validation process. INTRAVAL supports interaction between modelers and experimentalists.

The INTRAVAL studies began in October 1987. The first three-year study, Phase 1, is completed. The second three-year study, Phase 2, began in October 1990. Eleven test cases are included in Phase 2. This report describes one test case, WIPP 1, which is based on tests conducted at the Waste Isolation Pilot Plant (WIPP) in New Mexico, USA. These tests, analyzed by three international teams, involved measurement of brine-inflow rates to boreholes drilled into the halite strata surrounding the WIPP repository. Several modeling strategies were used by the different project teams. The pilot group at Sandia National Laboratories (SNL) used an analytical solution coupled with a parameter-estimation code. The (Dutch) National Institute of Public Health and Environmental Protection (RIVM) used the METROPOL-2 code. The (French) École Nationale Supérieure des Mines de Paris (EdM) used a two-stage mathematical modeling technique employing the HYDREF code. The EdM worked under the auspices of the Commissariat à l'Energie Atomique/Institut de Protection et de Sûreté Nucléaire (CEA/IPSN).

This report describes the work and conclusions of the three teams that studied the WIPP 1 test case. Chapter 2 provides a brief description of the geologic setting of the WIPP site. Chapter 3 summarizes the data provided for the test case. Chapter 4 presents the work performed by the three teams that studied the small-scale brine-inflow experiments. Chapter 5 summarizes the final status of the validation issues associated with the test case, provides recommendations for further work, and presents the conclusions derived from the work.

This page intentionally left blank.

2. SITE DESCRIPTION

The WIPP is a U.S. Department of Energy research and development facility designed to demonstrate safe disposal of transuranic wastes from the United States' defense programs. The WIPP site is located in the northern part of the Delaware Basin in southeastern New Mexico, USA (Figure 2-1). WIPP-site geologic investigations have concentrated on seven of the formations typically found in that part of the Delaware Basin. These are, in ascending order, the Bell Canyon, the Castile Formation, the Salado Formation, the Rustler Formation, the Dewey Lake Redbeds, the Dockum Group, and the Gatuña Formation (Figure 2-2). All of these formations are of Permian age, except for the Dockum Group, which is Triassic age, and the Gatuña, which is a Quaternary deposit. The WIPP underground facility lies in the lower part of the Salado Formation at an approximate depth of 655 m below ground surface.

The Salado Formation is approximately 600 m thick at the WIPP site and is composed largely of halite, with minor amounts of interspersed clay and polyhalite. Some zones in the upper part of the Salado are rich in potassium minerals such as sylvite and langbeinite. The Salado also contains interbeds of anhydrite, polyhalite, clay, and siltstone. Many of these interbeds are traceable over most of the Delaware Basin. Jones et al. (1973) designated 45 of the continuous anhydrite and/or polyhalite interbeds as "Marker Beds" and numbered these Marker Beds from 100 to 144, increasing downward. Stratigraphically, the WIPP facility horizon lies between Marker Beds 138 and 139.

A typical stratigraphic section of the Salado Formation in the vicinity of the WIPP underground facility, adapted from Deal et al. (1989), is shown in Figure 2-3. Deal et al. (1989) present a detailed description of stratigraphic units that correlate throughout most of the underground facility. The description covers a 41.2-m interval of the Salado, centered approximately at the stratigraphic midpoint of the excavations. This description delineates 16 "map units" numbered 0 to 15, as well as 23 other map units. The majority of the units are composed primarily of halite and are differentiated principally on the basis of differing clay and polyhalite contents. The halite units lacking integer map-unit designations are identified by H (pure halite), AH (argillaceous halite), or PH (polyhalitic halite) prefixes, followed by a number

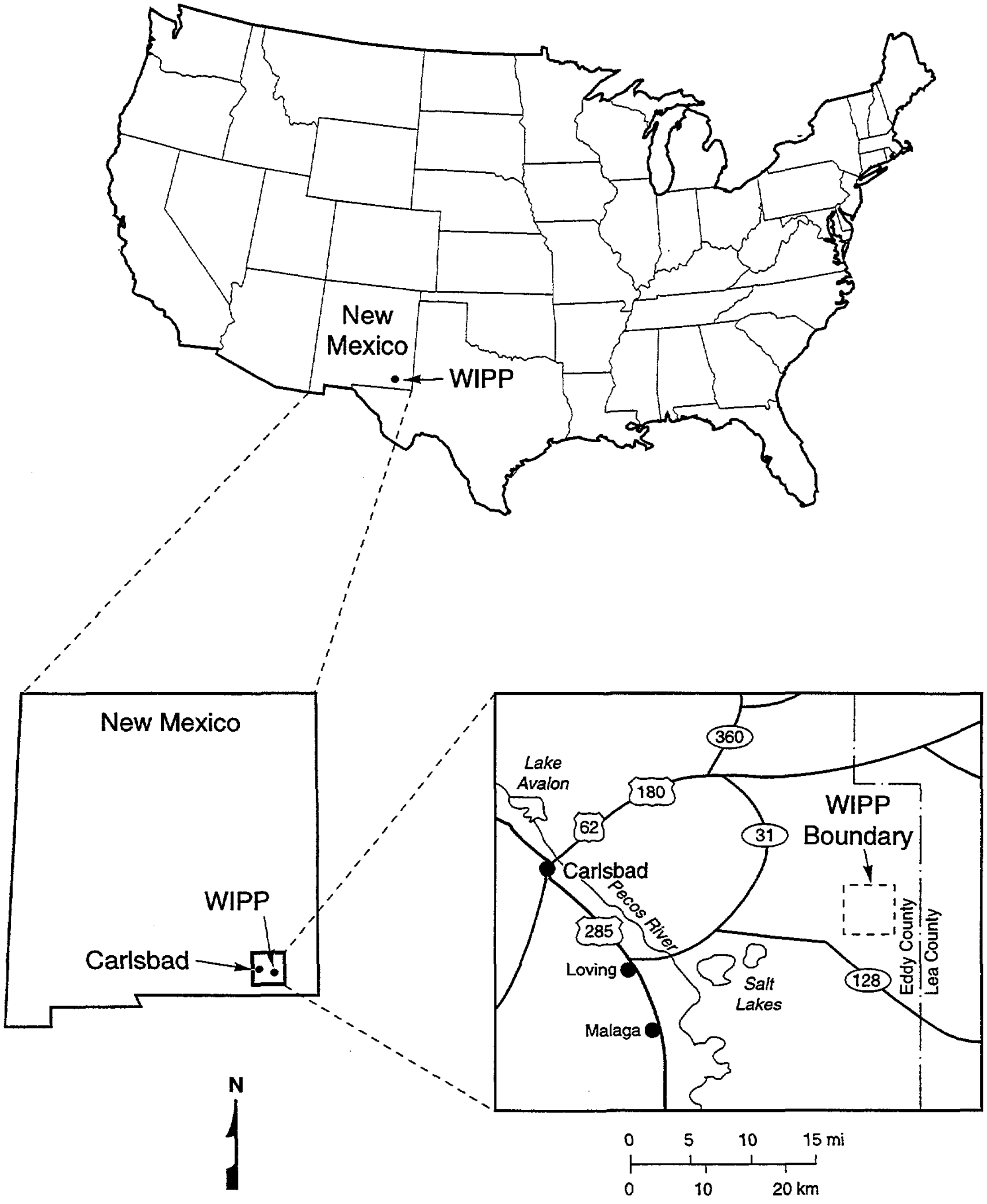

TRI-6330-3-5

Figure 2-1. Location of the WIPP site.

System	Series	Group	Formation	Member	Approximate Thickness (m)*
Recent	Recent		Surficial Deposits		3
Quaternary	Pleistocene		Mescalero Caliche		10
			Gatuña		
Triassic		Dockum	Undivided		3
Permian	Ochoan		Dewey Lake Red Beds		150
			Rustler	Forty-niner	18
				Magenta Dolomite	7
				Tamarisk	26
				Culebra Dolomite	7
				unnamed	37
			Salado		600
			Castile		400
	Guadalupian	Delaware Mountain	Bell Canyon		310
			Cherry Canyon		335
			Brushy Canyon		550

* At center of WIPP site.

TRI-6115-38-0

Figure 2-2. WIPP area stratigraphic column.

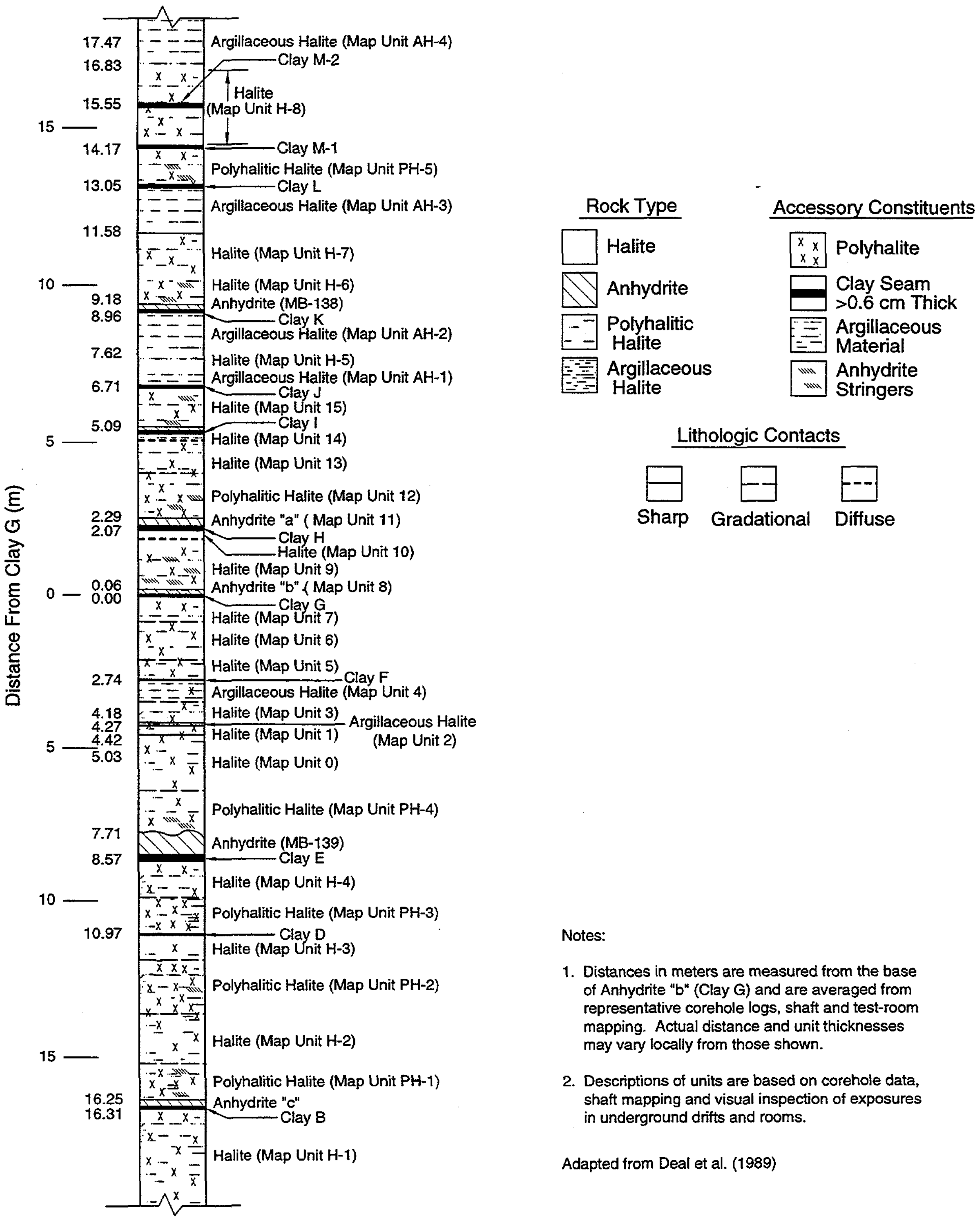

Notes:

1. Distances in meters are measured from the base of Anhydrite "b" (Clay G) and are averaged from representative corehole logs, shaft and test-room mapping. Actual distance and unit thicknesses may vary locally from those shown.
2. Descriptions of units are based on corehole data, shaft mapping and visual inspection of exposures in underground drifts and rooms.

Adapted from Deal et al. (1989)

TRI-6119-346-0

Figure 2-3. Detailed stratigraphy near the WIPP underground facility.

representing that unit's position with respect to the base of the sequence, which was arbitrarily defined as the halite unit immediately underlying anhydrite "c" and clay B. For example, AH-4 is the fourth argillaceous halite unit above the base of the sequence. The remainder of the units is made up of anhydrite interbeds such as Marker Beds 138 and 139. Thinner anhydrite interbeds and several of the more continuous clay seams have also been given letter designations (e.g., anhydrite "a," clay B) to facilitate consistent referencing. These units and the stratigraphic positions of the excavations with respect to the designated map units are shown in Figure 2-4.

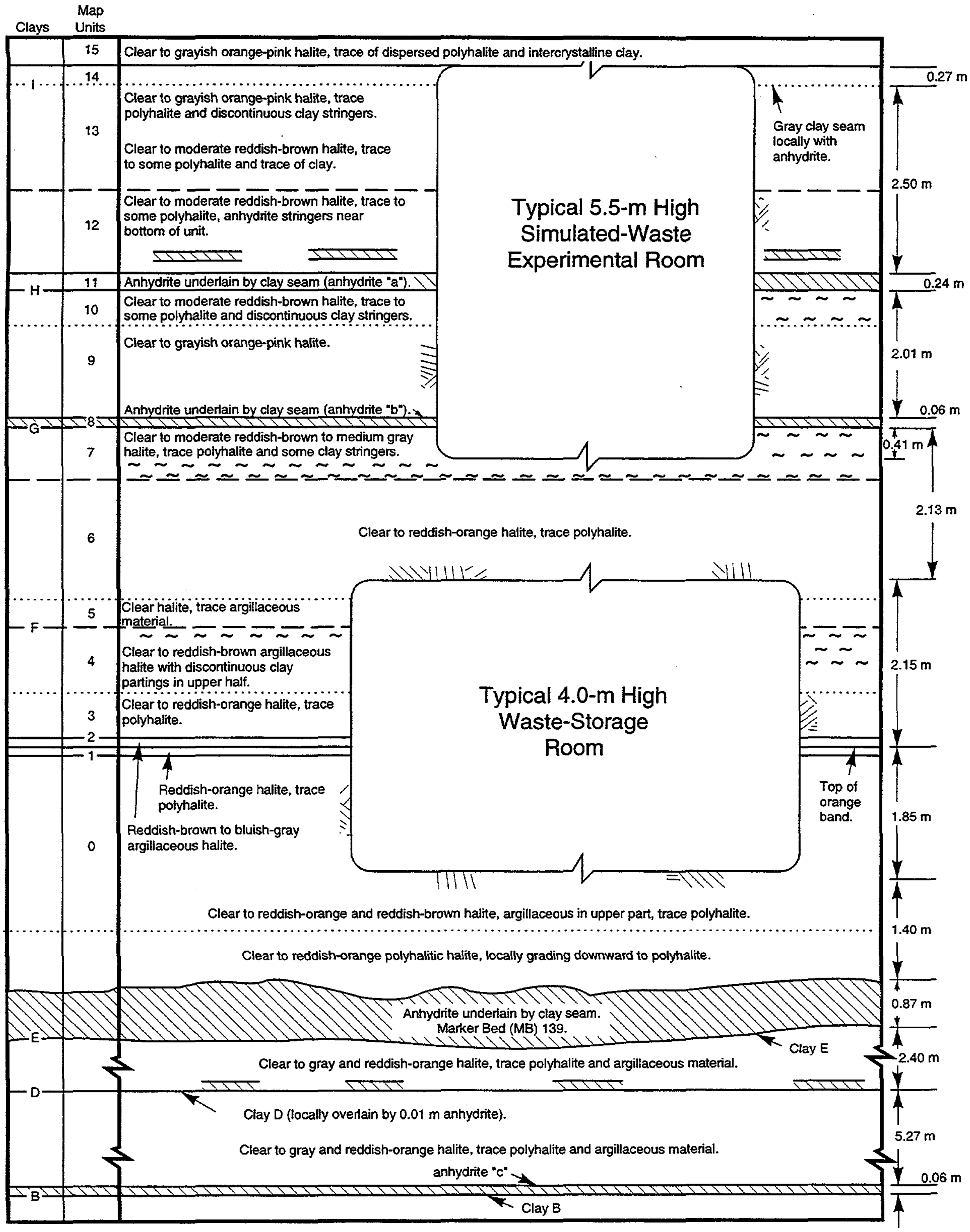

TRI-6334-257-1

Figure 2-4. Schematic of typical WIPP underground rooms showing stratigraphic positions.

3. TEST CASE DESCRIPTION

The WIPP 1 experiments provide data on the hydraulic behavior of the Salado Formation under a variety of testing conditions. The objective of the INTRAVAL test case was to determine whether a Darcy-flow model of brine flow through halite could accurately simulate all the different types of *in situ* tests performed and, therefore, be used to predict reliably the rates and volumes of brine inflow to the WIPP repository. This information is important to the WIPP project because brine availability is an important factor in determining the amount of corrosion of metals and associated generation of gas that might occur following closure of the repository. Gas generation is important because it may control the pressure of the repository at the time of a hypothetical human intrusion and must be considered in designing the seals and plugs to be placed within the repository and shafts.

Data from three types of experiments at three different scales form the basis of the WIPP 1 test case:

- Small-scale brine-inflow experiments
- Pore pressure and permeability tests
- Large-scale brine-inflow experiments (Room Q)

The tests were performed to evaluate formation responses under different conditions. The small-scale brine-inflow experiments were designed to measure the long-term flow of brine from halite to boreholes maintained at atmospheric pressure. The pore-pressure and permeability tests were designed to provide information on pore pressures, permeabilities, and other hydraulic properties at different positions around the repository. The large-scale brine-inflow experiment was designed to provide data on inflow to a room-sized opening in the halite, with supporting data provided by pore-pressure and permeability measurements in the surrounding rock. The locations within the WIPP underground at which the different experiments were performed are shown in Figure 3-1.

The data provided by all the tests are ultimately intended to be taken together to support modeling of the flow of brine between the WIPP repository and surrounding

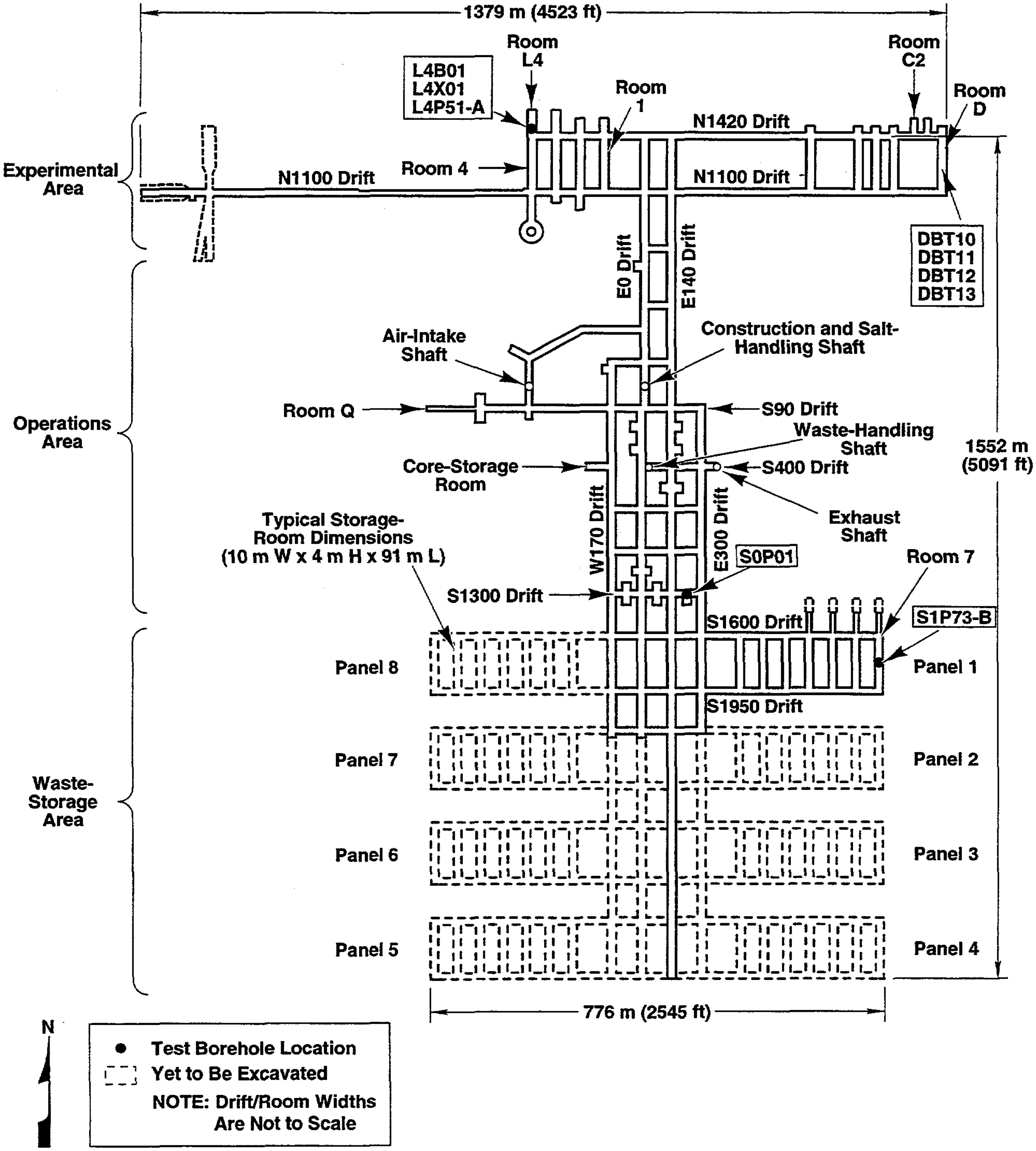

TRI-6330-129-8

Figure 3-1. Map of the WIPP underground facility showing test locations.

formation over a period of 10,000 years for regulatory compliance purposes. The pore-pressure and permeability tests would provide boundary and initial conditions for the modeling, while the small-scale and large-scale brine-inflow experiments would provide data on the output of the system under the experimental conditions. The focus of the WIPP 1 test case is to define an appropriate model for the long-term simulation of brine flow. The data from the tests were given to the test case team members, who selected different subsets of the data as the basis for their individual models.

In the WIPP 1 test case, only the movement of brine in response to pressure gradients was studied. Temperature effects were not taken into account because they are not considered to be of importance around a TRU waste repository such as the WIPP.

3.1 Small-Scale Brine-Inflow Experiments

For the small-scale brine-inflow experiments, boreholes were drilled from the repository into the surrounding halite from Room D (DBT boreholes) and Room L4, and the accumulation of brine seeping into each borehole was measured as a function of time. The boreholes, which were oriented either vertically downward (DBT) or horizontally (L4), were open over their entire span, but each borehole opening was sealed (being opened only for measurements of brine accumulation) to prevent moisture loss through evaporation and air circulation. Humidity measurements were made to aid in quantifying the total moisture entering a borehole. Brine-chemistry data were also obtained.

Data from the boreholes were given to members of the project teams. All three teams modeled the brine-inflow experiments in the vertical (DBT) boreholes. Only the SNL team studied the data from the horizontal (L4) boreholes.

3.1.1 Description of the DBT Boreholes

The WIPP 1 test case data set includes data from four 10-cm boreholes drilled vertically downward: DBT10, DBT11, DBT12, and DBT13. Construction information for these boreholes is presented in Table 3-1, and lithologic data for each are given in

Tables 3-2 through 3-5. The four holes were all drilled to different depths so that the contributions of different layers to flow could be evaluated.

Table 3-1. Construction Information for Vertical Boreholes DBT10, 11, 12, and 13 (after Finley et al., 1992)

Hole Number	Date Drilled to 10-cm Diameter	Total Length (m)*
DBT 10	9/18/87	5.3
DBT 11	9/23/87	4.6
DBT 12	9/22/87	3.7
DBT 13	9/17/87	2.8

*Total length as measured from the drift floor.

Table 3-2. Strata Intersected by Borehole DBT10

Depth (m)	Description	Map Unit
0.00 - 1.41	halite	6
1.41 - 2.05	argillaceous halite	5
2.05 - 3.50	halite	4, 3, 2, 1
3.50 - 4.27	argillaceous halite	0
4.27 - 5.22	halite	0

Table 3-3. Strata Intersected by Borehole DBT11

Depth (m)	Description	Map Unit
0.00 - 1.52	halite	6, 7
1.52 - 2.27	argillaceous halite	5
2.27 - 3.72	halite	4, 3, 2, 1
3.72 - 4.44	argillaceous halite	0

Table 3-4. Strata Intersected by Borehole DBT12

Depth (m)	Description	Map Unit
0.00 - 1.57	halite	6,7
1.57 - 2.29	argillaceous halite	5
2.29 - 3.53	halite	4, 3

Table 3-5. Strata Intersected by Borehole DBT13

Depth (m)	Description	Map Unit
0.00 - 2.41	halite	6,7
2.41 - 2.59	argillaceous halite	5

Brine-inflow measurements in the 10-cm-diameter boreholes generally showed rapidly declining flow rates for the first few months, followed by steady or slowly declining flow rates for periods as long as two years. Initial flow rates ranged from about 5 to 25 g/day, while steady flow rates ranged from about 2 to 10 g/day. Inflow rates into some boreholes began to increase two to three years after the holes were drilled. Plots of the rates of brine inflow to these holes over time are shown in Figure 3-2.

3.1.2 Description of the L4 Boreholes

Both L4B01 and L4X01 are subhorizontal boreholes drilled 5.8 and 5.7 m, respectively, into the argillaceous halite of Map Unit 0 (Finley et al., 1992). L4B01 is a 10-cm-diameter hole and L4X01 is a 90-cm-diameter hole. Plots of the brine-inflow rate versus time for these holes, drilled into argillaceous halite, are shown in Figure 3-3. L4B01 has yielded only about 2 g/day of brine. L4X01 produced as much as 25 g/day during the first few months after it was drilled, but the rate then declined to near zero. The humidity in these holes appears to be in equilibrium with free-standing brine.

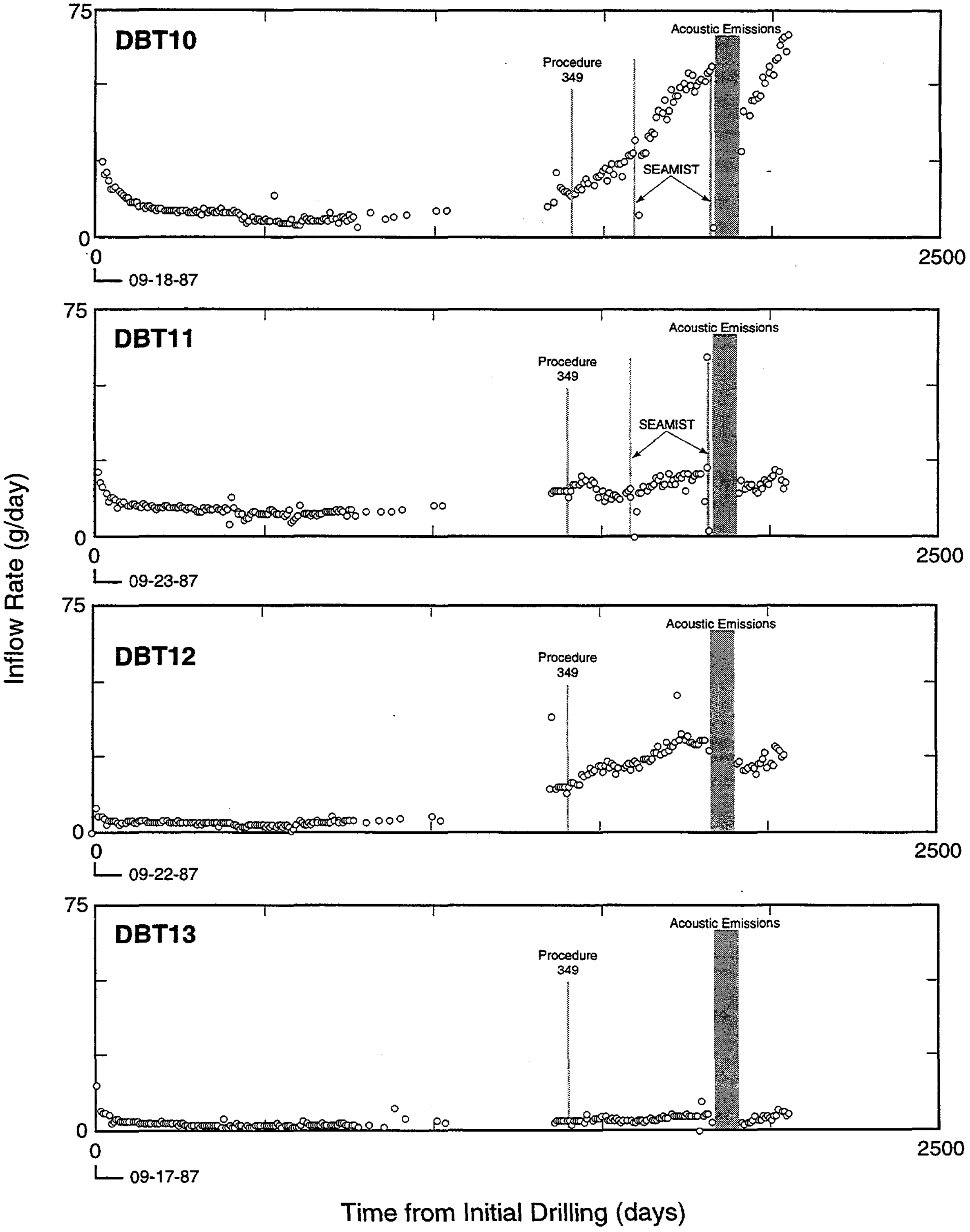

TRI-6119-359-0

Figure 3-2. DBT boreholes brine-inflow rate: DBT10 to DBT13.

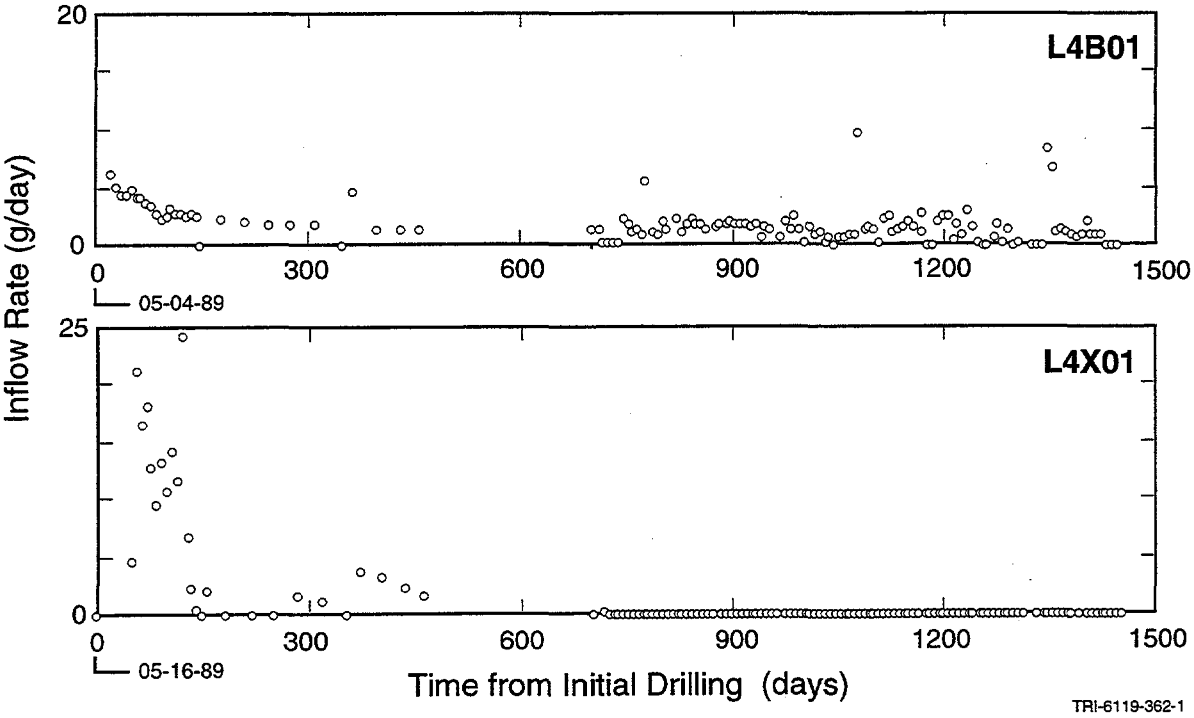

Figure 3-3. Plots of brine-inflow rate to L4B01 and L4X01.

3.2 Pore-Pressure and Permeability Tests

Pore-pressure and permeability tests were conducted with multipacker test tools installed in 10.2-cm-diameter boreholes drilled in a variety of orientations. Pressures were measured in packer-isolated intervals of the boreholes. Factors other than the formation pore pressure that could contribute to fluid pressures observed in a borehole, specifically temperature changes and borehole closure, were also monitored.

Permeability experiments in the 10-cm-diameter boreholes involved pressure-pulse, constant-pressure flow, and pressure-buildup tests. Pressures and temperatures were measured in the test interval between the bottom packer and the bottom of the hole and in the guard zone between the packers of the double-packer test tools. Packer pressure, radial borehole deformation, and borehole elongation were also measured. Flow rates during the constant-pressure flow tests were measured using differential pressure transmitters connected to pressurized vessels of different sizes. All data were collected on computerized data-acquisition systems (DASs).

The lithostatic pressure at the WIPP repository is 14.8 MPa (Krieg, 1984). A depressurized zone exists around the repository. Domski et al. (1996) interpreted pore pressures in the permeability test holes ranging from 0.3 MPa (within 2 m of a room) to 12.5 MPa (at locations farther than 22 m from a room), based on analyses of data collected during the permeability experiments. Stratigraphic heterogeneity and stress relief around the excavation may have significant effects on the pressures observed in the test boreholes.

The WIPP 1 test case includes two sets of permeability and pore-pressure experiments from argillaceous halite layers (test sequences S0P01 and L4P51-A) and one set from an anhydrite layer (S1P73-B). Data from borehole S0P01 allowed modeling of the strata properties in immediate proximity to the waste-disposal horizon from an excavation (South 1300 drift) older than those available in the waste-storage area. Data from borehole L4P51 in Room L4 provided information from a borehole drilled through halite, polyhalitic halite, and clay D underlying Marker Bed 139. Data from borehole S1P73 in Room 7 of Waste Panel 1 furnished information about Marker Bed 138. This last borehole was drilled vertically upward into the roof of the excavation. This location in the waste-storage area was chosen to provide hydraulic information for those portions of the Salado Formation directly affected by the excavations designed for waste storage. These areas generally have been exposed to excavation effects for less time than excavations in other parts of the underground facility.

The data were given to all three teams. No project team other than SNL modeled the data from the three tests; therefore, the permeability tests will not be discussed further in this report. Additional information on the tests and the interpretations performed by SNL can be found in Beauheim et al. (1991, 1993).

3.3 Integrated Large-Scale Experiments in Room Q

The large-scale experiment was conducted in Room Q, a cylindrical room 110 m long and 2.9 m in diameter situated approximately 92 m west-southwest of the Air Intake Shaft in the northern experimental area of the WIPP underground (Figure 3-1). This location represents an isolated, undisturbed area where pre-mining values for pore pressure and fluid flow could be established in a far-field location. The room was bored parallel to bedding in the upper host rock strata of the planned waste disposal stratigraphic interval, using the orange marker band (OMB; map unit 1) as a guide. The crown of Room Q peaks at 2.1 m above the OMB. The room intersects five distinct stratigraphic units, and it slopes slightly upward from front to back (east to west) to follow the natural dip of the bedding, as shown in Figure 3-4. Before Room Q was excavated, three arrays of boreholes (five over, five under, and five beside the planned room) were drilled. The locations of these boreholes relative to Room Q and the rectangular instrumentation alcove adjoining the room are shown in Figure 3-5. These boreholes were instrumented to allow for assessment of pre- and post-mining hydrologic conditions. In isolated test zones within the boreholes (each zone being at a specific radial distance from the centerline of Room Q), data were collected on pore pressure and permeability. Data-collection methods and raw data are found in Jensen et al. (1993a). These data were collected before, during, and after excavation of Room Q. Data sets from four of these holes, QPP03, QPP04, QPP11, and QPP12, were included in the WIPP 1 test case.

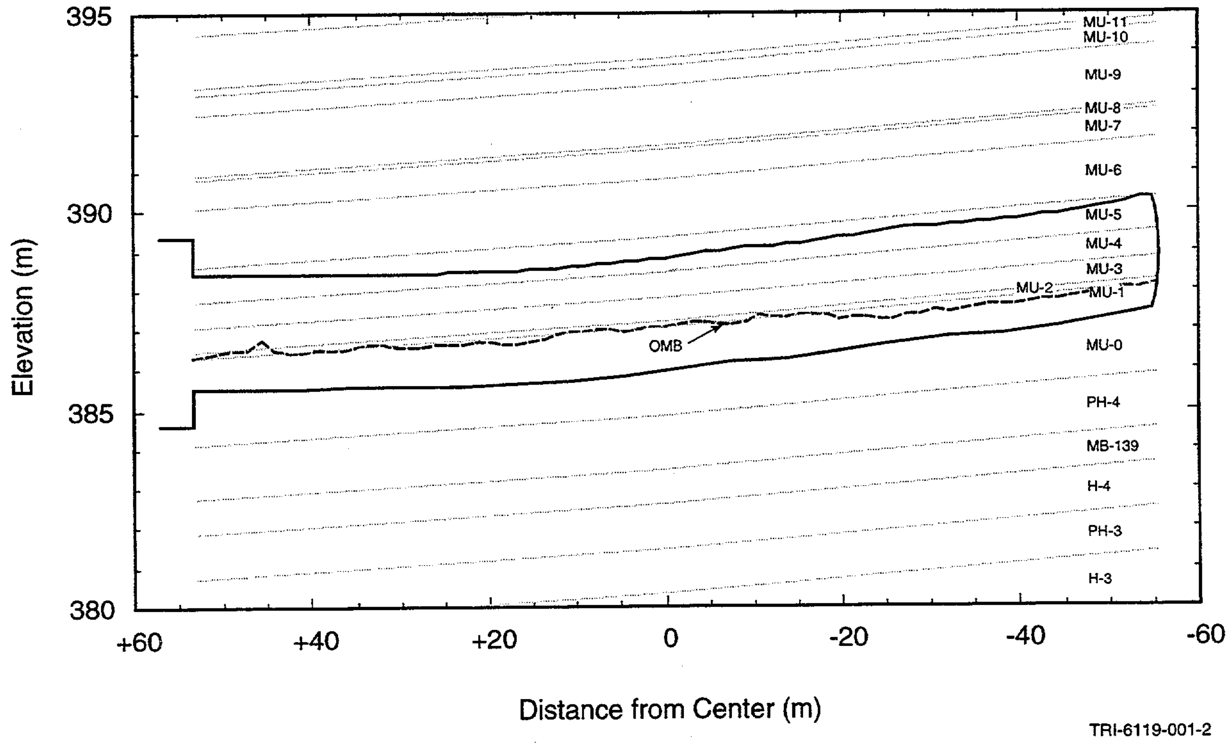

Figure 3-4. As-built profile of Room Q with inferred stratigraphy.

Other data were collected within Room Q. Brine accumulation in the sealed room was measured at three- to six-month intervals. Electrical resistivity changes were monitored around the circumference of the room at several locations, and vertical and horizontal closure of the room was measured at the collar and at three locations within the room. These data are presented in Jensen et al. (1993b).

The Room Q data were given to all INTRAVAL project team members. No project team other than SNL modeled the Room Q data, however, so the Room Q experiments will not be discussed further in this report. The SNL interpretations of the permeability tests conducted in the Room Q boreholes are presented in Domski et al. (1996). Freeze et al. (1997) simulated brine inflow to Room Q, taking formation of a disturbed rock zone around the room into account.

3.4 Validation Issues

The goal of the WIPP 1 test case was to establish the applicability of Darcy's equation or alternative models to describe brine flow through halite under a pressure gradient. This test case examined brine-flow mechanisms at a number of scales, from 10-cm-diameter boreholes to 3-m-diameter rooms. The test case used pressure-transient and flow-transient testing techniques to provide information on different properties of the flow system. The applicability of a Darcy-flow model to evaporites was investigated, with possible refinements suggested dealing with two-phase flow, rock-creep effects, and coupling of fluid pressures to the stress field in the rock mass. The need for alternative models, such as one in which porosity becomes interconnected and brine is squeezed from the salt as a result of creep, was also considered.

Investigation of the appropriateness of a flow model includes identification of all relevant phenomena and quantification of all necessary parameters required by the model. The modeling efforts were expected to identify additional experiments, if any, needed to validate Darcy-flow or alternative models. Once an appropriate flow model is obtained, the WIPP project will use this model to calculate the volumes and rates of brine flow into the repository after it is closed and sealed. Brine availability is an important factor in determining the amount of corrosion of metals and associated

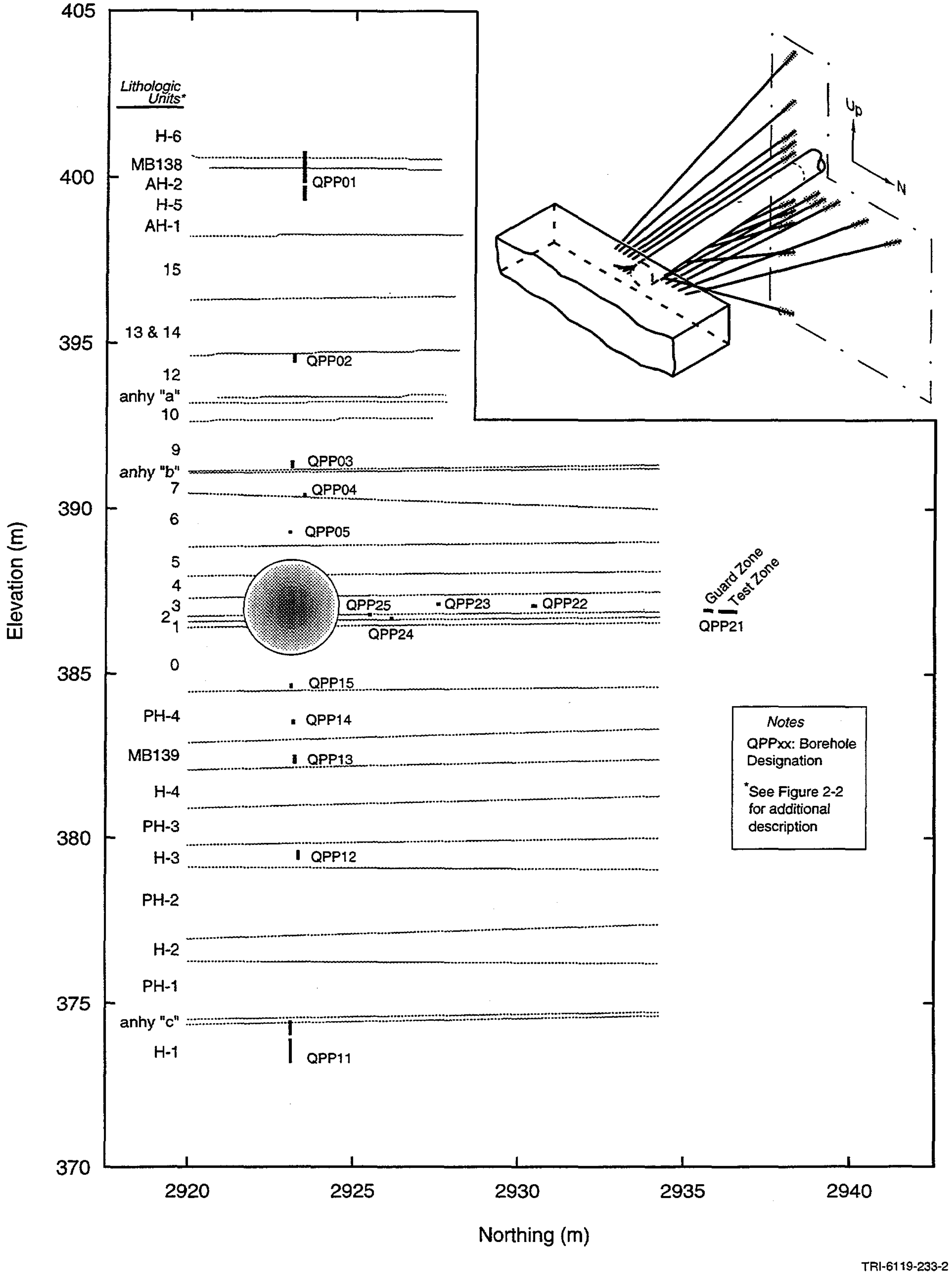

Figure 3-5. Stratigraphic locations of test boreholes.

generation of gas that might occur following closure of the repository. Gas generation is important because it may control the pressure of the repository at the time of a hypothetical human intrusion and must be considered in designing the seals and plugs to be placed within the repository and shafts. Consequently, the flow model will be coupled with gas-generation models and a geomechanical model of the excavation and host-rock response to understand and predict the overall repository performance.

4. ANALYSES OF SMALL-SCALE BRINE-INFLOW EXPERIMENTS

Brine-inflow data from boreholes DBT10, DBT11, DBT12, DBT13, L4B01, and L4X01 formed the data set for these analyses. The small-scale brine-inflow experiments were terminated in May 1993. Symbols and notation used in this report are identified in Section 6.

4.1 RIVM Project Team

The RIVM study of the small-scale brine-inflow experiments was originally reported by Hassanizadeh et al. (1994). The following sections are abstracted from that report.

4.1.1 Modeling Purpose/Strategy

Model calibration, also referred to as parameter estimation, history-matching, or solution of the inverse problem, is a notoriously difficult but vitally important stage in numerical modeling. An indirect approach was followed in the RIVM study by using an iterative procedure. An appropriate distribution of the hydrologic parameters, such as the permeability and storage coefficient, and the initial and boundary conditions were sought such that a satisfactory fit of the model calculations to experimental observations could be obtained. The calibration procedure began with an initial simulation using trial estimate of the unknown parameters. The parameters were then modified in successive simulations until the desired convergence in the fit was achieved. Finally, a sensitivity analysis was performed to see how the simulation results were influenced by variations in the values of certain parameters.

The main objective of the modeling exercise was to establish the applicability of Darcy's law in describing movement of brine in rock salt under a pressure gradient. Obviously, many simplifications and assumptions made in the first phase of study resulted in inaccurate predictions. Nevertheless, a systematic agreement between model calculations and experimental data was expected.

A simplified stratigraphy was represented for each of the brine-inflow boreholes, based on the detailed core logging performed. The strata were divided into two types, pure halite and argillaceous halite. Each type was considered to be homogeneous and to have the same hydraulic properties at all of the boreholes. The amount of brine inflow at each borehole was attributed to the relative percentages of the two rock types and the total length of the hole. Given that the boundary conditions, layer configurations, and the magnitude of driving forces vary among these experiments, a satisfactory simulation of all or most observed data would give an indication of the applicability of Darcy's law.

Model parameters were evaluated by fitting calculations to data from borehole DBT11, and then, using the same set of parameters, other inflow experiments were simulated. The DBT11 data were chosen for initial calculations because the measurements of brine inflow give a smooth curve with relatively few erratic data (Figure 3-2). The strata intersected by the borehole were treated as four individually homogeneous layers (see Table 3-3).

Parameters to be determined included initial pressure distribution, far-field pressure, brine density, viscosity, brine compressibility, rock compressibility, porosity, and permeability of the two types of layers. Values of some of these parameters are well defined under the repository conditions. For example, density, viscosity, and brine compressibility are known at the prevailing temperature and pressure values, and rock elastic moduli are fairly accurately determined by direct experiments. Major sources of uncertainty are initial pressure distribution, porosity, and permeability. These are spatially variable, and the last two most probably also vary with time. Lower and upper limits are known for these parameters. For example, the initial formation pressure is bound by the range from hydrostatic to lithostatic (6.0 and 14.8 MPa, respectively), except perhaps within a distance of 3 m of the repository walls. Permeability values are expected to range from 10^{-22} to 10^{-21} m^2 for halite and 10^{-21} to 10^{-20} m^2 for argillaceous halite. The ranges of values of parameters used in the RIVM simulations are given in Table 4-1.

Another parameter to be selected is the length of the domain being modeled. For the purpose of numerical simulations, a finite domain must be defined. This was formalized by assuming the existence of a radius of influence, r_i, beyond which (for $r \geq r_i$) the pressure distribution in the salt formation remains practically undisturbed by experiments carried out at the borehole. The procedure for choosing the radius of influence is described in section 4.1.3.

Table 4-1. Parameters Used for RIVM Simulations

Parameters	Values	References
temperature	300K	
boundary and initial pressure (p_∞)	$(6.0 \text{ to } 14.8) \times 10^6$ Pa	Beauheim et al., 1991
brine density (ρ)	1220 kg/m^3	Beauheim et al., 1991
brine compressibility (c_f)	3.1×10^{-10} Pa^{-1}	Beauheim et al., 1991
brine viscosity (μ)	1.6×10^{-3} Pa·s	Kaufmann, 1960
permeability (k)		
(poly)halite	$(1 \text{ to } 10) \times 10^{-22}$ m^2	Beauheim et al., 1991
argillaceous halite	$(1 \text{ to } 10) \times 10^{-21}$ m^2	Beauheim et al., 1991
porosity (ϕ)	0.001 to 0.03	Beauheim et al., 1991
bulk modulus (K_m)		
halite/arg. halite.	20.7×10^9 Pa	Beauheim et al., 1991
undrained bulk mod. (K_s)		
halite/arg. halite	23.4×10^9 Pa	Beauheim et al., 1991
shear modulus (G)		
halite/arg. halite	12.4×10^9 Pa	Beauheim et al., 1991
rock compressibility (c_m)	2.69×10^{-11} Pa^{-1}	Calculated from parameters
specific capacitance (C_s)	3.0×10^{-11} Pa^{-1}	From Eq. 4-5

4.1.2 Codes Used

Simulation of the brine-inflow experiments was carried out using the computer package METROPOL developed at RIVM. The METROPOL family of computer codes is based on a Galerkin finite-element formulation of the governing partial differential equations describing the flow of water or transport of dissolved substances in a porous medium. For constant-density (flow) calculations (METROPOL-1 and METROPOL-2), the Galerkin finite-element formulation results in a system of linear equations with a symmetrical matrix. This system of equations is solved by one of the available iterative solution methods: Jacobi, Gauss-Seidel, successive over-relaxation (SOR), or conjugate gradient method (with or without preconditioning). Generally, the conjugate gradient method is the most efficient. For the transient simulations, the employed time-integration scheme is a Euler implicit method. Time steps are selected automatically on the basis of maximum allowable changes in salt mass fraction and/or pressure.

The METROPOL family of packages consists of the following programs:

- METROMESH: generates a three-dimensional mesh.
- METROREF: automatically refines the mesh.
- METROPOL-1: models steady-state groundwater flow with constant fluid density.
- METROPOL-2: models transient groundwater flow with constant fluid density.
- METROPOL-3: models transient groundwater flow and coupled salt transport with strongly varying density.
- METROPOL-4: models transient transport of tracers, including absorption/desorption and decay.
- METROPART: postprocessor for computing particle trajectories in a steady-state velocity field.
- METROPLOT: postprocessor for plotting results of simulations with the METROPOL family.

Basic characteristics of the METROPOL family are:

(i) the porous medium is considered to be fully saturated;
(ii) groundwater flow is described by Darcy's law and the conservation law for fluid mass;
(iii) permeability may be anisotropic, although the main axes of the permeability tensor must coincide with the coordinate system;
(iv) permeability and porosity may vary in space;
(v) porosity and fluid density are dependent on pressure; and
(vi) boundary conditions and sources/sinks are allowed to change with time.

Additional information on METROMESH, METROPOL-2, and METROPLOT is provided below because these programs were used in the RIVM study. A more detailed description of all the programs can be found in the user manuals (Sauter et al., 1993).

METROMESH

A three-dimensional finite element mesh is generated with the computer code METROMESH. The coordinates of nodal points are either read or generated according to the input data. One of the restrictions in generating the mesh is that the number of nodes in the x-direction must be the same on all yz-planes. This also holds for the number of nodes in y- and z- directions. All relevant output is written to an unformatted output file.

METROPOL-2

METROPOL-2 is a computer package that simulates three-dimensional transient groundwater flow. Features (i) through (vi) listed above are relevant to METROPOL-2. The primary output variable is pressure, but the hydraulic head can be calculated, as well as velocities.

The equations solved by METROPOL-2 are mass balance,

$$(\phi\, c_f + c_m)\frac{\partial p}{\partial t} = -\nabla \cdot \mathbf{q} \qquad (4\text{-}1)$$

Darcy's law,

$$\mathbf{q} = -\frac{\mathbf{k}}{\mu}(\nabla p - \rho\, \mathbf{g}) \qquad (4\text{-}2)$$

and state equation,

$$\rho = \rho_r e^{c_f(p-p_\infty)} \tag{4-3}$$

Therefore, there are five equations and five unknowns, i.e., ρ, p, q_x, q_y, q_z.

To solve the differential equations, initial and boundary conditions are needed. METROPOL-2 provides a choice from among the following boundary conditions (Sauter, 1987):

(i) no flux $(\mathbf{q}\cdot\mathbf{n}=0)$.

(ii) prescribed flux $(\mathbf{q}\cdot\mathbf{n}=\mathbf{q}_0)$, where $\mathbf{q}_0$ is a specified amount of fluid crossing the boundary.

(iii) prescribed pressure $(p=p_\infty)$ or head $(h=h_0)$.

(iv) Robin-type boundary condition $(\mathbf{q}\cdot\mathbf{n}+a(p-p_\infty)=\mathbf{q}_1)$ where a is a constant. The flux is related to a pressure difference across the boundary. The parameters $\mathbf{q}_0$, p_∞, $\mathbf{q}_1$, and p_1 may be space- and time-dependent.

METROPLOT

METROPLOT is available for postprocessing results obtained with either one of the programs in the package. With the postprocessing program, the following graphics can be generated:

(i) a cross section of the finite-element mesh in two dimensions.

(ii) colored areas which represent a certain parameter distribution, for validating input.

(iii) pressure contours or salt mass fraction contours in two dimensions, either at regular intervals or at discrete values or both.

(iv) horizontal projection or vertical projection of particle trajectories.

(v) velocity vectors in two dimensions.

4.1.3 Modeling Approach

To model the brine-inflow experiment, a simplified approach was employed. In particular, deformation processes and porosity changes were not taken into account. Major assumptions underlying the model are:

1. Darcy's law describes movement of brine through inter-crystalline spaces of the rock salt under the influence of a pressure gradient.
2. Major salt layers are included in the model, but each layer is assumed to be homogeneous and isotropic.
3. All mechanical effects such as deformation of salt crystals and salt creep are neglected.
4. The phenomenon of microcracking in salt, caused by the release of pressure in the formation as a result of nearby excavations, is neglected. This is an important effect because microcracks in the early stages cause an increase in porosity and a significant rise in permeability, which in later stages decrease because of crack healing.
5. The presence of brine inclusions (intragranular brine) is neglected.
6. All temperature effects are neglected.
7. Dissolution and precipitation of salt crystals are neglected.
8. Presence of gas in the formation and its effect on brine movement are neglected.
9. Brine density and viscosity are assumed to be constant in time and space.
10. The initial pressure distribution in the formation is assumed to be uniform and equal to the formation pressure.
11. The storage of the system is assumed to be due entirely to elastic compressibility of brine and rock salt.
12. For boreholes drilled vertical to the layering, flow is assumed to be radially symmetric.
13. The possibility of fluid release from mineral dehydration or clay compaction is neglected.

Because of these assumptions, brine movement may be simply modeled by the groundwater flow equations given below:

$$C_s \frac{\partial p}{\partial t} + \nabla \cdot \mathbf{q} = 0 \tag{4-4}$$

where the specific capacitance of the medium (C_s) is defined as:

$$C_s = \left(\phi c_f + c_m\right). \tag{4-5}$$

The basic equations describing movement of brine from the formation to the boreholes during the brine-inflow experiments are Eq. 4-1 through 4-3. The initial condition is:

$$p = p_\infty \text{ for all points at } t = 0$$

The boundary conditions are:

$$p = 0 \quad \text{at} \quad r = r_w$$

$$p = p_\infty \quad \text{at} \quad r = r_i$$

where r_w is the borehole radius and r_i is the radius of influence beyond which no appreciable pressure change will occur.

To examine the effect of some of the parameters on simulation results, a number of calculations were performed using data from borehole DBT11.

In the case of a one-layer homogeneous system, the brine inflow at steady state is proportional to the initial pore pressure and permeability (Nowak et al., 1988) if $r_w \ll r_i$:

$$\left|\mathbf{q}_{borehole}\right| = \frac{k p_\infty}{\mu r_w} \frac{1}{\ln\left(r_i / r_w\right)} \tag{4-6}$$

Calculations by METROPOL for the layered cases agree fairly well with this relation. Some of the results are described here briefly.

SENSITIVITY STUDIES

Sensitivity studies were performed to determine the effects that changes in the mesh length, assumed initial pressure, permeability, and storage coefficient might have on the modeled results.

Mesh Length (Location of Boundary)

Theoretically, according to the analytical solution for steady radial flow to a well, the rate of flow is inversely proportional to the logarithm of the mesh length (distance to a constant-pressure boundary). Comparing the flow rate for different mesh lengths after 1000 days shows that this is indeed the case (Table 4-2 and Figure 4-1).

Table 4-2. Brine-Inflow Rate after 1000 Days Calculated with Different Mesh Lengths

Mesh Length (m)	Flow Rate (g/day)
1	16.44
5	9.50
10	8.66
50	< 7.82

The 50-m-long mesh had not reached steady state after 1000 days; assuming that the pressure front migrates and reaches the constant-pressure boundary very slowly, this is to be expected. However, as is apparent in Figure 4-1, the effect of distance to a constant-pressure boundary is negligible beyond 10 m for a 1000-day simulation. Therefore, a mesh length of 10 m to a constant-pressure boundary was used for all subsequent calculations.

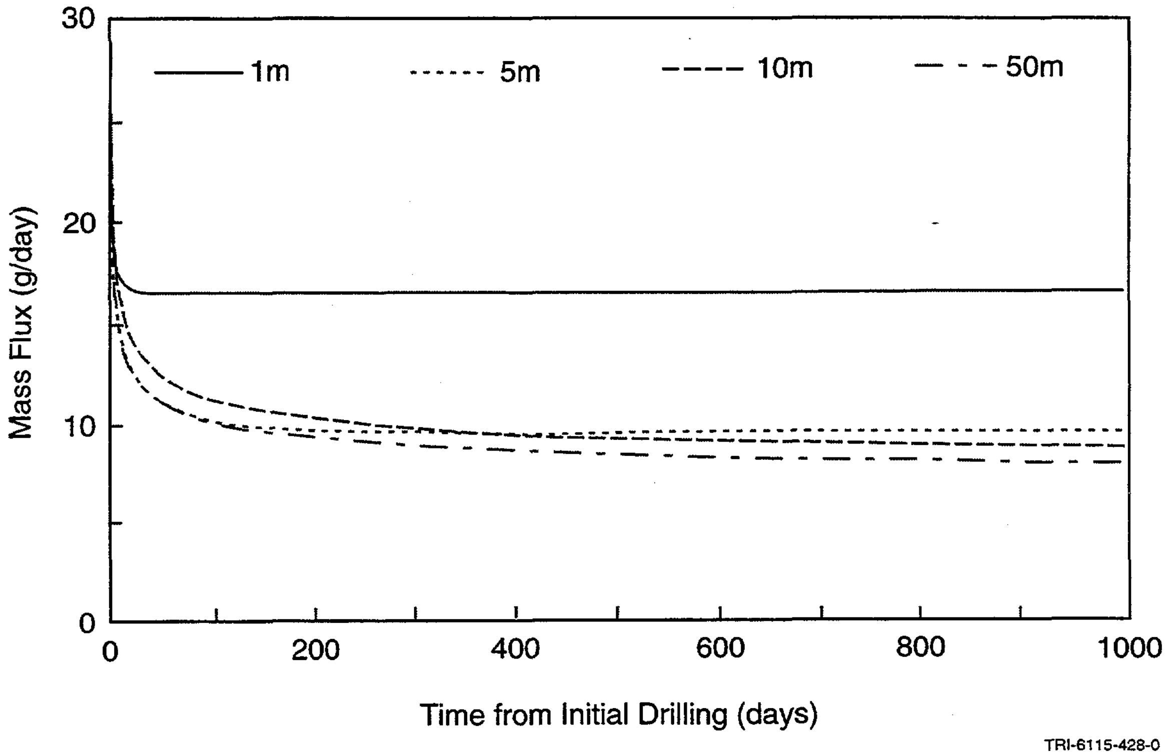

Figure 4-1. Sensitivity of brine inflow to the distance to a constant-pressure boundary.

Initial Pressure

The inflow rate is calculated for initial pressure values of p_∞ = 6.0, 10.0, and 14.8 MPa. After 1000 days, the values 5.20, 8.66, and 12.80 g/day, respectively, are obtained. Results are shown in Figure 4-2.

Permeability

To investigate the sensitivity of brine inflow to permeability, the average permeability values of 5.0 x 10^{-22} m^2 and 5.0 x 10^{-21} m^2 for pure and argillaceous halite were lowered by a factor of five (low *k*) and increased by a factor of two (high *k*). The

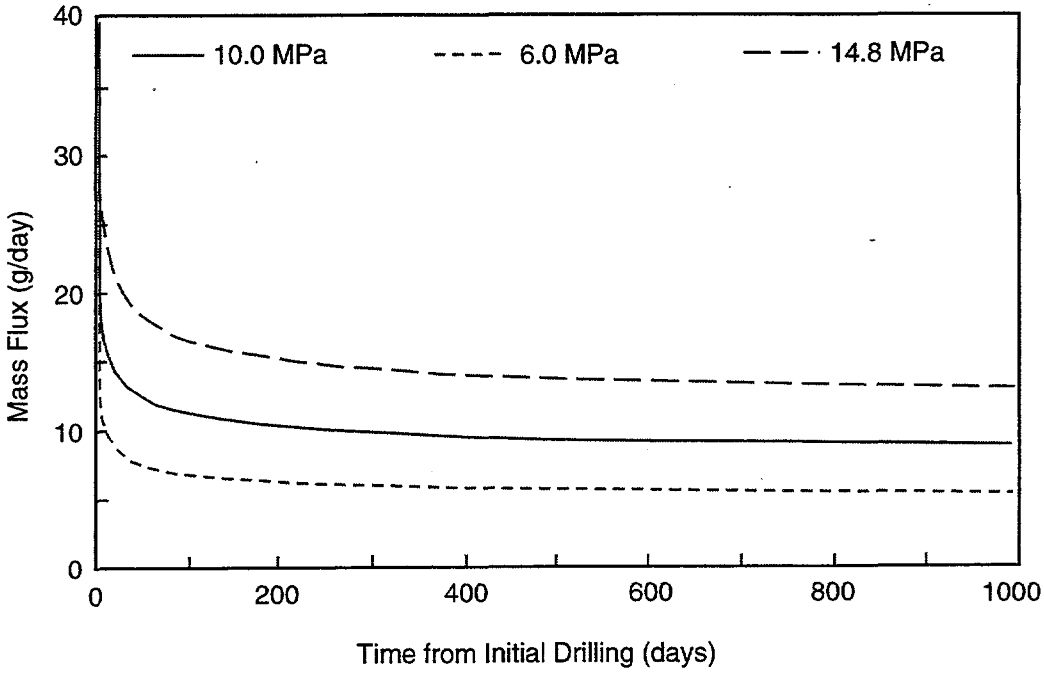

Figure 4-2. Sensitivity of brine inflow to the initial pore pressure.

steady-state values of brine flux for low k, average k, and high k are 2.05, 8.66, and 16.74 g/day, respectively. Figure 4-3 shows the sensitivity to permeability, given an initial pressure of 10.0 MPa. As suggested by Eq. 4-6, there is almost a linear relation between $q_{borehole}$ and k. The discrepancy is due to the fact that there are two layers with different permeability values present so that Eq. 4-4 is only approximately valid.

Specific Capacitance

The specific capacitance, C_s, comprises three parameters: porosity (ϕ), fluid compressibility (c_f), and rock compressibility (c_m) (see Eq. 4-5). In Figure 4-4, the brine mass flux calculated for two extreme values of specific capacitance are shown. As expected, the rate of brine inflow is smaller for a lower value of specific capacitance. From Figure 4-4 it is obvious that steady state is not reached even after 1000 days because the steady-state value of the brine-inflow rate should be equal for both values of specific capacitance.

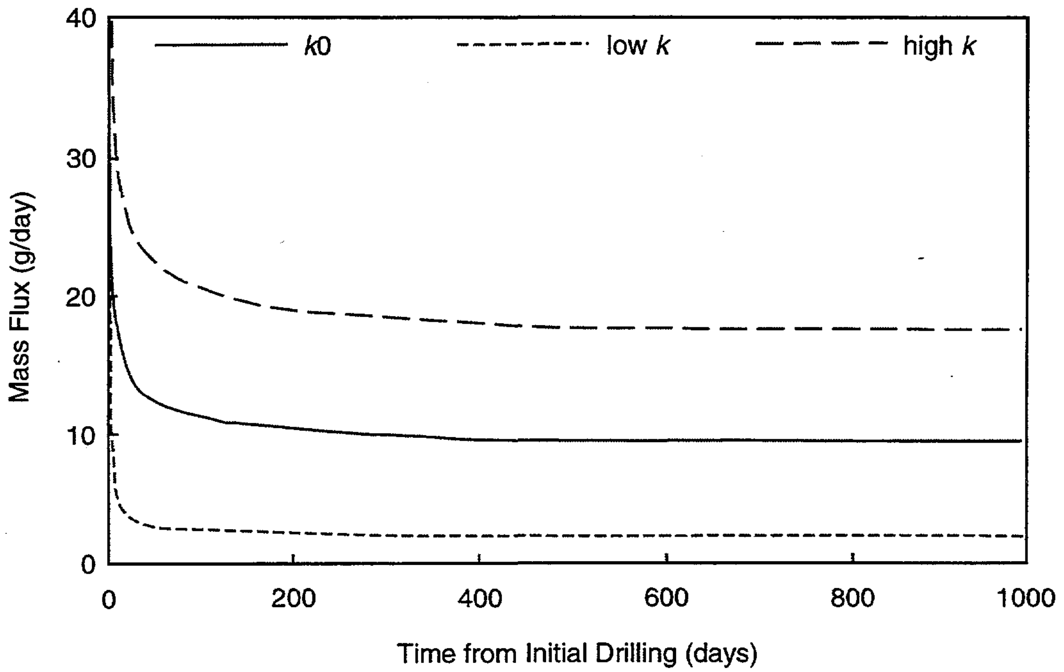

Figure 4-3. Sensitivity of brine inflow to permeability.

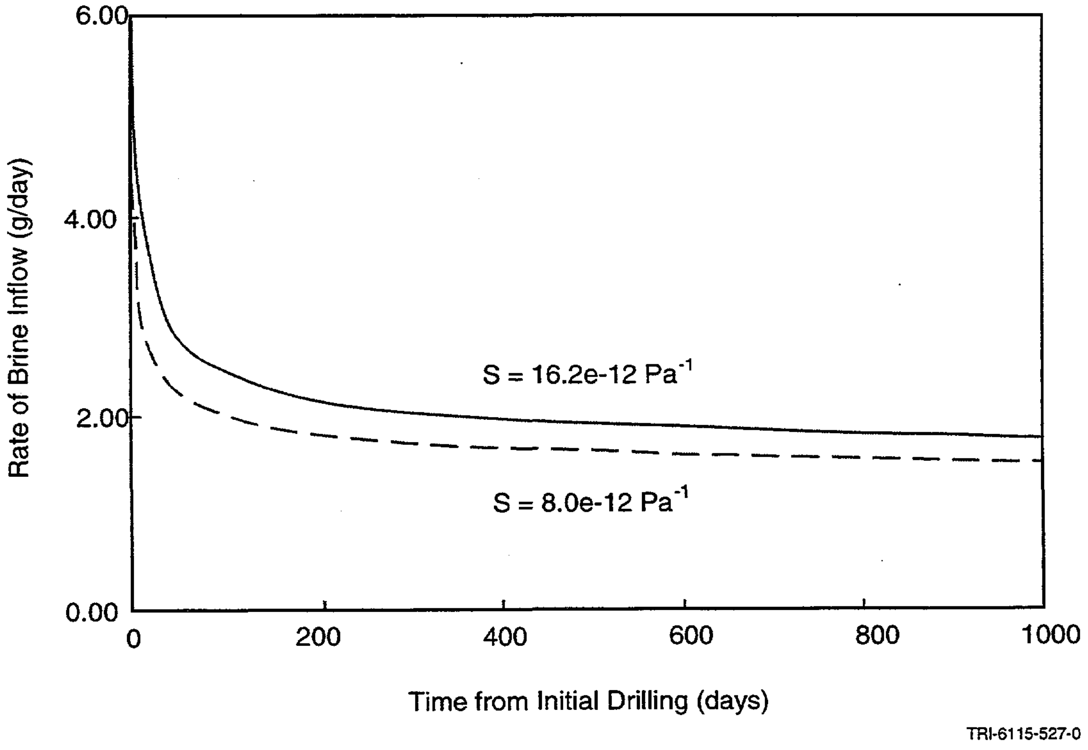

Figure 4-4. Sensitivity of brine inflow to specific capacitance.

4.1.4 Results

Based on results of the sensitivity analyses, a large number of simulations were carried out for borehole DBT11 to obtain an optimum set of values for formation pressure, porosity (or rock compressibility), and permeability such that an acceptable fit was obtained for mass flux and the accumulated mass of brine seeping into the borehole. The selected set of parameter values is:

Formation pressure p_∞ = 10 MPa
Porosity ϕ = 0.01
Rock compressibility c_m = 2.69×10^{-11} Pa^{-1}
Halite permeability k = 4.0×10^{-22} m^2
Argillaceous halite permeability k = 4.0×10^{-21} m^2

These values were then used as input to simulate the brine inflows observed in boreholes DBT10, DBT12, and DBT13. The sequences of thicknesses of pure and argillaceous halite layers used to simulate the stratigraphy around those three holes are given above in Tables 3-2, 3-4, and 3-5. In simulating the brine inflows to boreholes DBT10, DBT12, and DBT13, the parameter values obtained from the DBT11 simulations were modified slightly to provide the best aggregate fit to the data from the four boreholes.

Results of the calculations for brine-inflow experiments in boreholes DBT10, DBT11, DBT12, and DBT13, together with experimental data, are plotted in Figures 4-5 to 4-8. The brine inflow rates appear to approach steady-state values after about 300 days. However, further measurements have shown an increase in the amount of brine inflow, indicating that steady state has been disturbed by some change in conditions. The measured rates of brine inflow at the "interim" steady state are given in Table 4-3, along with the total amount of brine collected after about 1000 days is reported. Calculated values are also given in this table.

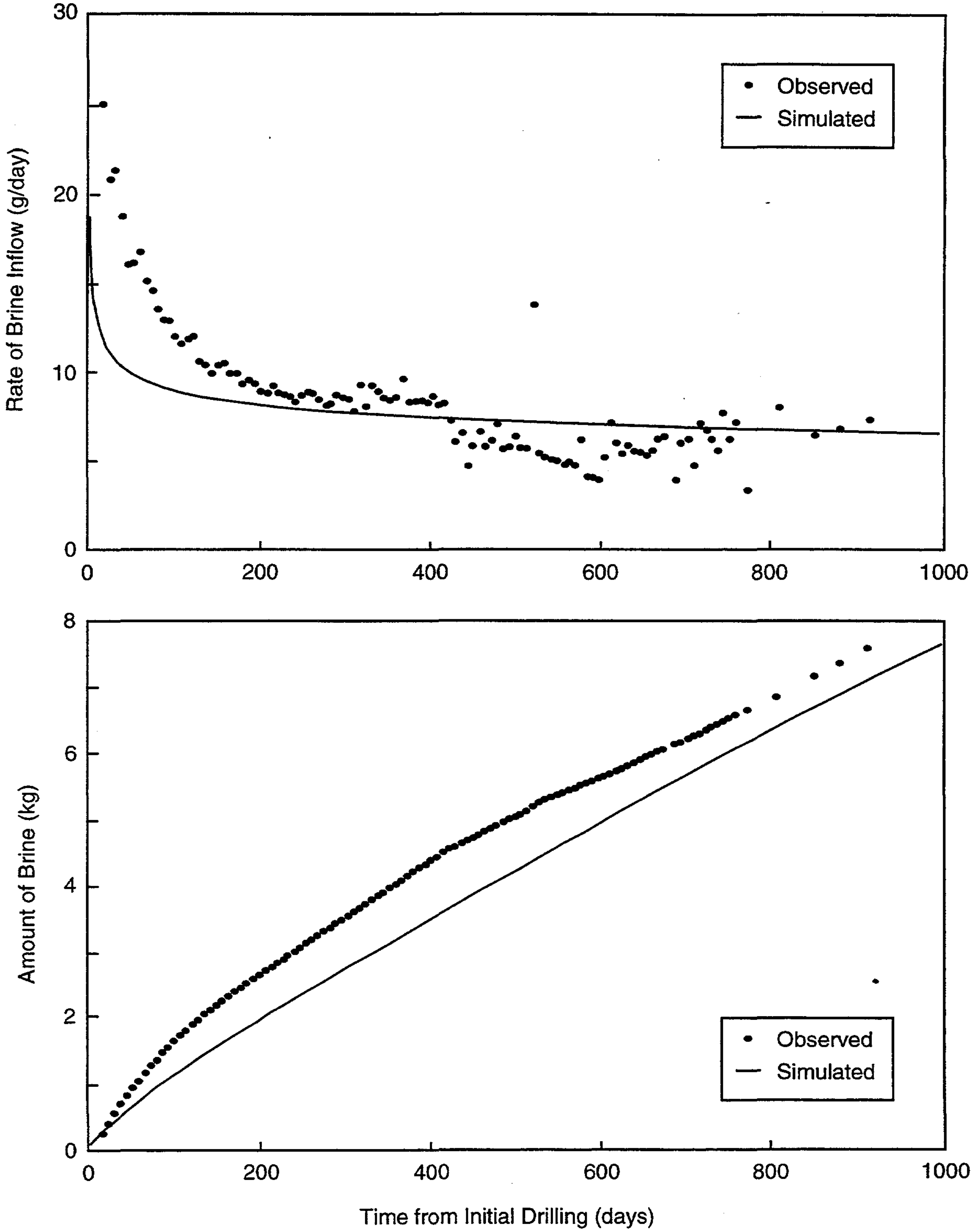

TRI-6119-394-0

Figure 4-5. Comparison of observed and RIVM-calculated flow rates and volumes of borehole DBT10 for a period of 1000 days.

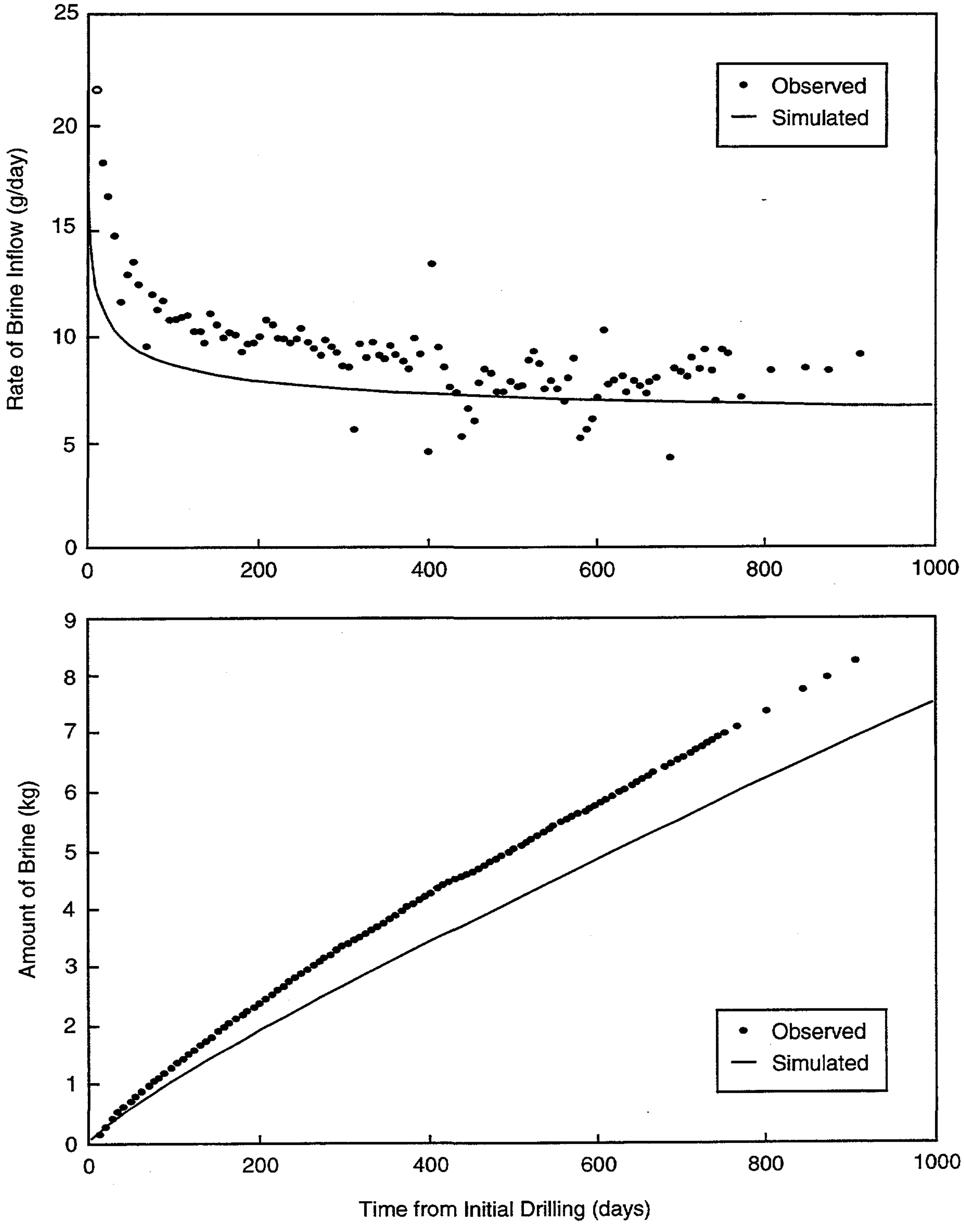

TRI-6119-395-0

Figure 4-6. Comparison of observed and RIVM-calculated flow rates and volumes of borehole DBT11 for a period of 1000 days.

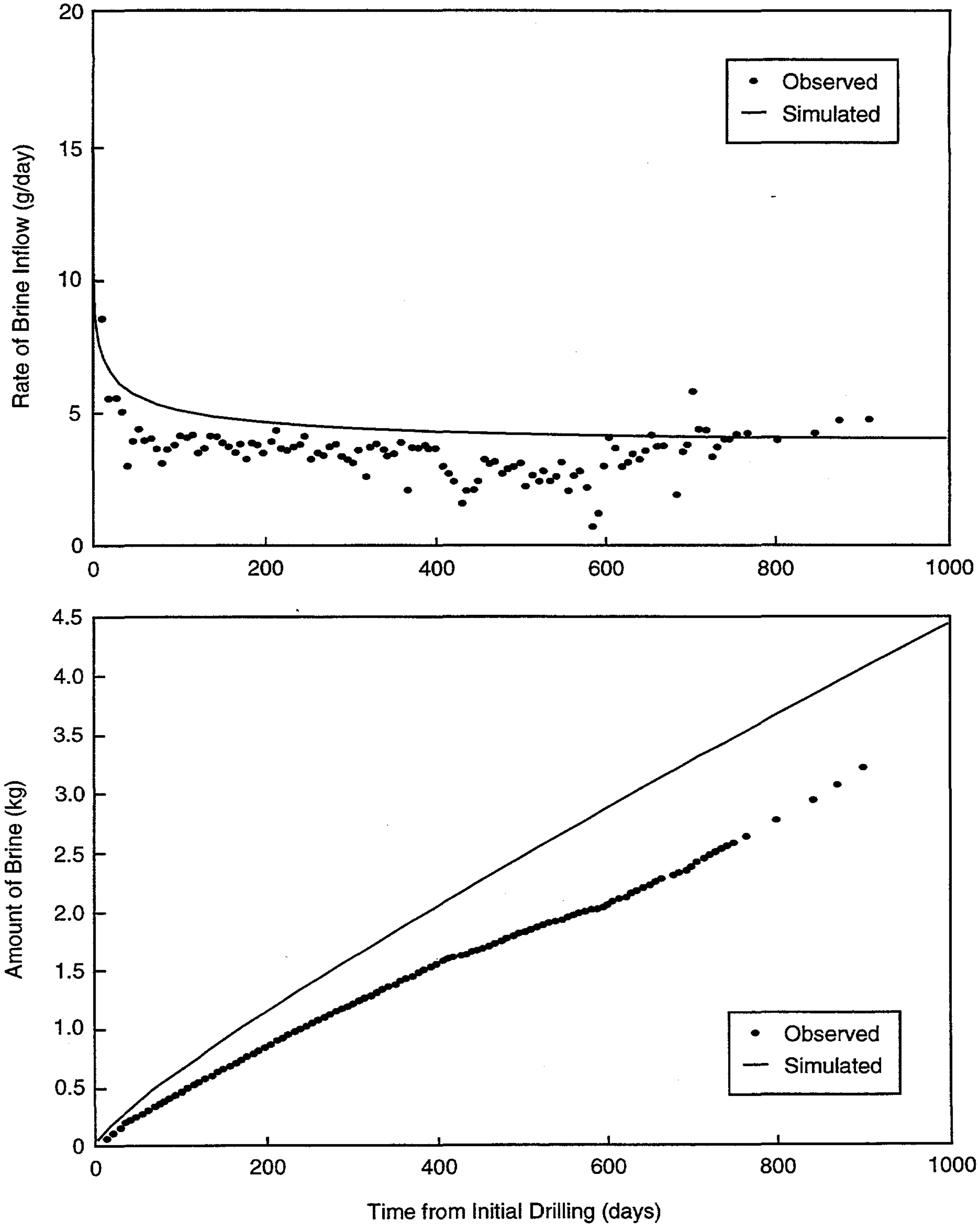

TRI-6119-396-0

Figure 4-7. Comparison of observed and RIVM-calculated flow rates and volumes of borehole DBT12 for a period of 1000 days.

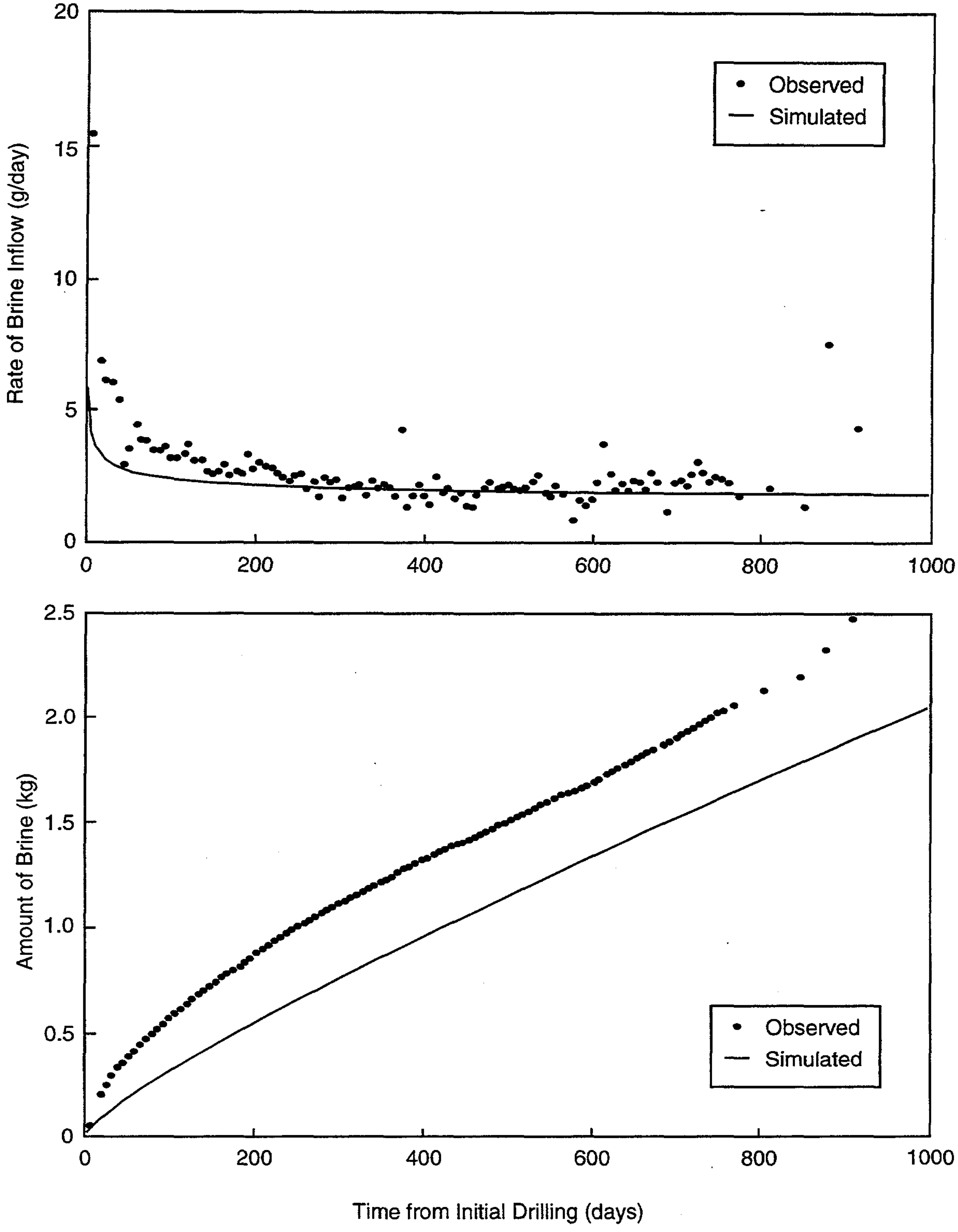

TRI-6119-397-0

Figure 4-8. Comparison of observed and RIVM-calculated flow rates and volumes of borehole DBT13 for a period of 1000 days.

Table 4-3. Measured and Calculated Amounts of Brine Inflow

	Measured Amounts of Brine Inflow		Calculated Amounts of Brine Inflow	
Borehole	Interim Steady-State Value (g/day)	Total Amount of Brine (kg)	Interim Steady-State Value (g/day)	Total Amount of Brine (kg)
DBT10	5.8	8.0	6.8	7.7
DBT11	6.8	8.8	6.6	7.4
DBT12	3.0	3.2	3.8	4.3
DBT13	2.1	2.5	1.8	2.1

MAGNITUDE OF BRINE-MIGRATION VELOCITY

The velocity with which brine moves within the rock salt is important in the study of transport of radionuclides. Because of the very low permeability of rock salt, the brine velocity is expected to be very small. In the case of the brine-inflow experiments, the maximum velocities occur near the boreholes during the early stages of the experiments. Calculations show that, taking into account the porosity, the maximum real velocity is of the order of 10^{-9} m/s. This value decreases rapidly with time or distance from the borehole. Even at this maximum rate, however, brine would move only about 300 m in 10,000 years. Therefore, transport of radionuclides by brine in halite should not be of regulatory concern.

4.1.5 Problem Areas

It is known that the excavation of the repository causes pressure reduction and stress relief around the excavated rooms. These effects will in turn result in structural changes leading to increases in porosity and permeability. In the simulations carried out to model the inflow and permeability experiments, these effects have been neglected; both porosity and permeability are assumed to be constant in time and space. In addition, the initial pressure around the boreholes is assumed to be equal to the far-field pore pressure.

In order to investigate the effects of this assumption on the calculated flows, a simulation of the pore-pressure distribution created by excavation in a horizontal domain around the repository was carried out. This simulation considered only pressure changes resulting from flow towards the repository and did not include the effects of stress relief.

Only the main north-south drifts were considered. These drifts were lumped together and modeled as a single room with dimensions of 1500 m by 20 m (based on dimensions given in Figure 3-1). The model dimensions were chosen to be 15,000 m by 400 m, that is, ten times the dimensions of the room in each direction. Because of symmetry, calculations were carried out for one fourth of the model domain. The generated mesh is given in Figure 4-9. The initial condition was chosen to be a uniform pressure of 10 MPa (equal to the average formation pressure). Because of symmetry, the boundary conditions at the left and lower boundaries were specified to be no-flow, and at the upper and right boundaries, the pressure was set equal to 10 MPa. The pressure at all points inside the excavated room, the rectangle ABCD in Figure 4-9, was fixed to be 10^5 Pa. For permeability and specific capacitance, the values corresponding to argillaceous halite were chosen. The pressure profile along a line perpendicular to the excavated room (a continuation of the line AD in Figure 4-9) after 10 years is given in Figure 4-10. The changes of pressure with time at various distances from the room wall are given in Figure 4-11. A substantial pressure drop is predicted in the vicinity of the excavation. However, this effect is limited to a distance of about five meters from the room wall, and the pressure rapidly increases to the formation pressure beyond that distance. At longer times, however, the pressure drop penetrates deeper.

Even though the simulation modeled only pressure changes in a horizontal plane around the room, it is clear that pressures must have changed vertically around the room as well. Considering that Room D, from which the DBT10 to DBT13 boreholes were drilled, was excavated three and a half years before the brine-inflow experiments began, a non-uniform pressure must have existed along the 5-m (or less) length of the DBT10 to DBT13 boreholes at the time they were drilled. To whatever extent the pore pressure driving flow towards the brine-inflow boreholes was less than the 10 MPa assumed in the calculations, the permeability must be proportionally larger than the calculated value.

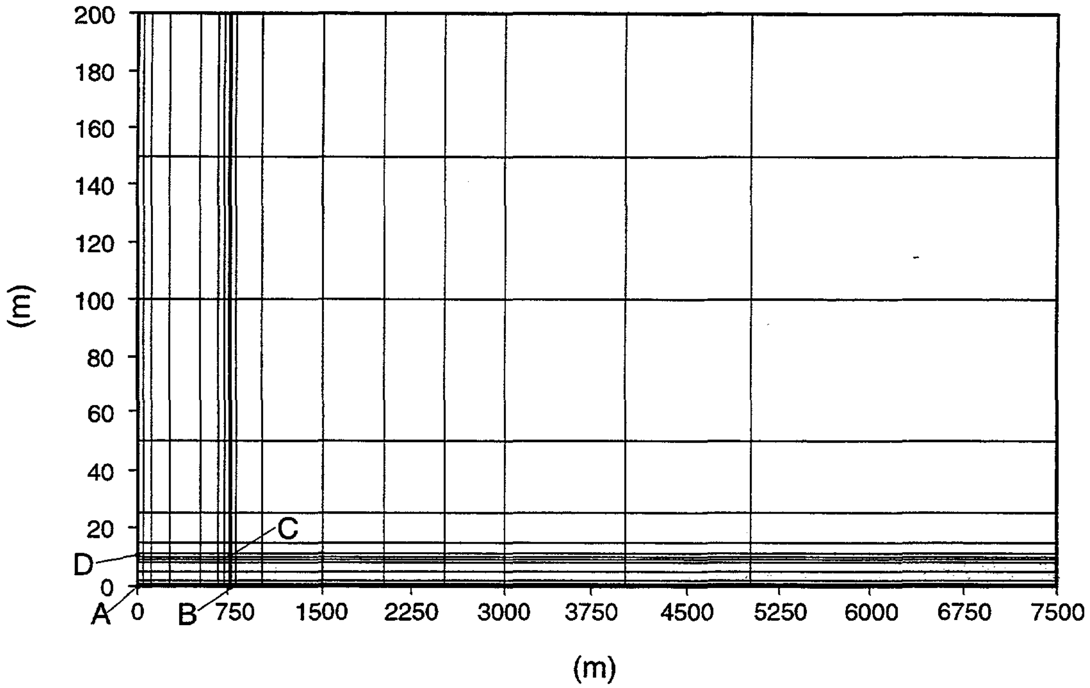

Figure 4-9. Mesh used for RIVM calculation of pressure distribution around the room.

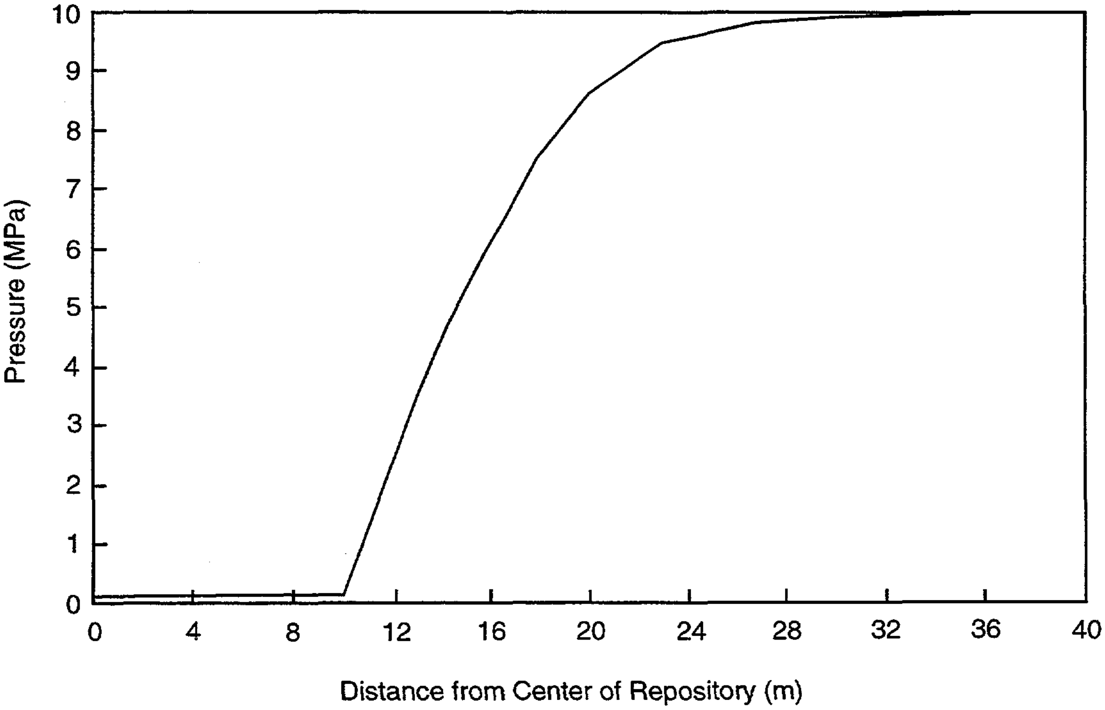

TRI-6115-526-0

Figure 4-10. Distribution of pressure along a line perpendicular to the room wall after 10 years.

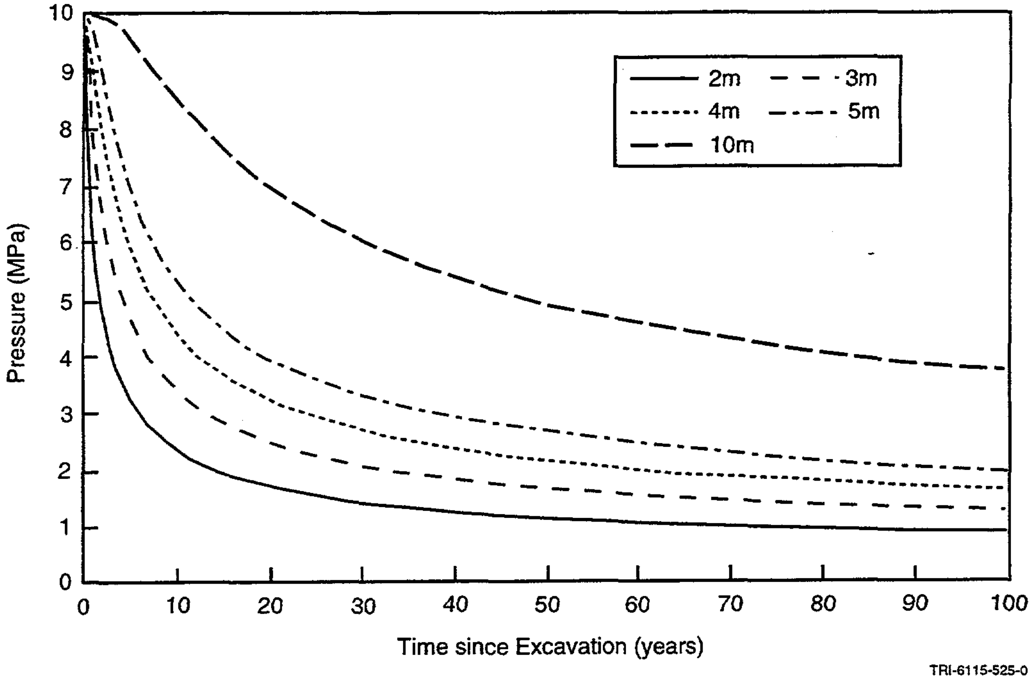

Figure 4-11. Change of pressure with time at various distances from the room wall.

Ultimately, the far-field pressures are uncertain. Vertical flow toward excavations must be affecting simultaneous horizontal radial flow toward boreholes. Realistic modeling cannot be performed without information on vertical permeability and vertical heterogeneity of horizontal permeability layering. A partially unsaturated or two-phase zone around boreholes may also be affecting results. The specifics of deformation and accompanying changes in hydraulic properties around excavations are also poorly known.

A very important issue in brine-inflow experiments is the trend change, which is evident in Figure 3-2. In all boreholes, the inflow rate is high at the start of the experiments and decreases exponentially, approaching an apparent steady-state value; this corresponds to common expectations of flow to a borehole. However, after about 1000 days, the inflow rates start to increase considerably and reach values even higher than those at the start of the experiments. The simulations of the experiments were carried out up to a time of 1000 days, and no attempt was made to simulate the rise of inflow rate. Apparently, the steady state has been disturbed by some undefined changes in conditions. Perhaps geomechanical effects have altered the structural integrity of the strata around Room D so that additional brine has become available to the boreholes. Such effects will not be important for large-scale, long-term brine inflow to the repository because long-term flow will ultimately be limited by the undisturbed, far-field properties of the formation.

4.2 EdM Project Team

The EdM study of the WIPP 1 test case was originally reported by Aït-Chalal et al. (1993).

4.2.1 Modeling Purpose/Strategy

An important objective of the EdM study is to account for the perturbations that the excavation of Room D produced in the hydraulic-head field within the formation before the brine-inflow tests. Instead of assuming that the hydraulic head is initially uniform, as was done in the RIVM study, the EdM study assumed that the excavation of a room creates a disturbance that alters the head in the vicinity of the room. Thus, to interpret the collected flow data correctly, it is necessary to consider complex initial conditions rather than a uniform distribution.

The EdM modeling comprised two calculations. In the first, hydraulic-head changes during the period from the excavation of Room D through the drilling of a borehole were simulated. The distribution of the hydraulic head around the room at the end of the first calculation then served as the initial condition for the second calculation, which simulated the *in situ* test and modeled brine inflow to a borehole for a period of 1000 days.

The first calculation was performed in a vertical plane around Room D. The second calculation was executed in axial symmetry around a borehole. This axis of symmetry coincides with the axis of the borehole. This approach implicitly assumed that the zone disturbed by the excavation was not greater in any direction than the width of the drift. Using the results from the first calculation to define the initial conditions of the second calculation necessitated a specific process to account for the transition from a planar calculation to the calculation in axial symmetry. At the end of the first calculation, the equipotential distribution within the formation is approximately in the form of nested cylinders. To perform the second calculation in axial symmetry, horizontal approximations of the bases of these cylindrical surfaces near the borehole were introduced (see Figure 4-12).

The objective of the second calculation was to determine variations in the hydraulic head that are caused solely by the presence of the borehole. Initially, the calculation led to a rapid modification of the equipotential network independent of the presence of the borehole. Specifically, the transition from planar to axial symmetry resulted in, at infinite time, an equipotential surface that reflected a linear variation of the head as a function of the distance between the upper and lower boundaries of the mesh. To correct this result, a source term was introduced, simulating artificial fluid emissions within the model domain. The source term was calibrated such that the steady-state equipotential distribution in the absence of a borehole coincided with the new initial distribution of equipotentials.

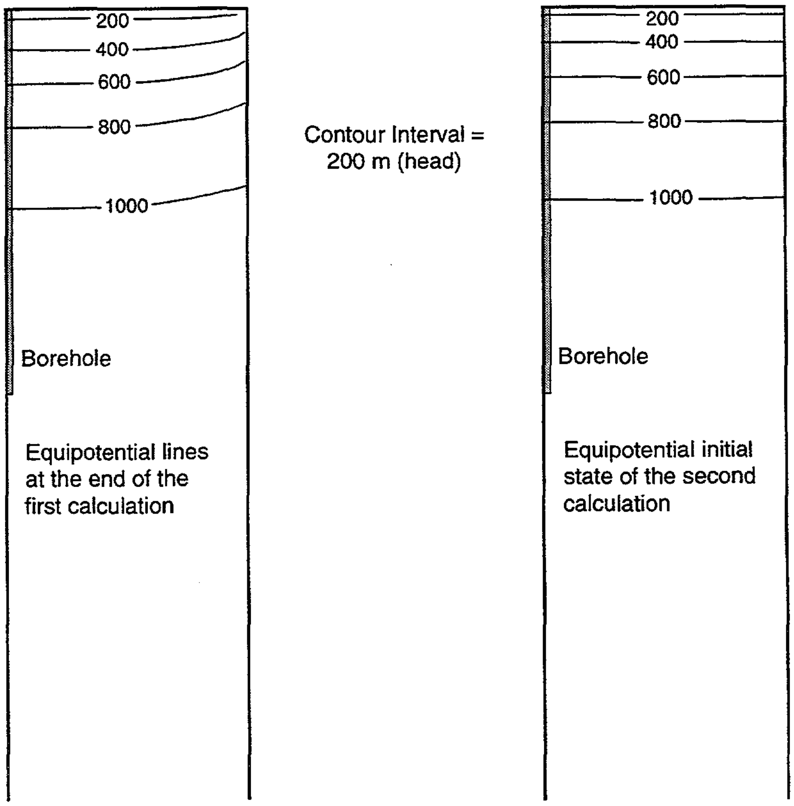

TRI-6115-524-0

Figure 4-12. Approximation of equipotential lines beneath Room D.

4.2.2 Modeling Approach

BOUNDARY CONDITIONS

As previously discussed, the small-scale brine-inflow test simulation comprised two calculations. The first calculation determined the distribution of the hydraulic head around Room D, as well as the dimensions of the second model. The simulation was made for the time between the excavation of the room and the drilling of the borehole, about 1270 days. In the first calculation, the source term (Q) was set to zero.

At the start of the first calculation, the distribution of the hydraulic head is uniform. Because of the lack of measured pore pressures within the formation, the value of hydraulic head was set equal to 1075 m of brine, a value between the hydrostatic and lithostatic pressures at a depth corresponding to the center of the room. The boundary conditions are given in Figure 4-13. For the second calculation, the hydraulic head distribution corresponded to the values obtained at the end of the first calculation. The second-calculation boundary conditions are given in Figure 4-14.

MODELING ASSUMPTIONS

Simulations of brine flow through salt were conducted using the following assumptions:

1. the salt is treated as a saturated medium in which brine flow follows Darcy's law;
2. the hydraulic gradient is the only flow force;
3. the salt is assumed to be homogenous and isotropic;
4. mechanical and thermal effects are neglected; and
5. any dissolution of salt crystals or precipitation of salt from brine is neglected.

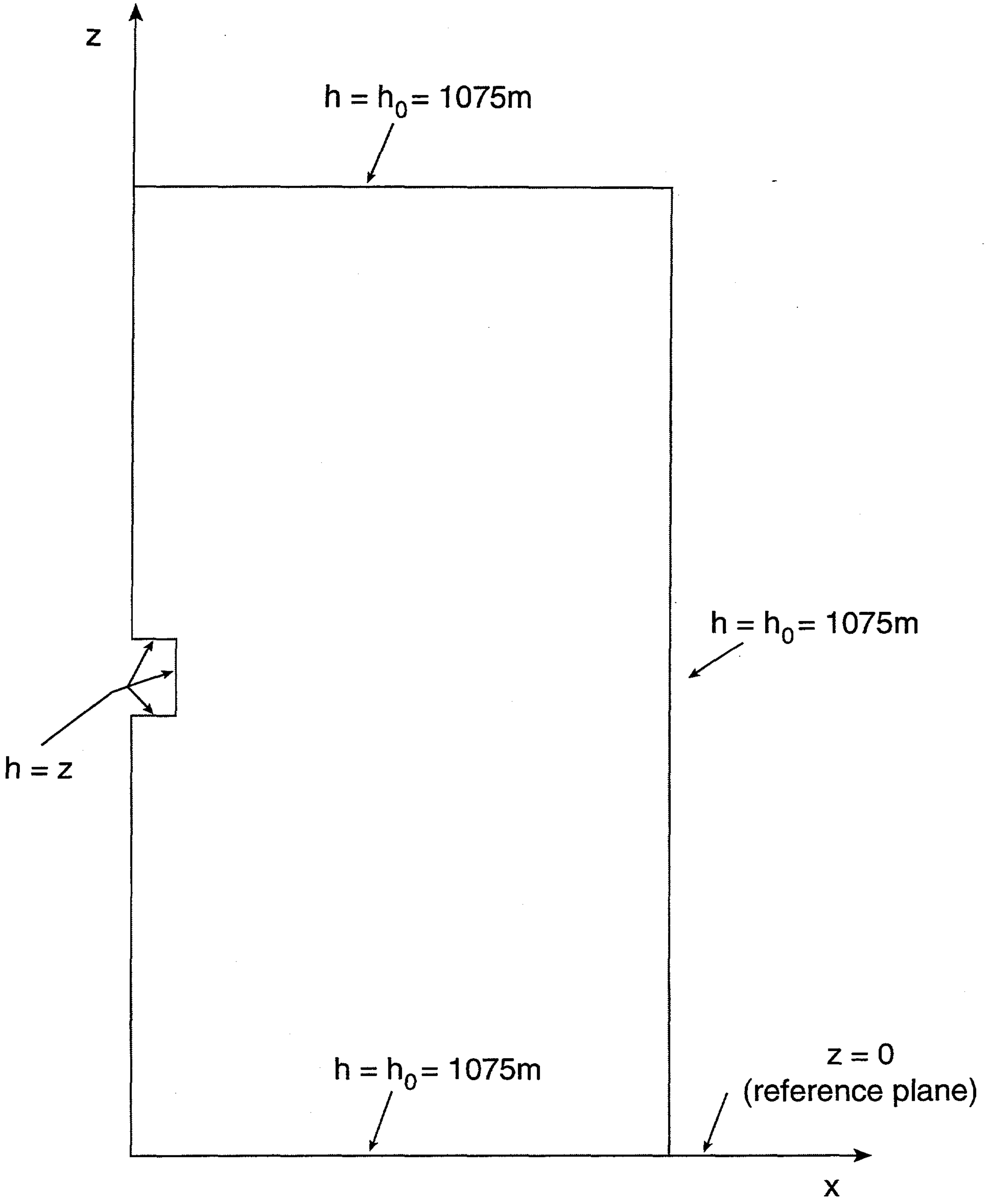

TRI-6115-522-0

Figure 4-13. Boundary conditions of the first calculation.

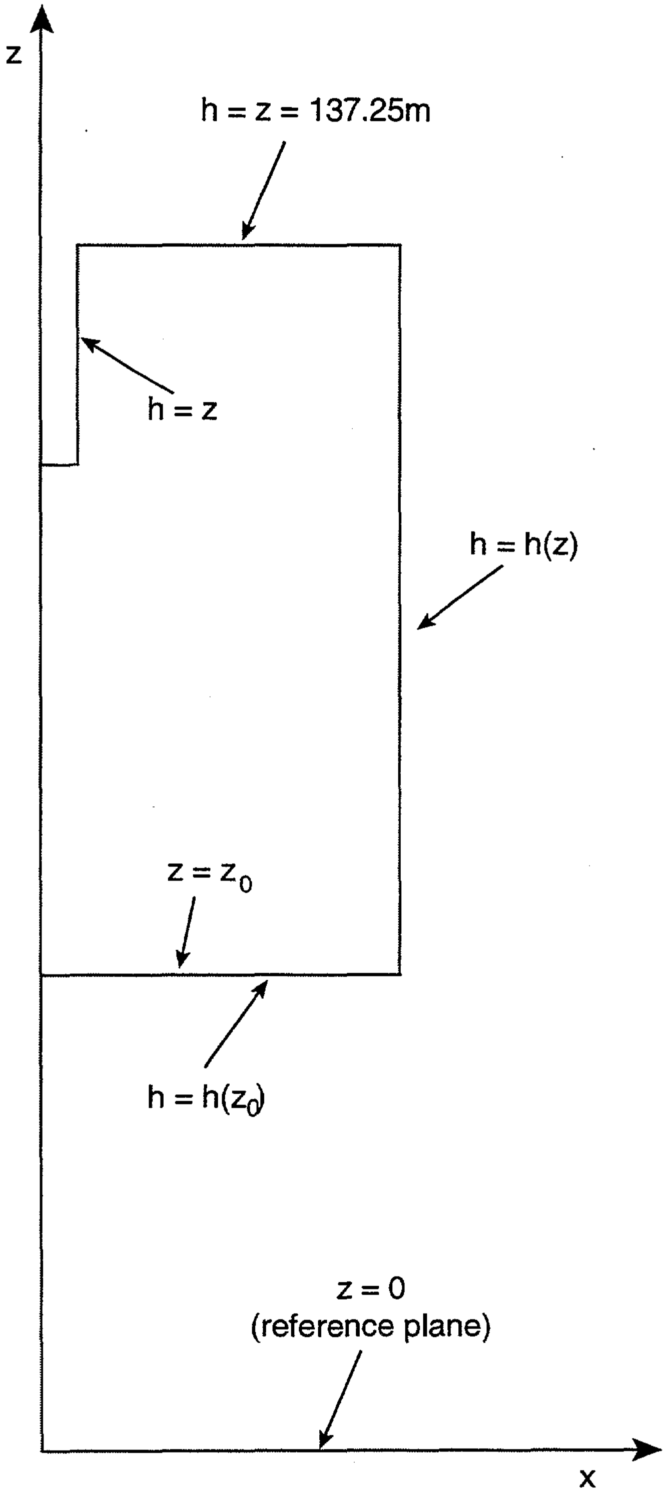

TRI-6115-523-0

Figure 4-14. Boundary conditions of the second calculation.

BASIC EQUATIONS

Flow through a porous, isotropic medium is assumed to result from the hydraulic gradient, subject to Darcy's law, which is formulated in the following equation:

$$\mathbf{q} = -K \operatorname{grad} h \tag{4-7}$$

where the hydraulic head, h, is given in the following formula:

$$h = \frac{p}{\rho \mathbf{g}} + z \tag{4-8}$$

and hydraulic conductivity (K) is related to permeability (k) by:

$$K = k \frac{\rho \mathbf{g}}{\mu} \tag{4-9}$$

The unknown parameters in Eq. 4-7 are the Darcy velocity and the hydraulic head. To solve the problem, a second equation is needed to express the mass balance:

$$\operatorname{div}(\mathbf{q}) + S_s \frac{\partial h}{\partial t} = Q \tag{4-10}$$

where S_s is the specific storage and Q is a source term.

Assuming that the fluid density is not pressure-dependent and that flow is isothermal, the problem is a system of two differential equations with two unknown functions. Combination of Eqs. 4-7 and 4-10 provides one equation in terms of head.

$$\operatorname{div}(-K \operatorname{grad} h) + S_s \frac{\partial h}{\partial t} = Q \tag{4-11}$$

To solve this problem, the boundary conditions and initial conditions for the transient system must be added.

4.2.3 Code Used

The EdM modeled brine inflow using the HYDREF code, a numeric calculation code using the finite-element method. This code was developed at the Centre de Géotechnique et d'Exploitation du Sous-sol of the École des Mines de Paris beginning in 1969. HYDREF is well adapted to modeling hydraulic flow in a porous medium in steady or transient state. HYDREF comprises a data-input program (LECHYDR), a finite-element calculation program (CALHYDR), and a postprocessing analysis program (RESHYDR).

LECHYDR is an interactive graphical program enabling the automatic construction of a two-dimensional mesh and preparation of the data required by the calculation program. Construction of the mesh requires definition of the model boundary and selection of triangular or quadrilateral elements. LECHYDR offers a graphical view of the mesh during the generation process, allowing easy modifications when required.

Using LECHYDR-generated data, CALHYDR solves the problem by the finite-element method. CALHYDR computes hydraulic head and Darcy velocity at any instant in media comprising one or more materials, taking into account variations of hydraulic characteristics. The code solves any two-dimensional problem in either planar or axially symmetric coordinates. CALHYDR has a complete isoparametric finite-element library which is split into families of first- and second-degree elements. The library contains three-node triangular elements and four-node quadrilateral elements to be used in linear interpolation. For second-degree quadratic interpolation, the library has six-node triangles and eight- or nine-node quadrilaterals.

RESHYDR is a postprocessing tool that allows the results obtained with CALHYDR, such as hydraulic head and Darcy velocity, to be viewed on a graphics screen or output to a plotter. RESHYDR can also be used to plot the mesh generated by LECHYDR.

LECHYDR and CALHYDR are written in FORTRAN IV/72 and are free-standing. RESHYDR is written in FORTRAN IV/77 and requires a graphics-device library.

The rate of fluid flow through a porous medium is determined by the general differential equation combining mass balance and Darcy's law subject to the boundary conditions of the system. The finite-element method is used to solve this type of problem. The model domain is separated into sub-domains of simple geometric forms, called finite elements. In the first model, which simulates the effects of the excavation of the room, the domain was discretized into 256 second-order quadrilateral elements totaling 1089 nodes (Figure 4-15). In the second model, representing flow to a borehole, the mesh comprises 272 second-order triangular elements totalling 680 nodes (Figure 4-16).

SOURCE-TERM CALCULATION

To assure that the steady-state solution of head within the second model domain remained consistent with the boundary conditions $[h_1(z)]$ from the first model, an artificial source term (Q) was introduced. This term is calibrated so that the solution $h_1(z)$ is reached at steady state. Then Eq. 4-11 yields:

$$Q = -K\frac{d^2h_1}{dz^2} \tag{4-12}$$

MODELING PROCEDURE

The objective of the study was to determine the hydrogeologic parameters of the formation by comparing the results of the calculations to the results of the *in situ* experiment.

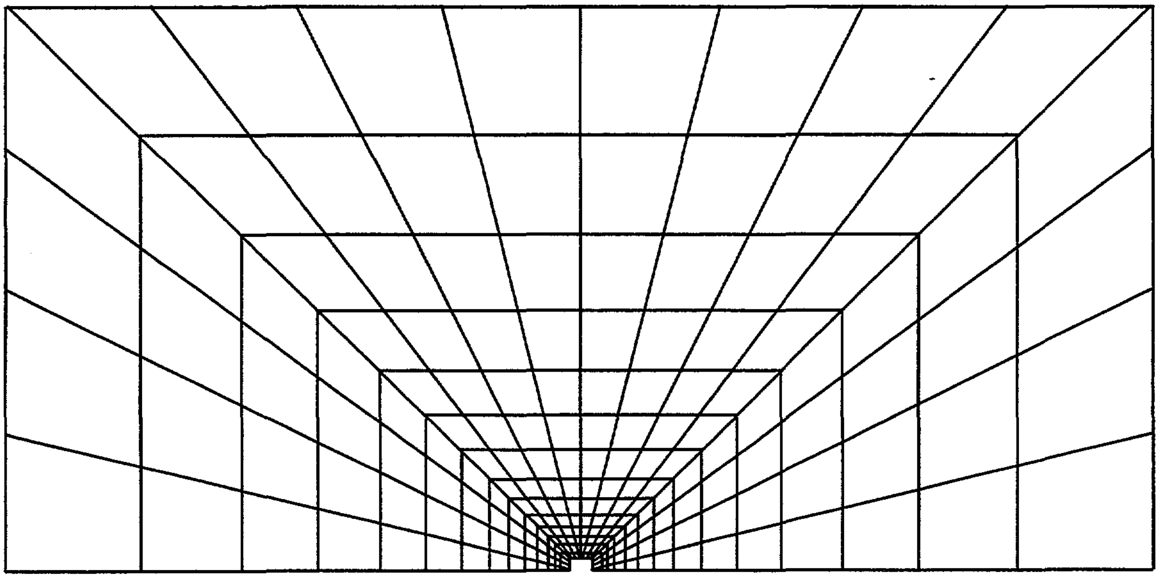

Figure 4-15. First model mesh.

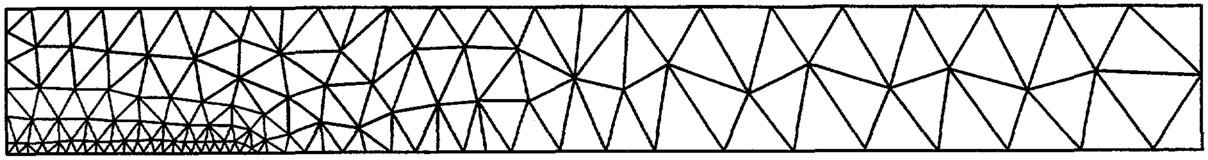

Figure 4-16. Second model mesh.

The modeling procedure consisted of the following steps:

1. Select values for hydraulic conductivity (K) and specific storage (S_s).
2. Calculate the transient hydraulic-head distribution around Room D using the first model.
3. Calculate the steady-state inflow rate to a borehole using the second model.
4. Determine λ where

$$\lambda = \frac{\text{measured steady - state flow rate}}{\text{calculated steady - state flow rate}}$$

5. Keeping the value of S_s constant, calculate a new K according to $K_{i+1} = \lambda\ K_i$.
6. Repeat steps 2 through 5 until convergence is achieved $(\lambda = 1 \text{ or } K_{i+1} = K_i)$.
7. Calculate the hydraulic-head distribution around Room D and the time-dependent inflow to a borehole in the transient system using the final value of K_{i+1} and the value of S_s.
8. Calculate the mean quadratic deviation between the whole of the measured and the calculated inflow values for the entire 1000-day period.
9. Choose a new value of S_s. Repeat steps 7 and 8 until the minimum of the mean quadratic deviation is reached.
10. Insert the final value of S_s and the value of K_{i+1} in step 1 and repeat the entire process until the values for both S_s and K have stabilized.

4.2.4 Results

Using the experimental results of the flow test conducted in hole DBT13 (Figure 4-17), the average rate of mass flow in the steady-state system was determined to be 1.97 g/day. Examination of the experimental curve led to the conclusion that steady-state equilibrium was reached 400 days after drilling the borehole. The choice of hole DBT13 is justified by the presence of a clearly marked steady-state phase and the absence of scatter in the data.

The transient-state first calculation and the steady-state second were performed using best-guess values for hydraulic conductivity of 1.40 x 10^{-15} m/s (permeability of

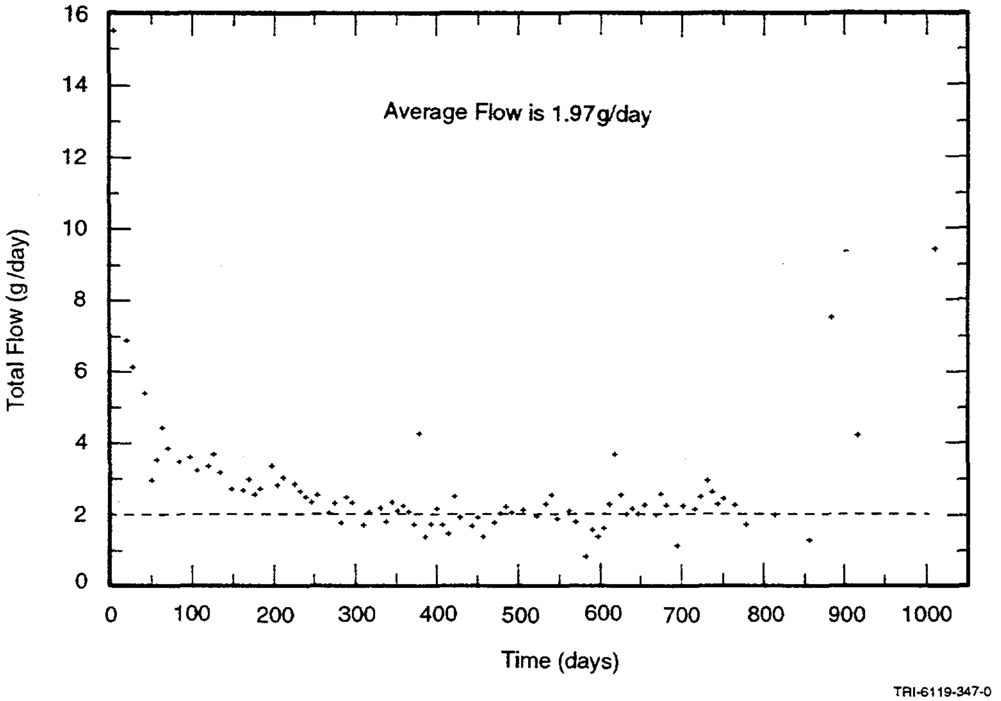

Figure 4-17. Average value of flow in DBT13 steady-state system.

2.46 x 10^{-22} m^2) and specific storage of 7.5 x 10^{-7} m^{-1} (specific capacitance of 6.3 x 10^{-11} Pa^{-1}). The hydraulic conductivity value is an average over various layers present in the borehole. From this calculation a steady-state mass flow rate of 1.86 g/day was obtained. Assuming that the flow rate was proportional to the hydraulic conductivity, a value of 1.48 x 10^{-15} m/s for hydraulic conductivity (permeability of 2.6 x 10^{-22} m^2) was established.

Linear proportionality between the mass flow rate and the hydraulic conductivity is possible only if the initial and boundary conditions were identical. In this simulation, the initial conditions were not critical because the second calculation was executed in a steady-state system. Boundary conditions reflect the values of hydraulic conductivity and specific storage used in the first calculation. The hydraulic conductivity of 1.48 x 10^{-15} m/s (permeability of 2.6 x 10^{-22} m^2) was determined without a complete accounting for the variation in the boundary conditions.

To verify this approximation and test its sensitivity to boundary conditions, additional calculations were performed with hydraulic conductivity values of 1.48 x 10^{-15} m/s (permeability of 2.6 x 10^{-22} m^2) and specific storage of 7.5 x 10^{-7} m^{-1} (specific capacitance of 6.3×10^{-11} Pa^{-1}). A mass flow rate of 1.97 g/day was obtained, which is equal to the measured flow in DBT13. This result indicates that the effect of the boundary conditions is negligible.

Using this value for permeability, several calculations were performed for the transient system, each time changing the value of the specific storage in order to minimize the average quadratic difference between calculated and measured flow rates. After a number of iterations, the best agreement was determined with specific storage of 8.0×10^{-7} m^{-1} (specific capacitance of 6.7×10^{-11} Pa^{-1}).

For further verification, a final simulation using the last pair of values where hydraulic conductivity = 1.48×10^{-15} m/s (permeability = 2.6×10^{-22} m^2) and specific storage = 8.0×10^{-7} m^{-1} (specific capacitance = 6.7×10^{-11} Pa^{-1}) was performed, and the simulated steady-state flow rate obtained was equal to that from the flow test conducted in DBT13. Thus the calculation method was assumed to be accurate.

For the other boreholes, the same value of specific storage (S_s) of 8.0×10^{-7} m^{-1} (specific capacitance of 6.7×10^{-11} Pa^{-1}) was used. Therefore, for holes DBT10, DBT11, and DBT12, only the average hydraulic conductivity value was determined by iterative calculations. The results were:

$K_{DBT10} = 5.09 \times 10^{-15}$ m/s (permeability = 8.95×10^{-22} m^2)
$K_{DBT11} = 6.02 \times 10^{-15}$ m/s (permeability = 1.06×10^{-21} m^2)
$K_{DBT12} = 1.97 \times 10^{-15}$ m/s (permeability = 3.46×10^{-22} m^2)

A different value of hydraulic conductivity was obtained for each borehole, reflecting the presence of different strata along the borehole. The brine flow on the inner surfaces of the boreholes is assumed to be nearly horizontal. The formula for average hydraulic conductivity is applied to determine the hydraulic conductivity of each layer.

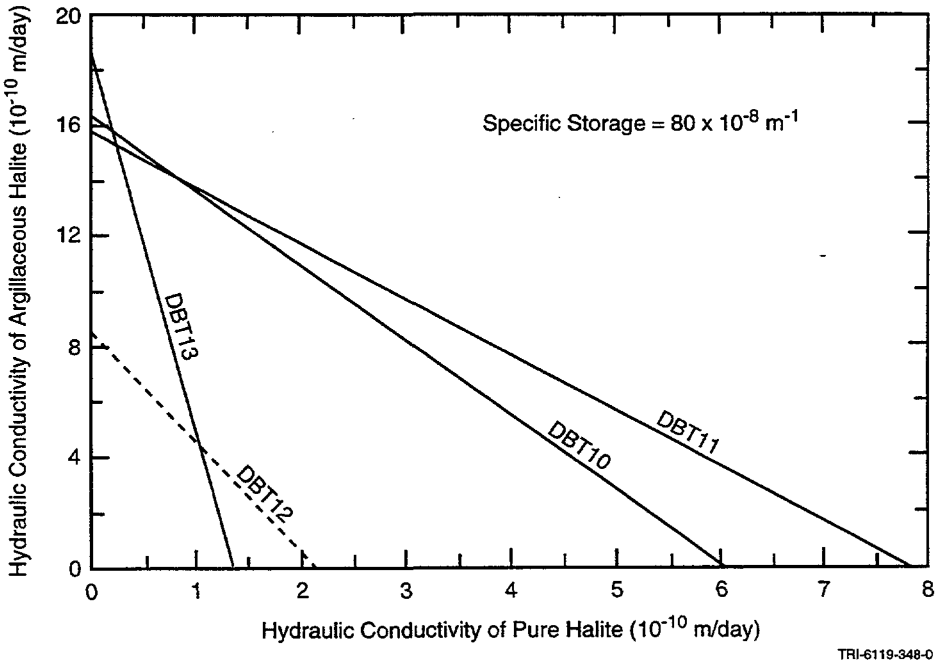

Figure 4-18. K_2 as a function of K_1.

$$K_{av} = \frac{\sum K_i b_i}{\sum b_i} \tag{4-13}$$

where:

K_{av} = average hydraulic conductivity
K_i = hydraulic conductivity of stratum i
b_i = thickness of stratum i

Application of this formula to the four boreholes resulted in a set of four equations with two unknowns, K_1 and K_2, which were, respectively, the hydraulic conductivities of pure halite and argillaceous halite. The following equations were obtained:

Hole DBT10: $3.81 \text{ m } K_1 + 1.41 \text{ m } K_2 = 2.6583 \times 10^{-14} \text{ m}^2\text{/s}$
Hole DBT11: $2.97 \text{ m } K_1 + 1.47 \text{ m } K_2 = 2.6722 \times 10^{-14} \text{ m}^2\text{/s}$
Hole DBT12: $2.81 \text{ m } K_1 + 0.72 \text{ m } K_2 = 6.9456 \times 10^{-15} \text{ m}^2\text{/s}$
Hole DBT13: $2.41 \text{ m } K_1 + 0.18 \text{ m } K_2 = 3.837 \times 10^{-15} \text{ m}^2\text{/s}$

The coefficients of K_1 in these equations represent the total thickness of the pure halite strata; those of K_2 correspond to the total thickness of the argillaceous halite strata. The right-hand numbers are the products of the borehole depths and the corresponding hydraulic conductivities.

Plotting the values for $K_2 = f(K_1)$ (Figure 4-18), produced three lines that cross at nearly the same point. The line corresponding to hole DBT12 was noticeably different. Nothing in the documentation for the *in situ* borehole tests provides any explanation for this difference in DBT12 relative to the other boreholes. Therefore, to avoid having the DBT12 result weigh too heavily on the determination of K_1 and K_2, it was omitted from subsequent calculations.

By a least-squares method, the values approached by K_1 and K_2 from the equations corresponding to holes DBT10, DBT11, and DBT13 were determined:

for pure halite:

$$K_1 = 3.35 \times 10^{-16} \text{ m/s (permeability} = 5.88 \times 10^{-23} \text{ m}^2)$$

for argillaceous halite:

$$K_2 = 1.77 \times 10^{-14} \text{ m/s (permeability} = 3.11 \times 10^{-21} \text{ m}^2)$$

These values were introduced to modify the average values of the hydraulic conductivities, using Eq. 4-13, to give:

$$K_{DBT10} = 5.02 \times 10^{-15} \text{ m/s (permeability} = 8.83 \times 10^{-22} \text{ m}^2)$$
$$K_{DBT11} = 6.09 \times 10^{-15} \text{ m/s (permeability} = 1.07 \times 10^{-21} \text{ m}^2)$$
$$K_{DBT13} = 1.54 \times 10^{-15} \text{ m/s (permeability} = 2.71 \times 10^{-22} \text{ m}^2)$$

The results of the calculations using these adjusted values for hydraulic conductivities can be compared to the experimental results. Plotting both calculated and observed data on the same graph produces satisfactory results (see Figures 4-19, 4-20, and 4-21). The best overall fit is obtained for hole DBT11. In contrast, variation in the steady-state phase was observed in the test of DBT10. This can perhaps be explained by a change in the microstructure of the salt which led to an increase in

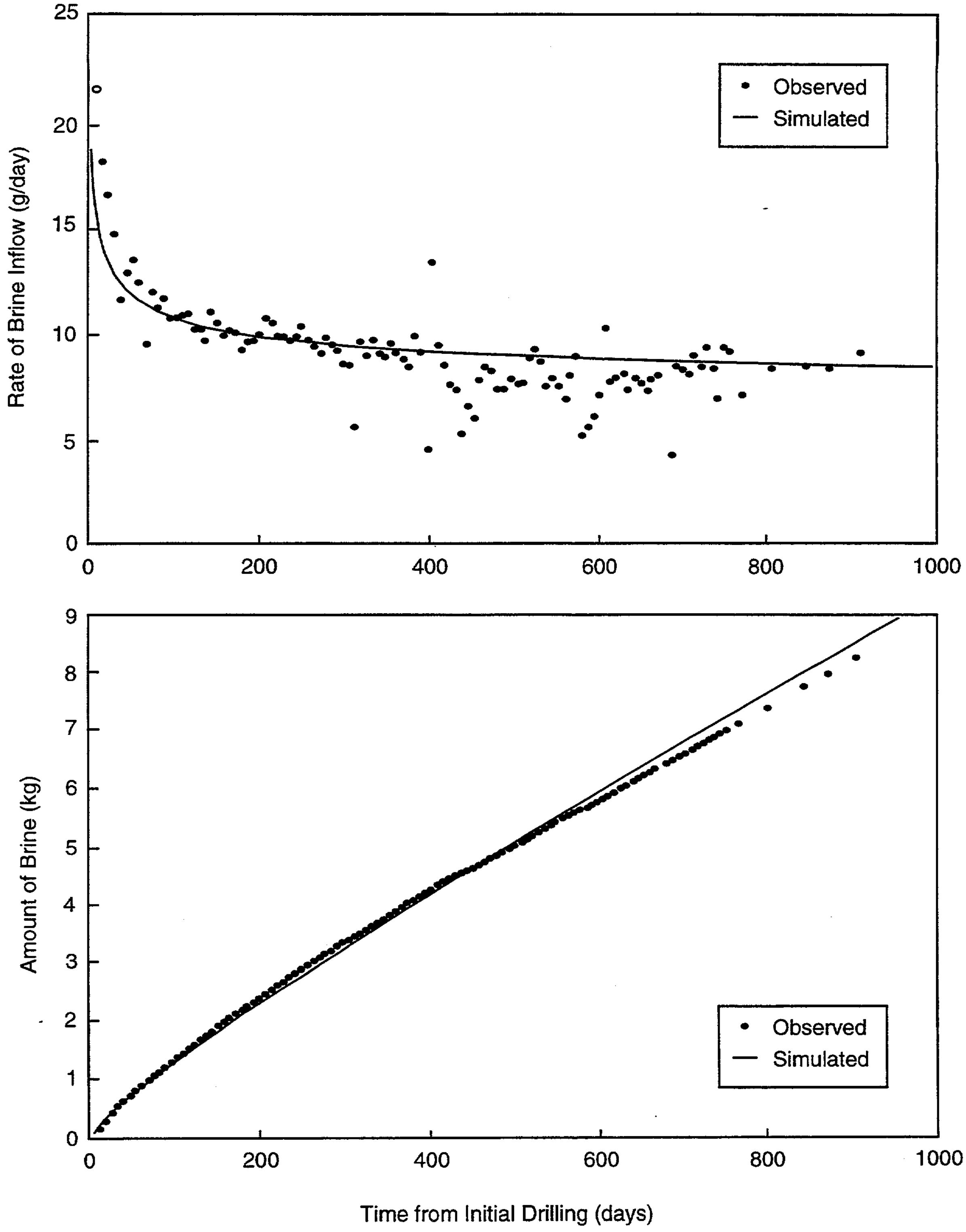

TRI-6119-350-0

Figure 4-19. Comparison of observed and EdM-calculated flow rates and volumes of borehole DBT10 for a period of 1000 days.

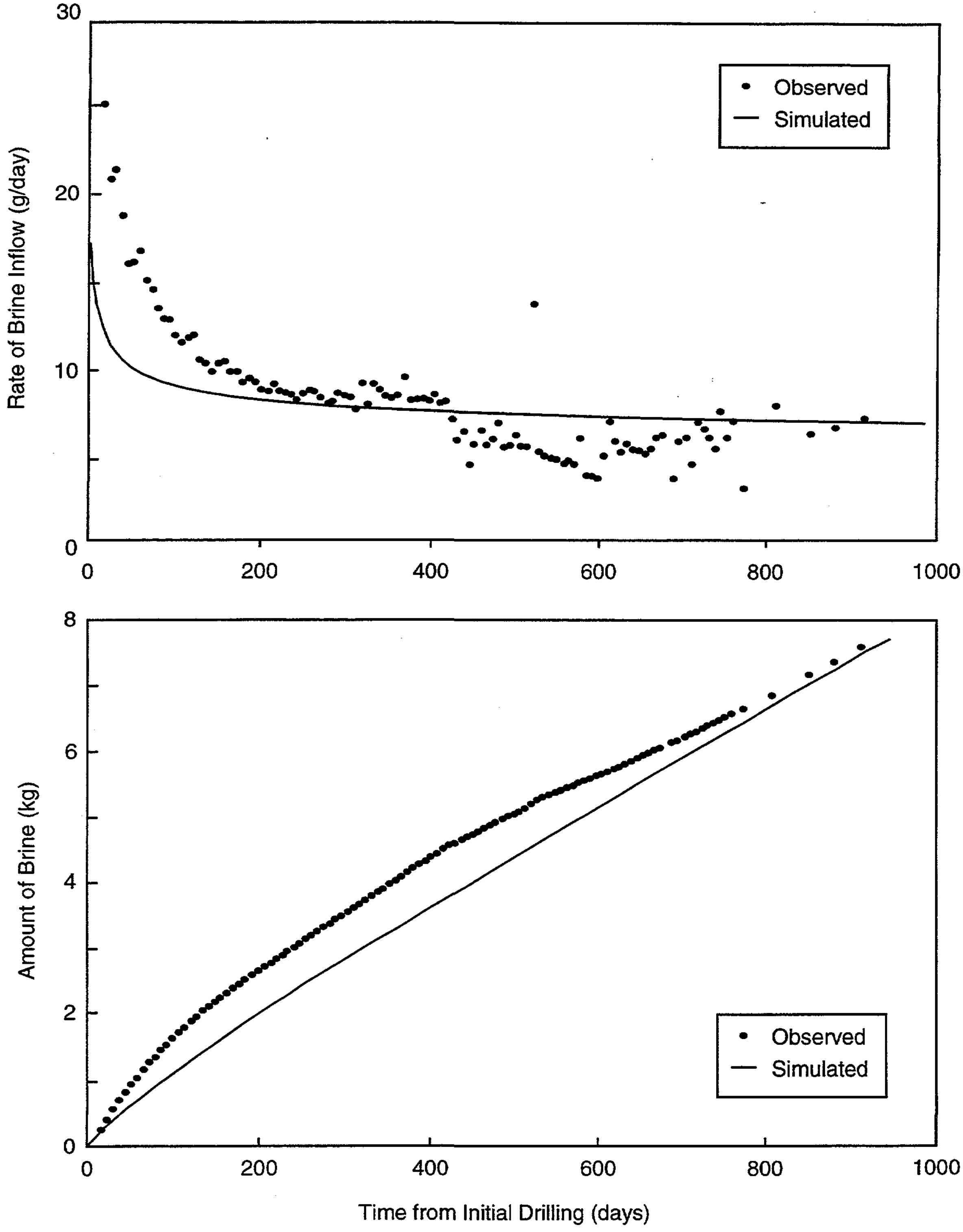

TRI-6119-392-0

Figure 4-20. Comparison of observed and EdM-calculated flow rates and volumes of borehole DBT11 for a period of 1000 days.

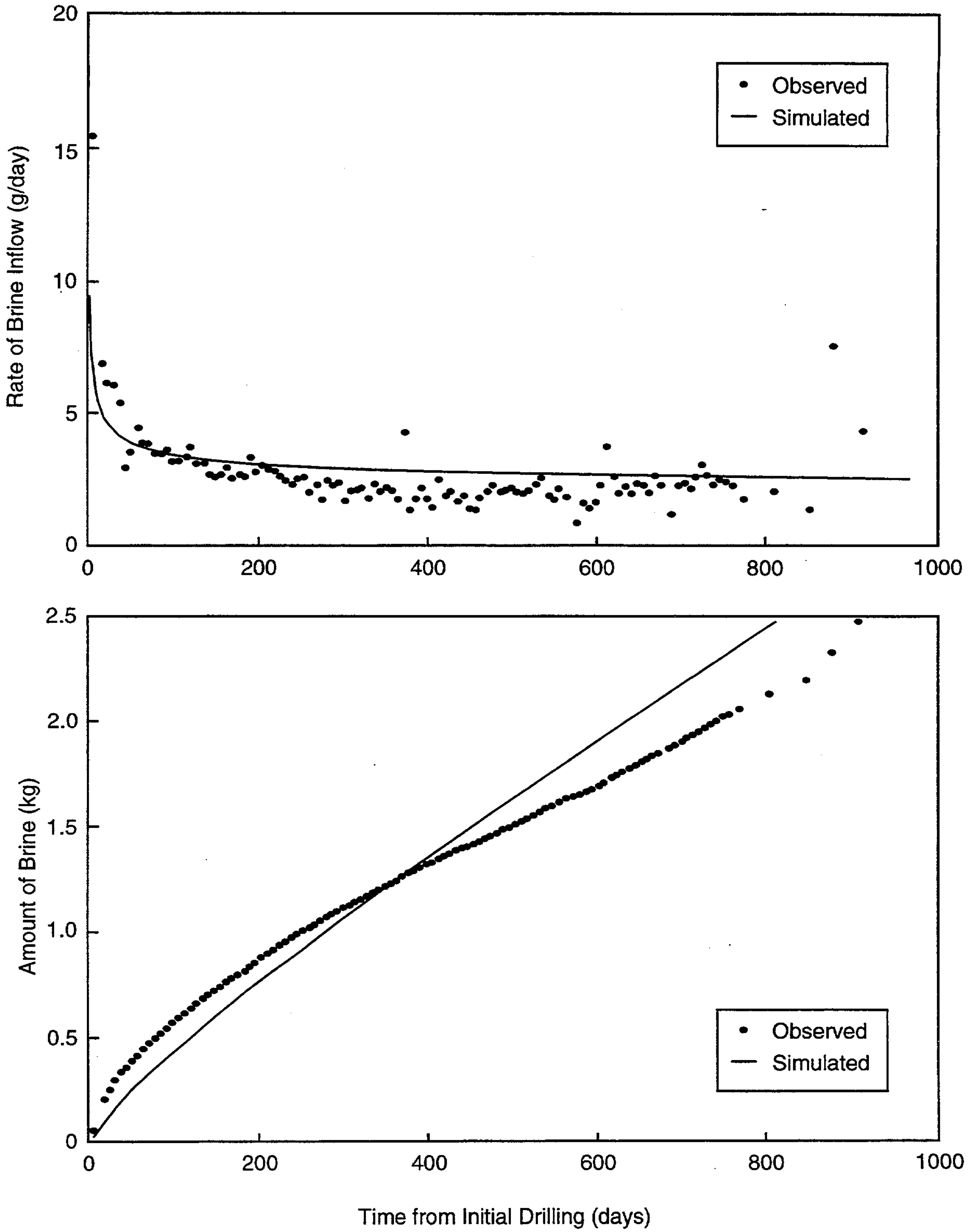

TRI-6119-393-0

Figure 4-21. Comparison of observed and EdM-calculated flow rates and volumes of Borehole DBT13 for a period of 1000 days.

hydraulic conductivity and specific storage. Recall that for these simulations the hydrogeologic parameters of the rock were assumed to remain constant over time, although certainly the excavation of Room D caused a change in these properties.

In an attempt to quantify the effect of ignoring the depressurization resulting from the excavation of Room D on the estimated hydraulic conductivity, a new calculation was performed assuming that the excavation did not modify the initial formation parameters. In this simulation, a single calculation beginning with an initially uniform hydraulic head was performed. At the top and bottom boundaries of the model, the imposed head was equal to the initial head. The hydraulic conductivity value that gave the best fit was determined from the simulation of the test of borehole DBT11:

$$K_{DBT11} = 5.5 \times 10^{-15} \text{ m/s (permeability} = 9.67 \times 10^{-22} \text{ m}^2\text{).}$$

When the disturbances caused by the excavation of Room D are ignored, the hydraulic conductivity is overestimated by about 10%. The effect of the room excavation on the hydraulic conductivity calculation is therefore not of great importance. This can be explained by the extremely low value of the diffusivity K/S_s. The effect of Room D on the pressure distribution at the start of the second calculation can be seen in Figure 4-22. The figure gives the initial head distribution as a function of distance from the lower boundary of the model. The distribution is considered constant along the x axis. The disturbance is very localized.

4.2.5 Problem Areas

The EdM study shows that the perturbation of the hydraulic head, caused by the excavation of Room D has no significant influence on the calculation of hydraulic conductivity. However, the effects of salt creep should be considered because these effects could explain the unexpected increase of the flow rate after apparently reaching steady state. As the salt creeps to fill the void left by the excavation of the room, stress concentrations are induced close to the room which might increase the pore pressure gradient, and dilation occurs which might increase the permeability of the rock mass. Therefore, when considering salt creep, permeability cannot be considered to be constant over time, and it becomes necessary to vary the parameters of Darcy's law with time.

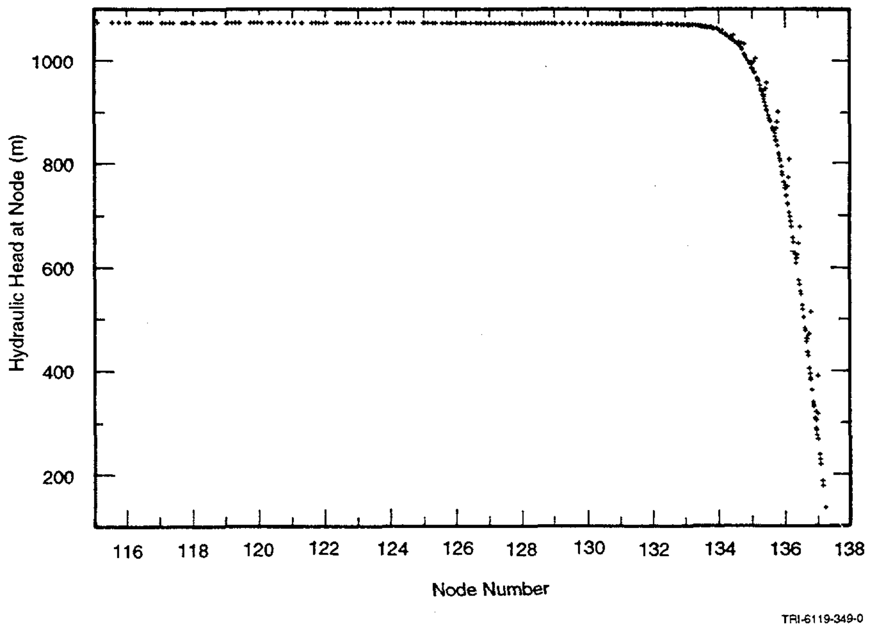

Figure 4-22. Calculated hydraulic head beneath the repository as a function of vertical position (see Figure 4-14).

Simulation of the brine-inflow tests can be improved by employing a coupled hydromechanical approach in which the rock mass is considered as a porous viscoplastic medium. Recent developments in the VIPLEF code, which is well adapted to solving rock mechanics, soil mechanics, thermal and hydraulic problems, will allow for such an approach either with a two- or three-dimensional model (Plischke, 1988).

4.3 SNL Project Team

Efforts by the Sandia project team to interpret the small-scale brine-inflow tests quantitatively were performed and reported by McTigue (1993). General studies of the effects of the nearby excavations on the experiments and evaluations of different approaches to test interpretation were performed and reported by Gelbard (1992) and Webb (1992), respectively.

4.3.1 Modeling Purpose/Strategy

McTigue (1993) estimated permeability and hydraulic diffusivity of the salt from the small-scale brine-inflow experiments by fitting a highly idealized one-dimensional model to the data. The model parallels conventional problems of flow in confined aquifers, assuming that brine seepage to the monitored boreholes is caused by relaxation of ambient pore pressure by Darcy flow. The model assumes halite is a linearly elastic medium with time-invariant permeability. The data from each hole were fit by a least-squares method.

The numerical model of McTigue (1993) was based on data collected through mid-January 1990, before brine-inflow rates began to rise in some holes. The observed cumulative volume and flux histories provided the data to which the model was fit. The fits sought the set of unknown parameters that minimized the difference between the observations and the model calculations. The model is described in Section 4.3.3.

4.3.2 Code Used

The fits reported here for the full-flux and cumulative-volume histories were performed with the parameter-estimation code ESTIM (Hills, 1987). The code seeks the set of model parameters that minimizes the sum of squares of residuals, or differences between observed and simulated quantities. In the present case, the data used are either brine flux or cumulative brine volume. The simulations are numerical evaluations of the exact solutions for radial seepage to a long hole.

Programs that evaluate the functions describing seepage to a borehole are called as subroutines by ESTIM. Each of the analytical functions is a two-parameter description of the flow; one parameter scales the magnitude of the flux or volume, and the other is a characteristic time over which the flow evolves. With few exceptions, the observed flow rates fall in a reasonably narrow range. Thus, the product of permeability and initial pressure is fairly well constrained in most cases. However, the detailed history of the flux for many holes was somewhat erratic, so fits for the diffusivity are more uncertain.

ESTIM employs a local least-squares method whereby the code seeks a local minimum in the sum of squares of residuals as a function of the unknown parameters. In general, experience with the present data suggests that the minimum local to a reasonable initial estimate of the parameters is the desired global minimum. ESTIM requires as input a set of initial estimates for the parameters to be determined, as well as upper and lower bounds on their possible values. At each iteration, the code constructs a sensitivity matrix consisting of the partial derivatives of the error measure, which is the sum of squares of residuals, with respect to the unknown parameters. These derivatives were approximated from all calculations by first-order differences. ESTIM then employs a quadratic least-squares method to optimize the parameter estimates.

The parameter estimation code includes an option to perform a propagation of variance analysis. This option was exercised for the fits to the full flux histories reported here; it was not used for the cumulative-volume fits. The analysis provides a measure of the sensitivity of the estimated parameters to small random errors in the data. The standard deviations returned by ESTIM are estimates of the true standard deviations, as described in Hills (1987).

For the propagation of variance performed on the analysis of the full flux histories, the measurement error is assumed uniform for every sampling interval in each borehole among the entire group. In particular, the standard deviation of the measurement of mass of brine collected was assumed to be ±5 g for each sample taken. For a uniform, seven-day sample interval, this corresponds to a measurement error of ±0.71 g/d on the total mass flow rate, which is comparable to the error estimates reported by Finley et al. (1992), based on laboratory repeatability tests and on a detailed statistical analysis of the field data by Rutherford (1992). This estimate for the error in the measured mass flow rate was then divided by the brine density and the borehole wall area for each hole to yield an estimate of the error in the flux. ESTIM returns normalized standard deviations to each parameter, which are then multiplied by the corresponding error estimate for the raw data to yield the standard deviation associated with each parameter in a given fit.

4.3.3 Modeling Approach

The model that underlies much of classical hydrology results in a linear diffusion equation for the excess pore pressure or, equivalently, hydraulic head in the fluid. The equation used here, the derivation of which is discussed in detail in McTigue (1993), is

$$c\frac{\partial p}{\partial t}-\frac{k}{\mu}\nabla^2 p=0 \tag{4-14}$$

Hydraulic diffusivity, c, is defined as

$$c=\frac{k}{\mu\, C_s} \tag{4-15}$$

C_s, the specific capacitance, is given as

$$C_s=C'\left[1-\frac{2(1-2\upsilon)}{3(1-\upsilon)}\frac{K_m B'^2}{C'}\right] \tag{4-16}$$

where:

$$C'=\frac{1}{K_m}\left(1-\frac{K_m}{K_s}\right)+\frac{\phi_0}{K_f}\left(1-\frac{K_f}{K_s}\right) \tag{4-17}$$

$$B'=\frac{1}{K_m}\left(1-\frac{K_m}{K_s}\right) \tag{4-18}$$

Eq. 4-14 is fundamental to classical hydrology, although it often appears in terms of head rather than pressure. The identity is made by defining the head $h=p/\gamma_{f0}\mathbf{g}$, so that Eq. 4-14 becomes:

$$S_s \frac{\partial h}{\partial t} - K\nabla^2 h = 0 \qquad (4\text{-}19)$$

where:

$S_s = \gamma_{f0} \mathbf{g} C_s$ is the specific storage, and

$K = k\gamma_{f0} \mathbf{g}/\mu$ is the hydraulic conductivity.

ANISOTROPY

The flow to a circular borehole of finite length and bounded on one end by a plane surface is a two-dimensional problem, even when axisymmetry can be supposed. However, if the permeability is strongly anisotropic, which is often the case in geological materials, the flow can be predominantly in planes normal to the axis of a vertical borehole.

The flow to an open borehole is idealized here as a one-dimensional process (i.e., radial flow occurs in planes normal to the borehole axis). In this configuration, the assumption of isotropy of the hydraulic properties can be viewed as the somewhat less restrictive assumption of *transverse* isotropy. For example, note that no flow was observed in the two sub-horizontal holes drilled from Room D, while eight vertical holes in the same area produced brine. This can be interpreted as an indication of flow confined predominantly to horizontal planes, perhaps corresponding to compositional or mechanical layering in the rock.

PRESSURE FIELD IN RADIAL FLOW MODEL

The radial flow model assumes that an open, circular hole is introduced into an unbounded, homogeneous domain at time $t = 0$. A definition sketch of the model is shown in Figure 4-23. The initial fluid pressure, p_∞, is assumed to be uniform. The open face of the borehole is at atmospheric pressure, $p = 0$, causing flow toward the hole, associated with relaxation of the pressure in a zone that grows diffusively outward from the hole. The exact statement of the initial-value problem is (from Eq. 4-14):

$$\frac{\partial p}{\partial t}-\frac{c}{r_i}\frac{\partial}{\partial r_i}\left(r_i\frac{\partial p}{\partial r_i}\right)=0 \tag{4-20}$$

with initial condition:

$$p(r_i,0)=p_\infty \tag{4-21}$$

and boundary conditions:

$$p(r_w,t)=0 \tag{4-22}$$

$$\lim_{r_i\to\infty} p(r_i,t)=p_\infty \tag{4-23}$$

An analytical solution to Eqs. 4-20 through 4-23 is well known:

$$\frac{p}{p_\infty}=-\frac{2}{\pi}\int_0^\infty \exp\left(-u^2 t_*\right)\mathrm{f}\left(u;r_{i^*}\right)\frac{du}{u} \tag{4-24}$$

where

$$\mathrm{f}\left(u;r_*\right)=\frac{J_0\left(ur_*\right)Y_0\left(u\right)-Y_0\left(ur_*\right)J_0\left(u\right)}{J_0^2\left(u\right)\;+\;Y_0^2\left(u\right)} \tag{4-25}$$

and where:

$$t_*=\frac{ct}{r_w^2} \tag{4-26}$$

$$r_*=\frac{r_i}{r_w} \tag{4-27}$$

Although Eq. 4-24 is a closed-form solution to the problem, it is difficult to evaluate accurately because the integrand is singular at the lower limit of integration. However, the singularity is integrable, so that Eq. 4-24 can be evaluated accurately if appropriate care is taken.

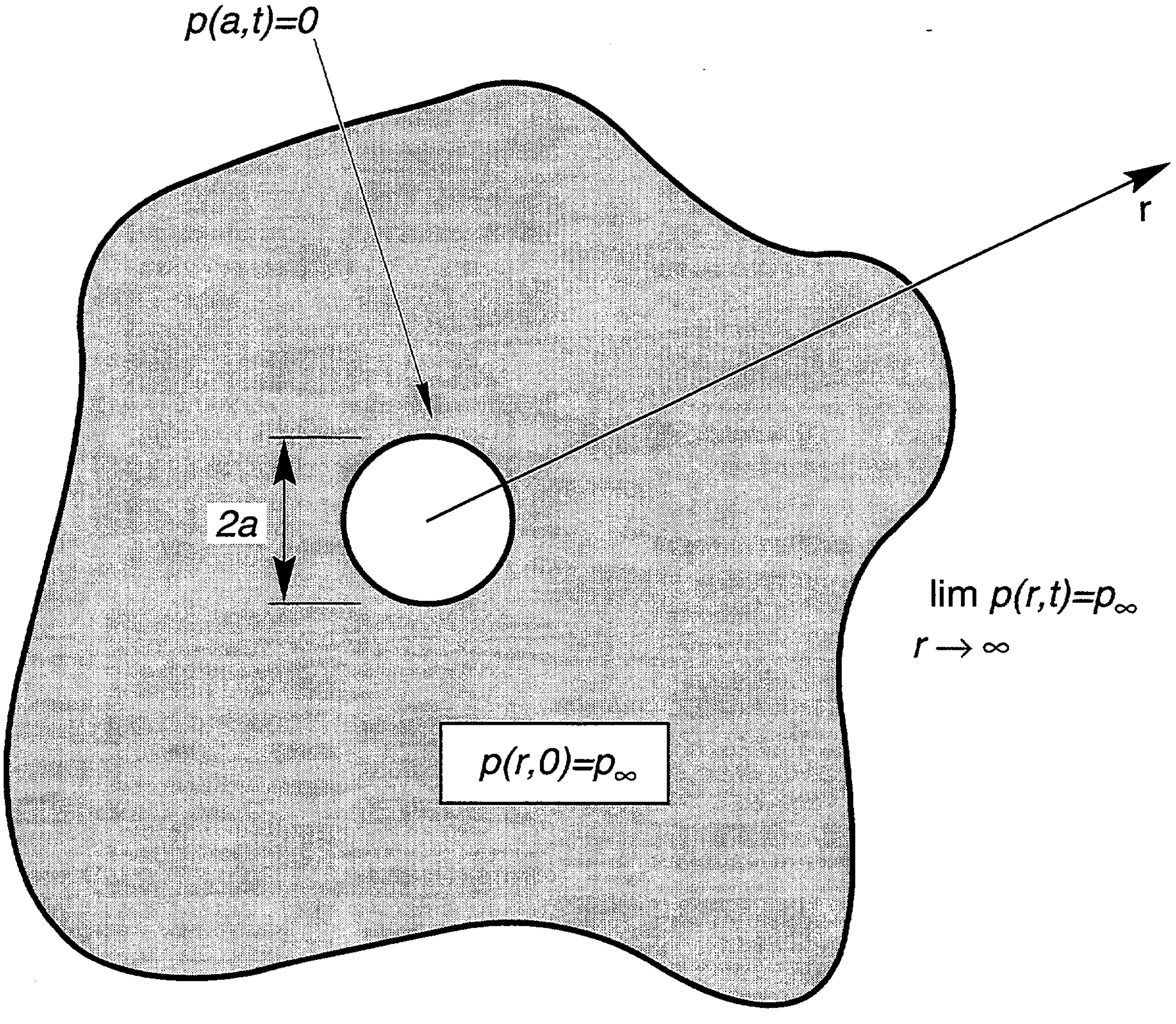

TRI-6119-276-0

Figure 4-23. Definition sketch for radial flow to a borehole.

To isolate the singular part of the integrand, the integral in Eq. 4-24 can be partitioned into two parts:

$$\frac{p}{p_\infty} = \frac{2}{\pi}\int_0^\varepsilon \exp\left(-u^2 t_*\right) \mathrm{f}\left(u;r_*\right)\frac{du}{u} - \frac{2}{\pi}\int_\varepsilon^\infty \exp\left(-u^2 t_*\right) \mathrm{f}\left(u;r_*\right)\frac{du}{u} \tag{4-28}$$

where ε can be chosen to be arbitrarily small. The expansions of $J_0(\varsigma)$ and $Y_0(\varsigma)$ for small arguments are given by:

$$J_0(\varsigma) = 1 - \frac{\varsigma^2}{4} + \ldots \tag{4-29}$$

$$Y_0(\varsigma) = \frac{2}{\pi}\left(1 - \frac{\varsigma^2}{4}\right)\ln\left(\frac{\beta\varsigma}{2}\right) + \ldots \tag{4-30}$$

where $\beta = \exp(\gamma)$, and $\gamma = 0.5772\ldots$ is Euler's constant. Substitution of Eqs. 4-29 and 4-30 into the first integral in Eq. 4-28, and expansion about $u = 0$ gives, to leading order:

$$\lim_{u\to 0} -\frac{2}{\pi}\int_\pi^\varepsilon \exp\left(-u^2 t_*\right) \mathrm{f}\left(u, r_*\right)\frac{du}{u} = \ln r_* \int_0^\varepsilon \frac{\exp\left(-u^2 t_*\right)}{\ln^2(\beta\, u/2)}\frac{du}{u} + \ldots \tag{4-31}$$

The right side of Eq. 4-31 can be integrated by parts to yield:

$$\lim_{u\to 0} -\frac{2}{\pi}\int_0^\varepsilon \exp\left(-u^2 t_*\right) \mathrm{f}\left(u, r_*\right)\frac{du}{u} = -\frac{\exp\left(-\varepsilon^2 t_\circ\right) \quad \ln r_*}{\ln\left(\beta\, e/2\right)} + 0\left(\frac{\varepsilon^2 t_*}{\ln\varepsilon}\right) \tag{4-32}$$

Thus, Eq. 4-24 can be evaluated accurately by separating the singular part of the integrand, integrating it analytically, and evaluating the remainder by numerical quadrature. Substitution of Eq. 4-32 into Eq. 4-28 gives the final form used:

$$\frac{p}{p_\infty} \cong -\frac{\exp\left(-\varepsilon^2 t_*\right)\ln r_*}{\ln\left(\beta\,\varepsilon/2\right)} - \frac{2}{\pi}\int_\varepsilon^\infty \exp\left(-u^2 t_*\right) \mathrm{f}\left(\mathrm{u};\mathrm{r}_*\right)\frac{du}{u} \tag{4-33}$$

Evaluations of Eq. 4-33 have been carried out, setting $\varepsilon = 10^{-8}$, and performing the integral by the Gauss quadrature routine DGAUS8 in the SLATEC subroutine package.

The error tolerance in the numerical integrator was set to ERR = 10^{-6}, and the calculations were carried out on a VAX 8650 using double-precision arithmetic. Figure 4-24 shows Eq. 4-33 evaluated for $1 \le r_* \le 5$ and $t_* = 0.01, 0.1, 0.5, 1.0, 5.0, 10.0$, and 50.0. The results shown here differ slightly from those reported by Nowak and McTigue (1987) and Nowak et al. (1988) because of the more careful treatment of the integral in Eq. 4-24 near $u = 0$. The most significant differences are evident at later times and larger radial coordinates, where the pressures are typically somewhat larger than in the original calculations. Thus, the numerical quadrature applied directly to Eq. 4-24 appears to underestimate the contribution near the singularity.

FLUID FLUX AT THE BOREHOLE

A quantity that can be estimated from field data is the flux into the hole, $\mathbf{q}_r(r_w,t)$, which can be obtained from Eq. 4-24 by application of Darcy's law:

$$\mathbf{q}_r(r_w,t) = -\frac{k}{\mu}\frac{\partial p}{\partial r_i}(r_w,t) \tag{4-34}$$

The resulting expression has been noted previously by Nowak and McTigue (1987) and Nowak et al. (1988):

$$\mathbf{q}_* = \frac{4}{\pi^2}\int_0^\infty \frac{\exp\left(-u^2 t_*\right)}{J_0^2(u)+Y_0^2(u)}\frac{du}{u} \tag{4-35}$$

where: $\mathbf{q}_*$ is the magnitude of the normalized flux at the borehole, and where $\mathbf{q}_* = |\mathbf{q}_r|(r_w,t)/\mathbf{q}_0 = -\mathbf{q}_r\,(r_w,t)/\mathbf{q}_0$, and the scale of the flux, $\mathbf{q}_0$, is given by $\mathbf{q}_0 = kp_\infty/\mu\, r_w$.

Eq. 4-35 experiences the same difficulty noted previously in the discussion of the pressure profiles: the integrand is singular at $u = 0$, and numerical quadrature routines cannot easily resolve this. However, the singularity is of the same form as that in Eq. 4-24, and is therefore integrable. The identical procedure can be applied to Eq. 4-35. However, the same result can be achieved by differentiating Eq. 4-33 directly, giving:

$$\mathbf{q}_* \cong -\frac{\exp\left(-\varepsilon^2 t_*\right)}{\ln(\beta\,\varepsilon/2)} + \frac{4}{\pi^2}\int_\varepsilon^\infty \frac{\exp\left(-u^2 t_*\right)}{J_0^2(u)+Y_0^2(u)}\frac{du}{u} \tag{4-36}$$

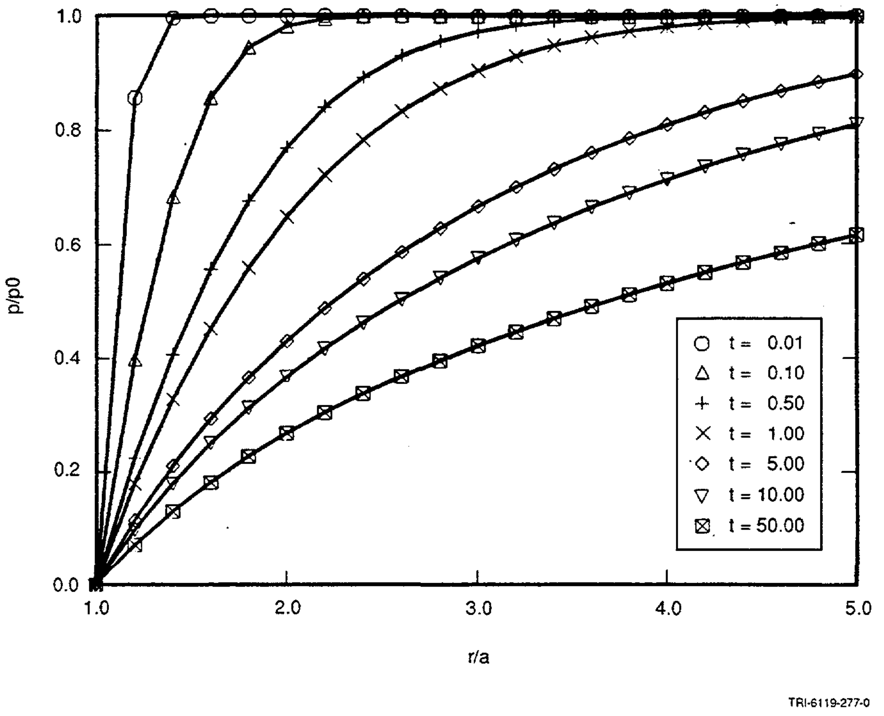

Figure 4-24. Pore pressure profiles at various times based on Eq. 4-33; radial coordinate, *r*, is normalized by borehole radius, *a*; pressure, *p*, is normalized by initial value p_∞.

Evaluations of Eq. 4-36 have been carried out in the same fashion as those of Eq. 4-33 described above, again taking $\varepsilon = 10^{-8}$ and ERR = 10^{-6}. Over a range of t_* from 0.01 to 0.8, the results are identical within three decimal places to values given by Jaeger and Clarke (1942-43).

CUMULATIVE VOLUME

The cumulative volume of fluid per unit area of borehole wall, *V*, is obtained by integrating Eq. 4-36 over time:

$$V_* \cong -\frac{t_*}{\ln(\beta\varepsilon/2)} + \frac{4}{\pi^2}\int_\varepsilon^\infty \frac{\left[1-\exp\left(-u^2 t_*\right)\right]}{J_0^2(u)+Y_0^2(u)}\frac{du}{u^3} + 0\left(\frac{\varepsilon^2\, t_*^2}{\ln\varepsilon}\right) \tag{4-37}$$

where:

$V_* = V/V_0$, and
$V_0 = kp_\infty r_w/\mu c = C_s p_\infty r_w$ is the reference volume scale.

LATE-TIME ASYMPTOTIC FLUX

The asymptotic expansion of Eq. 4-35 for $t_* \gg 1$ takes a particularly simple form useful for fitting data. The development is reproduced here in detail.

In order to find the late-time, asymptotic expansion of the fluid flux (Eq. 4-35), let $\eta^2 = u^2 t_*$, so that large t_* corresponds to small arguments of the Bessel functions. Introduce the appropriate expansions for small argument from Eqs. 4-29 and 4-30, and expand the integrand:

$$\lim_{t_* \to \infty} q_* = \int_0^\infty \frac{\exp(-\eta^2)}{\left[\ln(\beta\eta/2t_*^{1/2})\right]^2}\left[1 - \frac{\pi^2/4}{\left[\ln(\beta\eta/2t_*^{1/2})\right]^2} + \ldots\right]\frac{d\eta}{\eta}$$

$$+\frac{1}{2t_*}\int_0^\infty \frac{\eta\exp(-\eta^2)}{\left[\ln(\beta\eta/2t_*^{1/2})\right]^2}d\eta + \ldots \tag{4-38}$$

where $\beta = \exp(\gamma)$ and $\gamma = 0.5772\ldots$ is Euler's constant. Integration of each term in Eq. 4-38 by parts yields:

$$\lim_{t_* \to \infty} q_* = -2\int_0^\infty \frac{\eta\exp(-\eta^2)}{\ln(\beta\eta/2t_*^{1/2})}\left[1 - \frac{\pi^2}{6}\left(\eta^4 - 3\eta^2 + 1 + \ldots\right)\right]d\eta \tag{4-39}$$

$$-\frac{1}{t_*}\int_0^\infty \frac{\eta(\eta^2-1)\exp(-\eta^2)}{\ln(\beta\eta/2t_*^{1/2})}d\eta + \ldots$$

Expansion of $1/\ln(\beta\eta/2t_*^{1/2})$ in powers of $1/\ln(4t_*/\beta^2)$ gives:

$$\frac{1}{\ln\left(\beta\eta/t_*^{1/2}\right)} = -\frac{2}{\ln\left(4t_*/\beta^2\right)}\left[1+\frac{2\ln h}{\ln\left(4t_*/\beta^2\right)}+\frac{4(\ln\eta)^2}{\left[\ln\left(4t_*/\beta^2\right)\right]^2}+\dots\right] \tag{4-40}$$

Substitution of Eq. 4-40 into Eq. 4-39 and term-by-term integration yields:

$$\begin{aligned}\lim_{t_*\to\infty} \mathbf{q}_* = {} & \frac{2}{\ln\left(4t_*/\beta^2\right)}\left[1-\frac{\gamma}{\left[\ln\left(4t_*/\beta^2\right)\right]}+\frac{\left(\frac{\pi^2}{6}+\gamma^2\right)}{\left[\ln\left(4t_*/\beta^2\right)\right]}+\dots\right]-\frac{2\pi^2/3}{\ln\left(4t_*/\beta^2\right)} \\ & \left[0+0+\frac{1}{\left[\ln\left(4t_*/\beta^2\right)\right]^2}+\dots\right]+\frac{2/t_*}{\ln\left(4t_*/\beta^2\right)}\left[0+\frac{1/2}{\ln\left(4t_*/\beta^2\right)}+\dots\right]\end{aligned} \tag{4-41}$$

Combination of the first four nonzero terms in Eq. 4-41, and neglect of the smaller term of order $t_*^{-1}\ln^{-2}(t_*)$, yields the final result:

$$\lim_{t_*\to\infty} \mathbf{q}_* = \frac{2}{\ln\left(4t_*/\beta^2\right)}\left[1-\frac{\gamma}{\ln\left(4t_*/\beta^2\right)}-\frac{\left(\frac{\pi^2}{6}-\gamma^2\right)}{\left[\ln\left(4t_*/\beta^2\right)\right]^2}+\dots\right] \tag{4-42}$$

Figure 4-25 shows an evaluation of the full integral solution for the flux from Eq. 4-36, along with the late-time approximations based on Eq. 4-42. It is evident by inspection of Figure 4-25 that one or two terms of the series given by Eq. 4-42 capture the general trend of the exact solution at late time, but overestimate the flux somewhat. The two-term expansion yields a flux that is 5% too high at $t_* = 100$ and 3% too high at $t_* = 1000$. The three-term expansion is very close (less than 2% error) for $t_* > 100$.

A simple scheme for fitting data to extract hydraulic properties is suggested by taking the inverse of Eq. 4-42:

$$\lim_{t_*\to\infty} \mathbf{q}_*^{-1}\,\frac{1}{2}\ln\left(\frac{4t_*}{\beta^2}\right)\left[1+\frac{\gamma}{\ln\left(4t_*/\beta^2\right)}+\frac{\pi^2/6}{\left[\ln\left(4t_*/\beta^2\right)\right]^2}+\dots\right] \tag{4-43}$$

Retaining the first two terms in Eq. 4-43 (i.e., neglecting the term of $[\ln^{-1}(4t_*/\beta^2)]$ and returning to dimensional variables, this takes the convenient form:

$$\lim_{t_* \to \infty} |\mathbf{q}_r|^{-1}(r_w, t) = A \ln t + B \tag{4-44}$$

where:

$$A = \frac{\mu\, r_w}{2kp_\infty} \tag{4-45}$$

and

$$B = A \ln\left(\frac{4c}{r_w^2 \beta}\right) \tag{4-46}$$

Thus, a plot of the inverse flux at the borehole versus ln t is approximately linear at sufficiently late time. The slope, A, is an indicator of the permeability, and the intercept, B, is an indicator of the hydraulic diffusivity through the simple relations:

$$k = \frac{\mu\, r_w}{2p_\infty A} \tag{4-47}$$

and

$$c = \frac{r_w^2 \beta}{4} \exp\left(\frac{B}{A}\right) \quad \text{(two - term expansion)} \tag{4-48}$$

Note that, if only the first term of the expansion given in Eq. 4-43 is retained, Eq. 4-48 is replaced by:

$$c = \frac{r_w^2 \beta^2}{4} \exp\left(\frac{B}{A}\right) \quad \text{(leading order)} \tag{4-49}$$

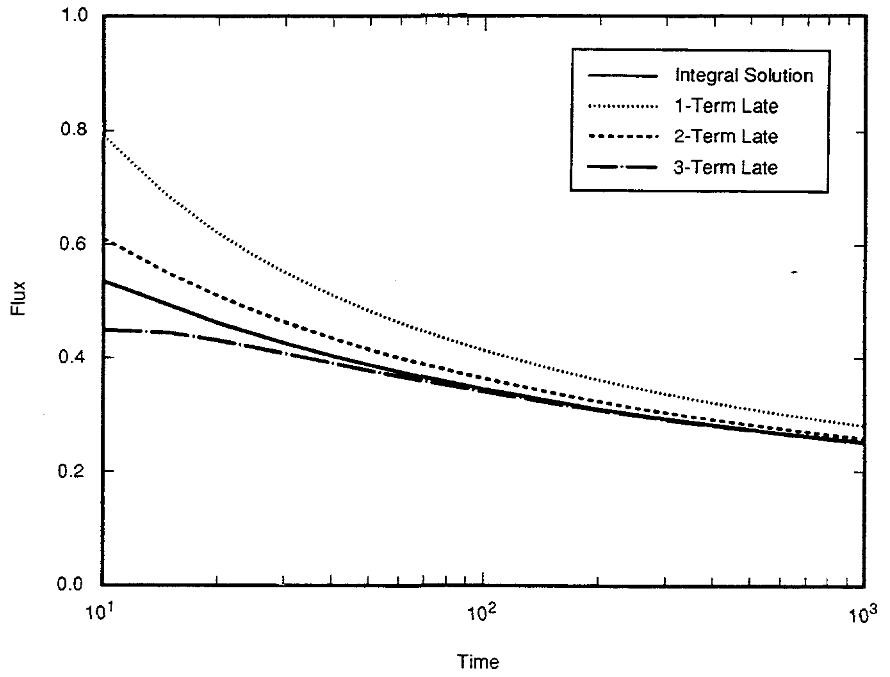

Figure 4-25. Comparison of late-time approximations (Eq. 4-42) and "exact" solution (Eq. 4-36) for fluid flux at a borehole; time, *t*, is normalized by characteristic diffusion time, a^2/c; flux, $|q_r|(a,t)$, is normalized by $q_0 = kp_\infty/\mu a$.

Thus, the higher-order approximation simply shifts the curve upward by a constant, A_γ. As a result, a fit based on only the first term in Eq. 4-43 will yield an estimate for the diffusivity (Eq. 4-49) that is a factor of $\beta \approx 1.78$ times greater than that obtained in view of the two-term expansion (Eq. 4-48).

Figure 4-26 shows a plot of inverse flux versus the logarithm of time for $t_* > 10$. The open symbols are computed from evaluations of the exact, integral solution. The lines show one, two, and three terms of Eq. 4-43. As noted above, both the leading-order approximation and the next, higher-order approximation are linear on this plot, with the latter simply shifted upward by a constant. Eq. 4-48 will give a better estimate of the hydraulic diffusivity than will Eq. 4-49, but Eq. 4-48 still tends to overestimate *c*. A nonlinear fit of the three-term series given in Eq. 4-43 would give a much better result and, although more involved than a linear regression based on the first two terms, is still far easier to perform than a fit requiring numerical quadrature on Eq. 4-36.

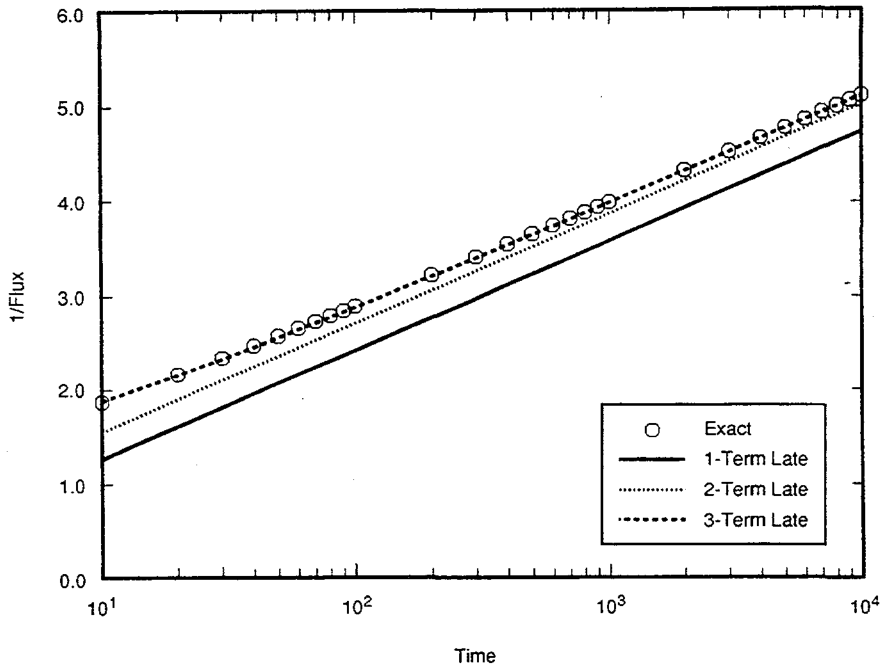

TRI-6119-280-0

Figure 4-26. Comparison of "exact" and late-time, asymptotic solutions for inverse of borehole flux; time, t, is normalized by characteristic diffusion time, a^2/c; flux, $|q_r|\,(a,t)$, is normalized by $q_0 = kp_\infty/\mu a$.

The inverse-flux fitting method was tested using synthetic data generated by numerical simulations of radial flow (Webb, 1992). Although the permeabilities used in the simulations were recovered with very good accuracy, typically within a few percent, the diffusivities estimated using Eq. 4-48 were typically overestimated by factors of about 50%. This difficulty is inherent in the method because extrapolation of the late-time fit back to ln $t = 0$ introduces significant error (Jaeger, 1958).

A good estimate of the diffusivity from late-time data is difficult to obtain if other processes affect the flow at early time. For example, suppose that the early-time flow is delayed by the growth of microcracks, dilatation, and resultant retentive storage of brine. After some time, the flow may behave in the classical fashion, and the slope of the $|\mathbf{q}|^{-1}$ versus ln t plot would reflect the permeability. However, the time should be "re-zeroed" to account for the delay. Without some rational basis for such a correction, the diffusivity inferred by this method is inherently unreliable if processes not accounted for are significant.

4.3.4 Results

FITS BASED ON THE FLUX HISTORIES

The principal emphasis of McTigue's work was to obtain fits based on the complete history of the brine flux for each borehole through mid-January 1990. Fits to the flux are believed to yield the most significant information with regard to the hydraulic diffusivity. The least-squares fitting routine tends to place greater weight on the larger numerical values in a given data set. Because the flux is maximum at early time, fits to the flux data tend to weight the early-time response. The flow changes most rapidly at early time, so that the most important information with regard to the evolution of the flow through time, which is characterized by the diffusivity, is contained in the early-time data.

One disadvantage of fitting the flux is that the data reduction entails an approximation to obtain flow rates. In particular, the field sampling program yields the cumulative volume over the sampling interval. In the present case, the mean flow rate over the sampling interval (an exact quantity) was calculated and assigned to a time corresponding to the midpoint of the interval (an approximation). This approximation is acceptable when the rate of change of flow rate as well as the sampling interval are relatively small. A second disadvantage to fitting the flux is that the data often exhibit considerable scatter; that is, while the cumulative volume must always be a non-decreasing sequence of data and often is reasonably smooth, the discrete approximations to its derivative can be highly variable. The least-squares routine can encounter difficulty fitting data with large scatter.

Results of McTigue's (1993) fits to the flux histories using Eq. 4-36 are shown in Figures 4-27 through 4-31 and summarized in Table 4-4. The permeabilities resulting from the fits fall in a reasonably narrow range, typically of order 10^{-21} m^2. The diffusivities, however, are widely distributed, with most in the range 10^{-10} to 10^{-8} m^2/s, reflecting variability in the time evolution of the seepage from hole to hole. The uncertainties, too, are typically greater for the diffusivities than for the permeabilities, again reflecting significant departures of the flux histories from the model behavior.

The parameter-estimation code ESTIM returns error estimates for the permeability and the diffusivity in the form $k \pm \lambda_k$ and $c \pm \lambda_c$, respectively. The error estimates for the specific capacitance, λ_{C_s}, are computed from:

$$\lambda_{C_s}^2 = C_s^2 \left[\left(\frac{\lambda_k}{k} \right)^2 + \left(\frac{\lambda_c}{c} \right)^2 \right] \tag{4-50}$$

The analysis treats the brine density, brine viscosity, and borehole radius and length as known constants; the error estimates do not include the contributions due to uncertainty in these parameters. However, such contributions are small compared to the uncertainty in the flux and volume measurements, and the ability of the idealized model to match the data.

FITS BASED ON THE CUMULATIVE VOLUME HISTORIES

Fits based on the cumulative volume history for each hole are derived from Eq. 4-37. This approach offers two advantages over fitting data for the flux. First, the raw data are in the form of the volume collected in each sampling. Thus, data for cumulative volume versus time can be constructed directly, rather than involving some sort of approximation in the assembly of the data. Second, the data for cumulative volume are much smoother than those for the flow rate. The cumulative volume is, by definition, a non-decreasing function, while approximations to its derivative with respect to time can be highly variable.

Fits to the flux and to the cumulative volume for the same borehole will yield somewhat different parameter values, in part due to the different weights given to different portions of the data in the two schemes. In particular, a fit to the cumulative volume tends to weight the late-time data, when the volume is large, while a fit to the flux tends to weight the early-time data, when the flux is large.

The fits to the cumulative volume data were again performed with the parameter-estimation code ESTIM. A subroutine was written to evaluate Eq. 4-37, again leaving two parameters to be determined. As is the case for the flux, one parameter characterizes the time when the flow evolves, $t_0 = r_w^{2/c}$, and one parameter

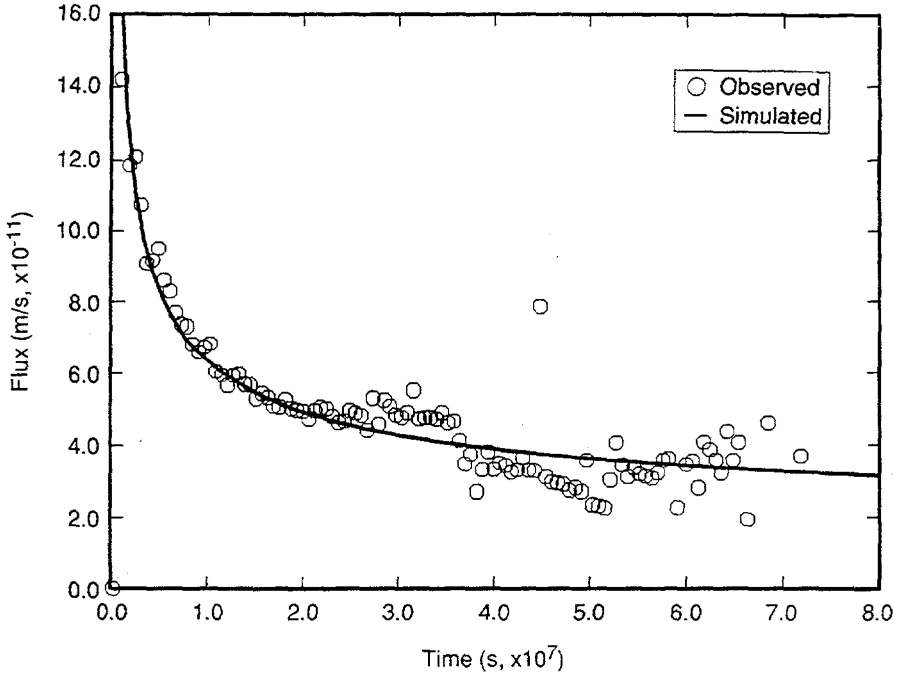

TRI-6119-281-0

Figure 4-27. Comparison of model fit to data for full flux history, hole DBT10.

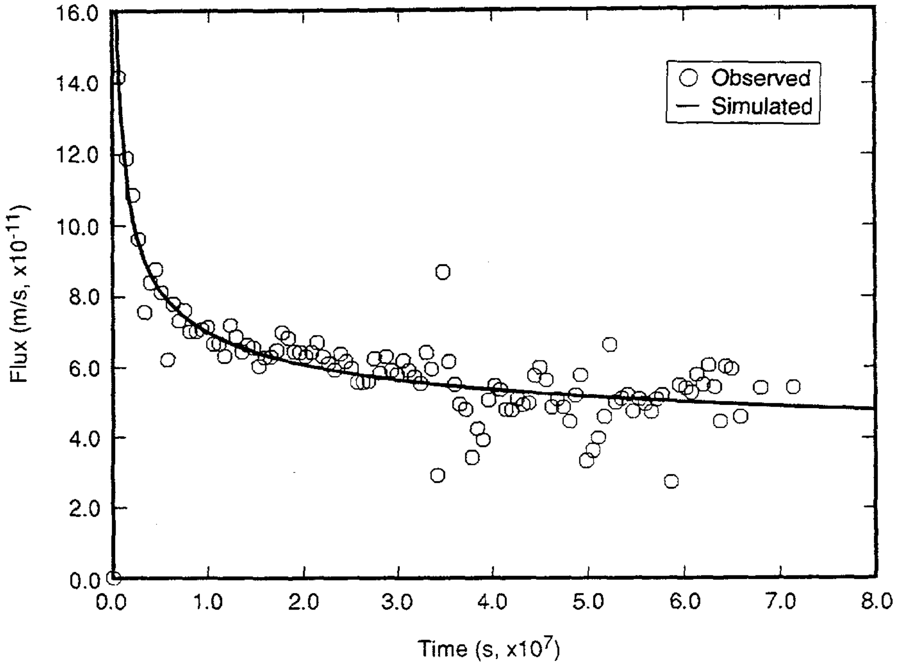

TRI-6119-282-0

Figure 4-28. Comparison of model fit to data for full flux history, hole DBT11.

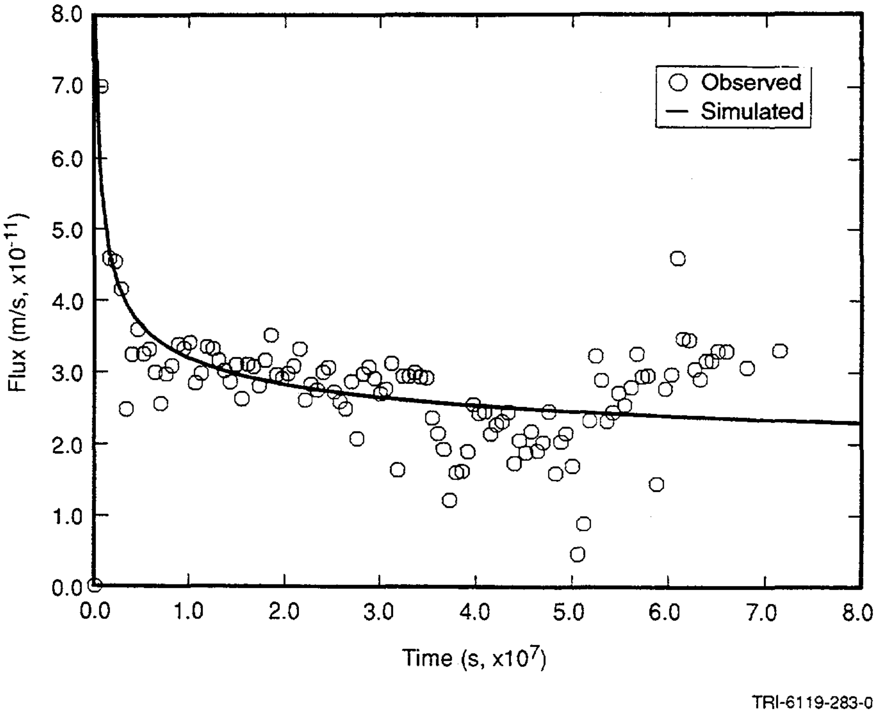

Figure 4-29. Comparison of model fit to data for full flux history, hole DBT12.

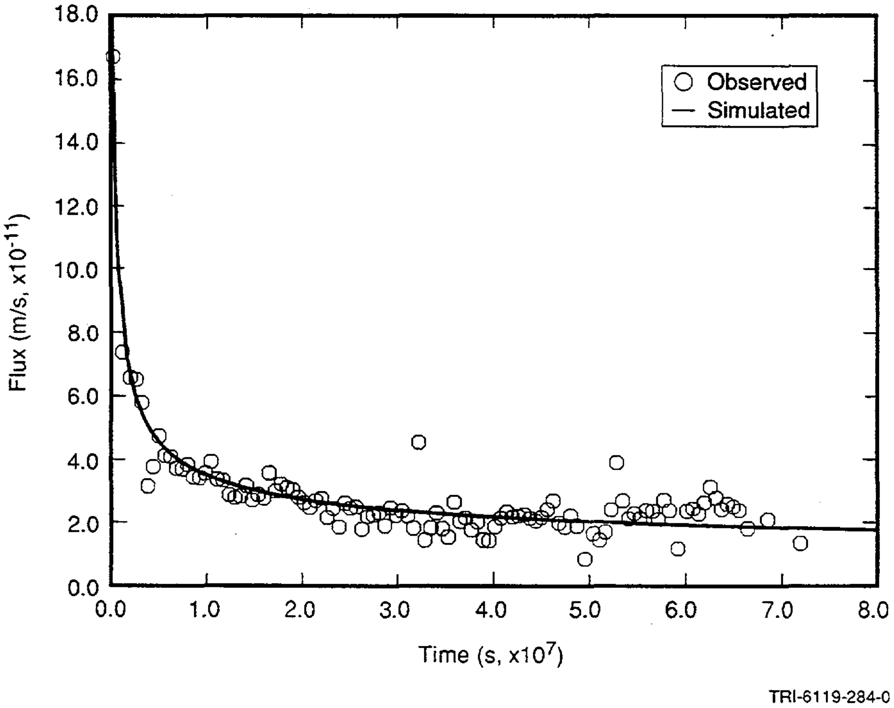

Figure 4-30. Comparison of model fit to data for full flux history, hole DBT13.

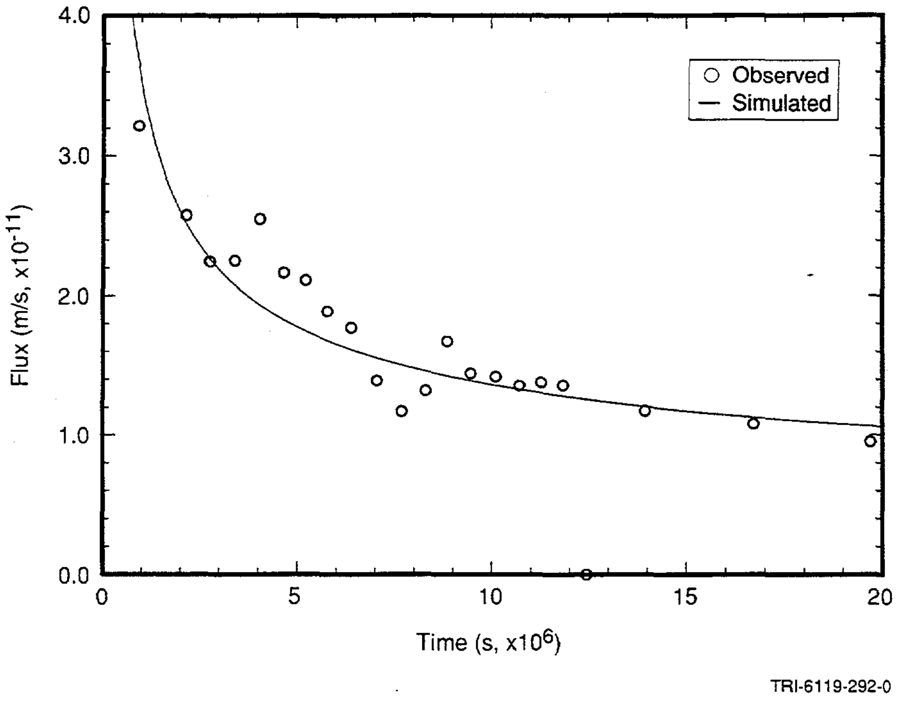

Figure 4-31. Comparison of model fit to data for flux history, hole L4B01.

Table 4-4. Parameters Derived from Fits to Flux through January 1990

Hole	Perm. x Press. kp_∞ (m^2Pa, x 10^{-15})	Permeability* k (m^2, x 10^{-21})	Diffusivity c (m^2/s, x 10^{-10})	Specific Capacitance* C_s (Pa^{-1} x 10^{-9})
DBT10	3.84 ± 0.24	0.380 ± 0.024	0.47 ± 0.078	3.870 ± 0.69
DBT11	14.92 ± 0.55	1.490 ± 0.055	35.09 ± 6.29	0.200 ± 0.037
DBT12	8.40 ± 0.94	0.840 ± 0.094	101.73 ± 65.33	0.039 ± 0.025
DBT13	2.29 ± 0.35	0.230 ± 0.035	0.59 ± 0.23	1.850 ± 0.77
L4B01	0.88 ± 0.56	0.088 ± 0.056	0.58 ± 0.91	0.730 ± 1.24
	—	—	—	—

* Assumes $p_\infty = 1.0 \times 10^7$ Pa, $\mu = 2.1 \times 10^{-3}$ Pa·s, $\rho = 1200$ kg/m^3.

characterizes the magnitude of the volume per unit area, $v_0 = kp_\infty r_w/\mu c = C_s p_\infty r_w$. With r_w and μ known, one may fit for the diffusivity, c, and the product of the specific capacitance and the initial pressure, $C_s p_\infty$. The integral in Eq. 4-37 was evaluated by Gauss quadrature using the SLATEC subroutine DGAUS8.

Fits were obtained for the entire monitored histories of holes DBT10, DBT11, DBT12, DBT13, and L4B01. The fits of Eq. 4-37 to data for cumulative volume are shown in Figures 4-32 through 4-36. The resulting parameters are summarized in Table 4-5. The fit determines c and $p_{\infty}C_s$; the specific capacitance is determined from the latter, assuming $p_{\infty} = 10^7$ Pa. The permeability is then determined using $k = c\mu\, C_s$, with $\mu = 2.1 \times 10^{-3}$ Pa·s. The diffusivity characterizes the rate of decay of the flux; consequently, it is sensitive to the evolution of the flow in time, which is quite variable from hole to hole. Correspondingly, the fits yielded a wide range of apparent diffusivities, on the order of 10^{-10} to 10^{-8} m^2/s. Similarly, the inferred specific capacitances range from 10^{-11} to 10^{-9} Pa^{-1}. The permeability is determined from the magnitude of the flow rate, which was observed to fall within a fairly narrow range. Thus, the fits yielded permeabilities typically in the range 10^{-22} to 10^{-21} m^2.

FITS BASED ON THE LATE-TIME FLUX HISTORIES

An attempt was also made to fit the late-time, asymptotic solution for the flux to the data. The disadvantage of this approach is that it discounts the early-time response, when the flow evolves relatively rapidly, and the data contain information more sensitive to the diffusivity. This limitation is manifested in the difficulty of obtaining a reliable value for the intercept. However, there are advantages to considering the late-time response, in addition to its simplicity. First, plots of the model output versus late-time flux give some visual indication of how far the idealized model can be taken, and where it begins to break down. A linear portion of the curve with positive slope is the region where the model may yield meaningful results. A departure from the linear trend at some point may indicate that phenomena not accounted for by the model, such as crack growth, started to influence the flow. Second, this method allows a local fit in those regions where it appears to apply; for example, data at very late time that become erratic can be excluded from the fit. Of course, this introduces considerable subjectivity into the fitting process, and the results should be viewed with this in mind.

Figures 4-37 through 4-42 show all data fitted to late-time flux for selected portions of the data. The resulting hydraulic properties are given in Table 4-7. Permeability values are more reliable than capacitance values; this fact is borne out by the relatively narrow range of permeability inferred, and the reasonable agreement with results from the more complete fits shown in Tables 4-5 and 4-6.

Table 4-5. Parameters Derived from Fits to Cumulative Volume

Hole	Diffusivity c (m^2/s)	Pressure x Specific Capacitance $p_\infty C_s$	Specific Capacitance* C_s (Pa^{-1})	Permeability* k (m^2)
DBT10	3.11×10^{-10}	1.03×10^{-2}	1.03×10^{-9}	6.72×10^{-22}
DBT11	5.77×10^{-9}	1.33×10^{-3}	1.33×10^{-10}	1.610×10^{-21}
DBT12	1.41×10^{-8}	2.88×10^{-4}	2.88×10^{-11}	8.53×10^{-22}
DBT13	1.5×10^{-10}	9.56×10^{-3}	9.56×10^{-10}	3.02×10^{-22}
L4B01	4.4×10^{-9}	1.85×10^{-3}	1.85×10^{-10}	1.71×10^{-22}

* Assumes $p_\infty = 1.0 \times 10^{7}$ Pa, $\mu = 2.1 \times 10^{3}$ Pa·s, $\rho = 1200$ kg/m^3.

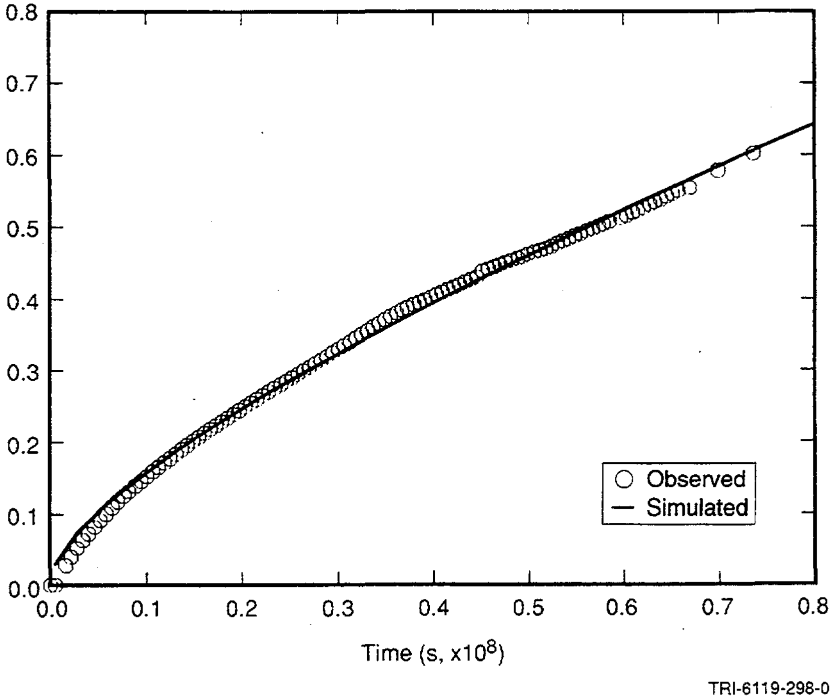

Figure 4-32. Comparison of model fit to data for cumulative volume history, hole DBT10.

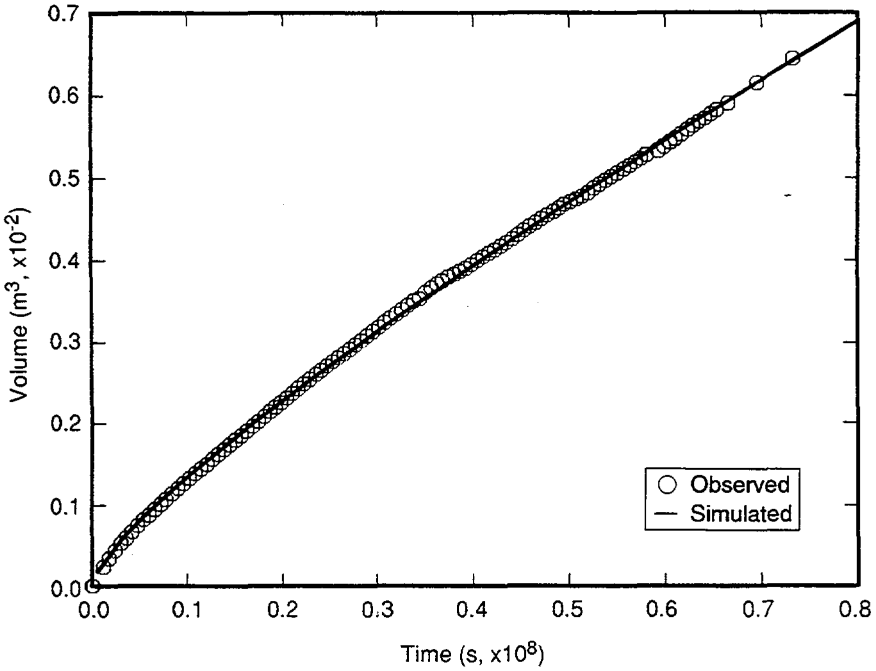

TRI-6119-299-0

Figure 4-33. Comparison of model fit to data for cumulative volume history, hole DBT11.

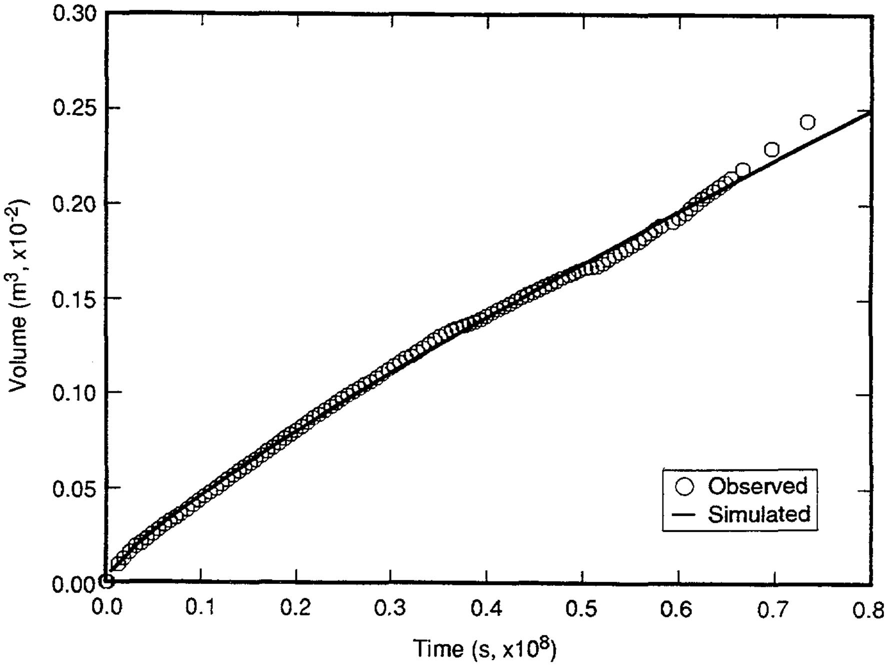

TRI-6119-300-0

Figure 4-34. Comparison of model fit to data for cumulative volume history, hole DBT12.

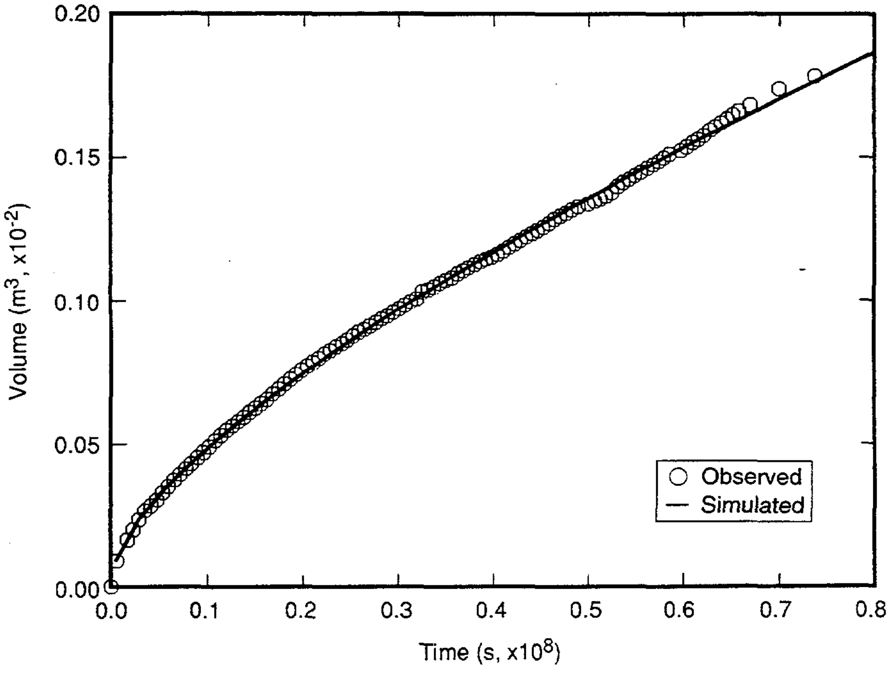

TRI-6119-301-0

Figure 4-35. Comparison of model fit to data for cumulative volume history, hole DBT13.

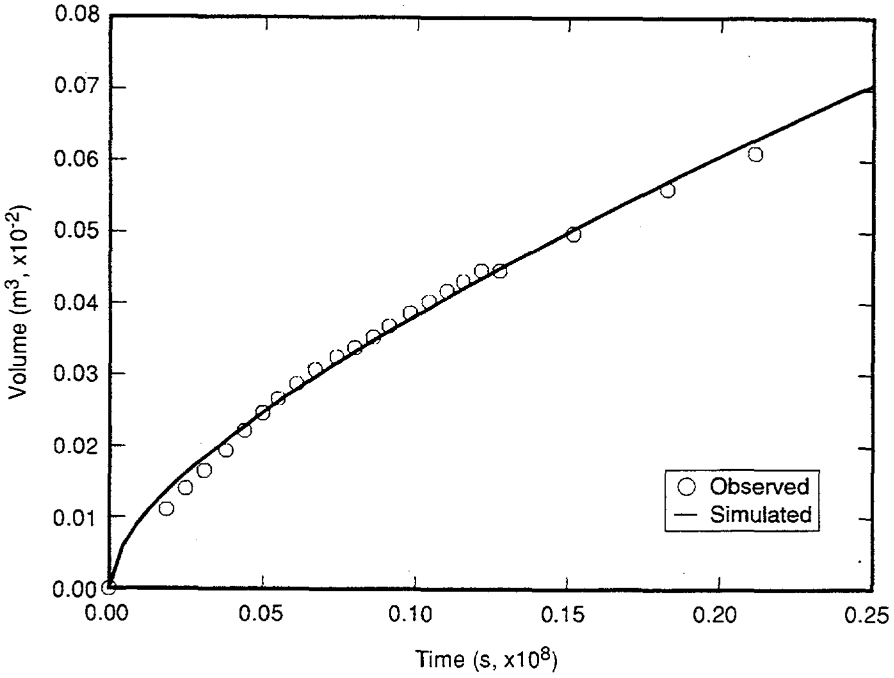

TRI-6119-304-0

Figure 4-36. Comparison of model fit to data for cumulative volume history, hole L4B01.

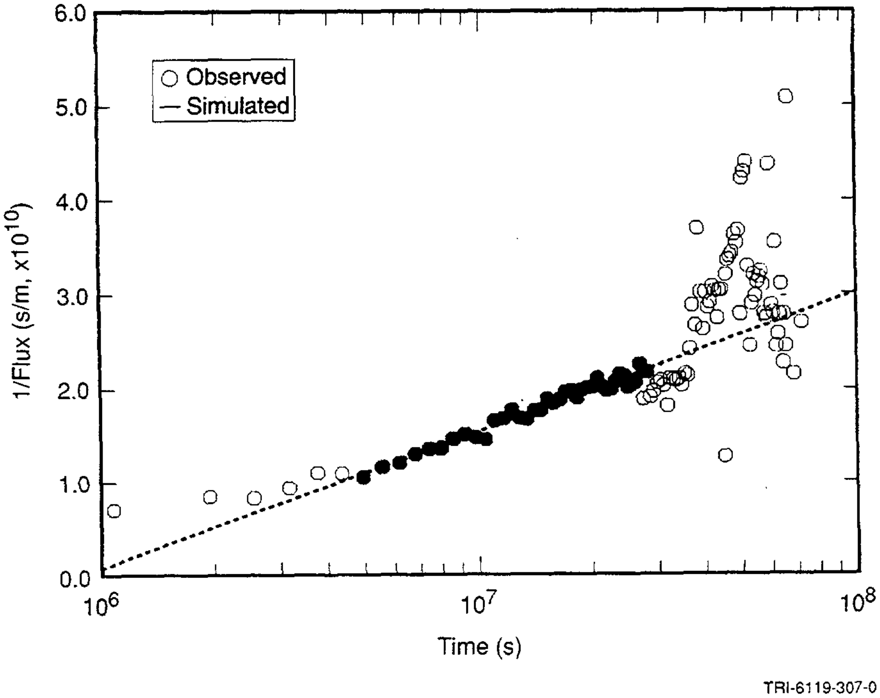

Figure 4-37. Comparison of model fit to data for late-time flux, hole DBT10. Points included in linear regression are shaded.

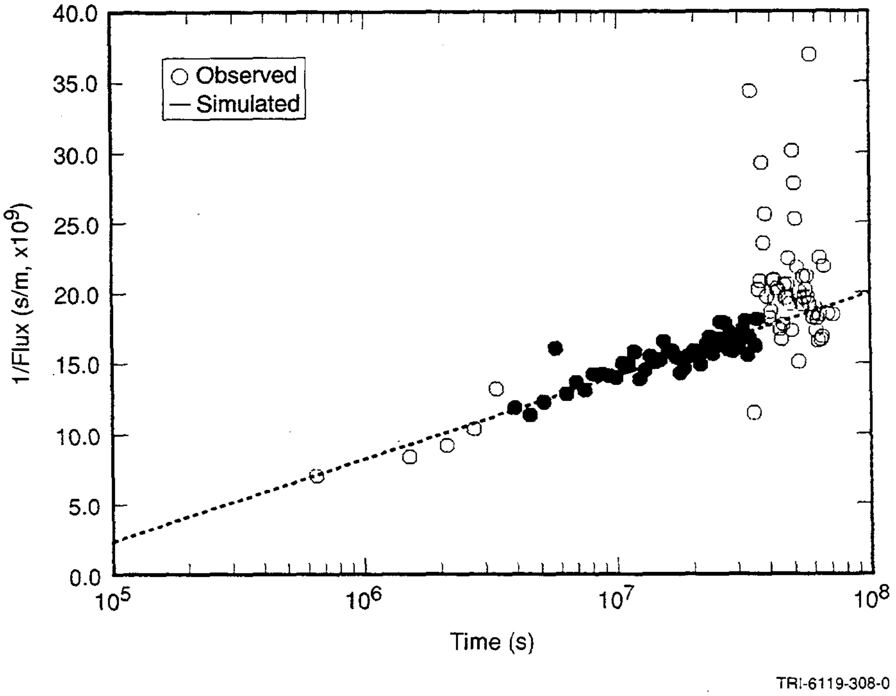

Figure 4-38. Comparison of model fit to data for late-time flux, hole DBT11. Points included in linear regression are shaded.

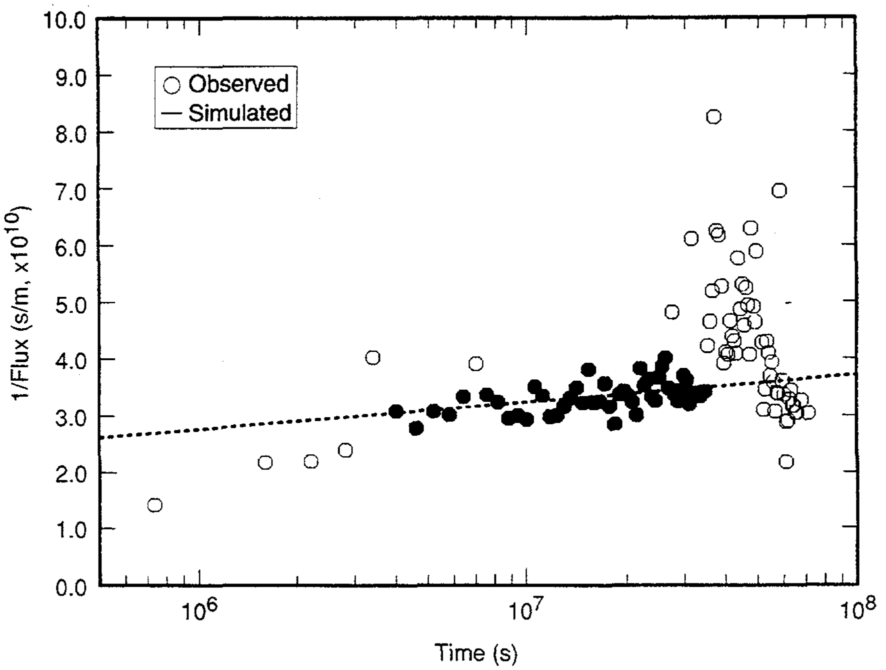

TRI-6119-309-0

Figure 4-39. Comparison of model fit to data for late-time flux, hole DBT12. Points included in linear regression are shaded.

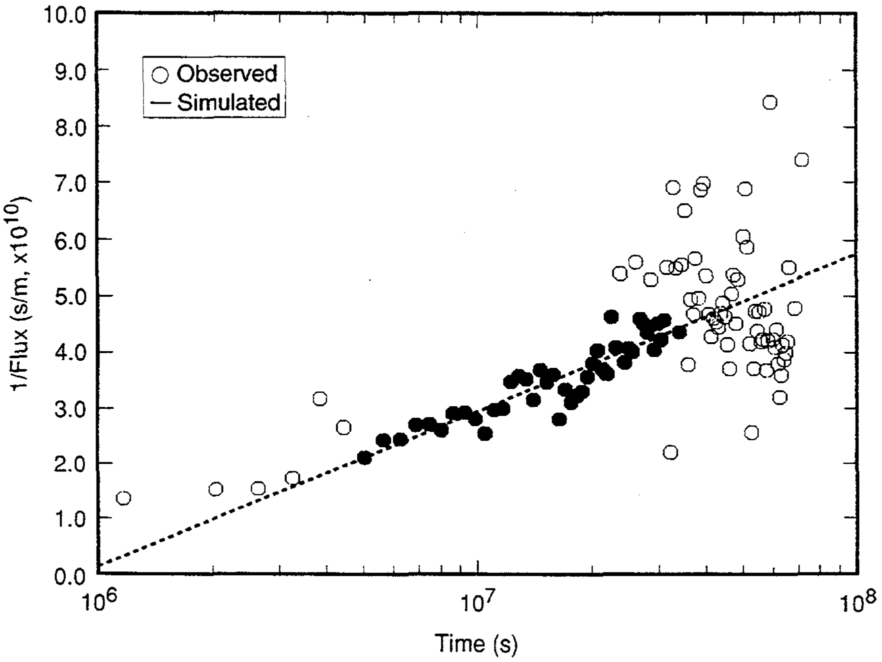

TRI-6119-310-0

Figure 4-40. Comparison of model fit to data for late-time flux, hole DBT13. Points included in linear regression are shaded.

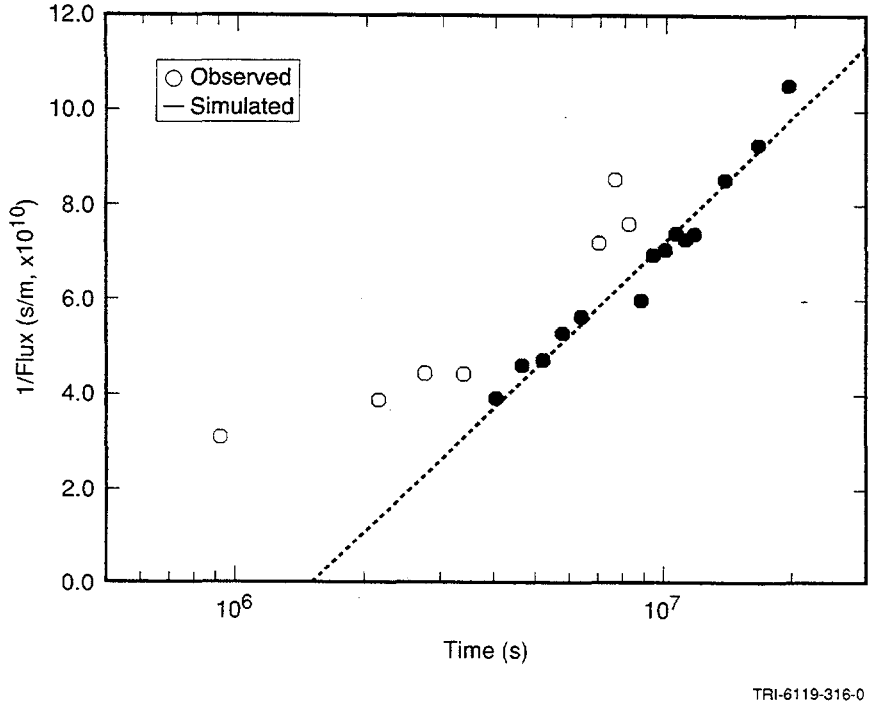

Figure 4-41. Comparison of model fit to data for late-time flux, hole L4B01. Points included in linear regression are shaded.

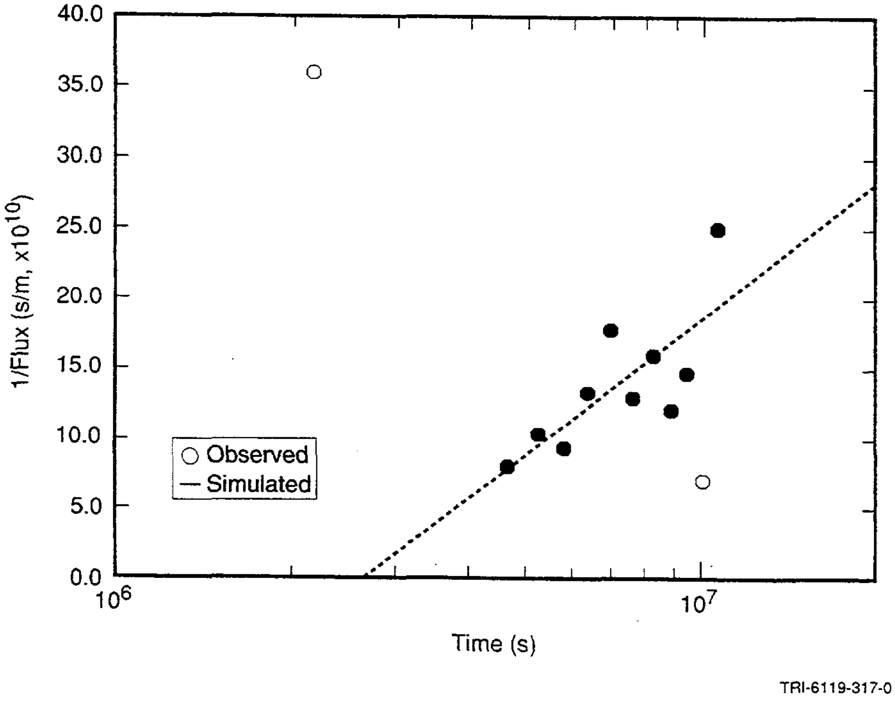

Figure 4-42. Comparison of model fit to data for late-time flux, hole L4X01. Points included in linear regression are shaded.

Table 4-6. Parameters Derived from Fits to Late-Time Flux

Hole	Perm. x Press. kp_∞ (m^2Pa)	Permeability* k (m^2)	Diffusivity c (m^2/s)	Specific Capacitance* C_s (Pa^{-1})
DBT10	8.33×10^{-15}	8.33×10^{-22}	2.28×10^{-9}	1.74×10^{-10}
DBT11	2.07×10^{-14}	2.07×10^{-21}	5.08×10^{-8}	1.95×10^{-11}
DBT12	2.6×10^{-14}	2.6×10^{-21}	1.45×10^{-7}	8.53×10^{-7}
DBT13	4.38×10^{-15}	4.38×10^{-22}	2.28×10^{-9}	9.14×10^{-11}
L4B01	1.4×10^{-15}	1.4×10^{-22}	1.36×10^{-9}	4.92×10^{-11}
L4X01	3.44×10^{-15}	3.44×10^{-22}	6.26×10^{-8}	2.6×10^{-12}

* Assumes $p_\infty = 1.0 \times 10^7$ Pa, $\mu = 2.1 \times 10^{-3}$ Pa·s, $\rho = 1200$ kg/m^3.

The permeabilities inferred here are on the order of 10^{-22} to 10^{-21} m^2. Most are within a factor of two of the values obtained by fitting the entire flux or cumulative volume histories.

The diffusivities and specific capacitances inferred by this method must be regarded as questionable. The latter fall in a range of order 10^{-12} to 10^{-10} Pa^{-1}, with DBT12 giving $C_s = 8.5 \times 10^{-16}$ Pa^{-1}. The latter value is clearly absurd, as it implies compressibilities many orders of magnitude less than can be rationalized for the salt and brine. The extremely small specific capacitance inferred in this case results from the very slow decay rate observed at late time.

Notably, the specific capacitances inferred from these fits are, in many cases, about an order of magnitude smaller than those inferred from the full fits. This occurs because the full data for many holes exhibit fluxes that drop off very slowly at very late time. Thus, the fits to the full data sets arrive at a relatively large value of C_s in order that the characteristic time for the decay of the flux be large. In contrast, because the fits of the asymptotic expression (Eq. 4-44) typically exclude the very late time data, when the linearity of $|\mathbf{q}|^{-1}$ versus ln t appears to break down, intermediate times (typically centered around $\approx 10^7$ s) are given more weight. During the period when the asymptotic expression appears to represent the data, the decay of the flux occurs at a somewhat higher rate than that inferred for the full histories, and this is reflected in smaller inferred values of C_S.

CHOICE OF PARAMETERS FOR THE FITS

The regressions reported here are two-parameter fits. For example, the flux is fit for a magnitude, $\mathbf{q}_0 = kp_\infty/\mu r_w$, and a characteristic decay time, $t_0 = r_w^2/c$. The approach followed in the foregoing was to treat the borehole radius and the brine viscosity as known, because they can be determined with good accuracy by direct, independent measurements. The initial brine pressure was also treated as known, with the constant value $p_\infty = 10$ MPa assumed. This leaves the permeability, k, and the diffusivity, c, as unknowns determined by the fits. The specific capacitance, $C_s = k/\mu c$, can then be computed as well.

An alternative scheme that can be applied in a system whose mechanical properties are well characterized is to consider the specific capacitance known. This requires a model for the relationship between specific capacitance and various material properties (e.g., Eq. 4-16), as well as independent laboratory measurements of the rock and fluid compressibilities. In this case, the two remaining unknowns determined by the fits are the permeability and the initial pressure, p_∞. This scheme is attractive because p_∞ is indeed unknown, can be expected to exhibit some variability, and can be determined only by *in situ* measurements. However, its success rests on the assumption that the storage mechanisms are well understood, properly represented by the model adopted, and characterized accurately by the independent measurements. That this is not the case for the salt is suggested by the following argument. The field data for borehole seepage indicate a relatively long time scale that characterizes the decay of the flux, typically 100 days. The long time scale implies that the diffusivity is small, which, for fixed specific capacitance, implies that the permeability is small. In order to match the magnitude of the flux given a small permeability, the inferred formation pressure must be unrealistically large.

A sample calculation illustrates this point. Suppose that t_0 is 10^7 s (~116 days); assume that $C_s = 1.0 \times 10^{-11}$ Pa^{-1}, which is consistent with various estimates based on the elastic properties of the salt and brine (Freeze and Cherry, 1979; Nowak and McTigue, 1987). Then, with $r_w = 0.05$ m and $\mu = 0.0021$ Pa$\cdot$s, the inferred permeability is $k \sim r_w^2 \mu C_s/t_0 \cong 5 \times 10^{-24} \mathrm{m}^2$. That gives (with $\mathbf{q}_0 \cong 10^{-10}$ m/s)

$p_\infty \sim \mathbf{q}_0 \mu\, r_w/k \cong 2 \times 10^9$ Pa, which is clearly absurd (the lithostatic stress is two orders of magnitude smaller). Thus, as discussed in the foregoing paragraph, this scheme leads to implausible estimates of both the permeability and the formation pressure.

The fitting scheme adopted by McTigue (1993), which concerns the formation pressure as known and the permeability and capacitance as unknowns, in some sense acknowledges that the mechanisms affecting capacity or storage in the salt may not be understood fully. This uncertainty is then submerged in the estimation of the specific capacitance, which should be viewed as an "effective" or "apparent" property of the salt. It is important to recognize, however, that the large values of specific capacitance inferred from the fits (e.g., Table 4-4) are not easily reconciled with the classical models of an elastic, porous skeleton and compressible fluid (e.g., Eq. 4-16). Such models predict a specific capacitance of the order of $C_s \sim 10^{-11}$ Pa^{-1}, while the fits yielded many estimates on the order of 10^{-10} to 10^{-8} Pa^{-1}.

VALIDITY OF THE RADIAL FLOW APPROXIMATION

After a sufficiently long time, the measured flow to a borehole becomes sensitive to the finite length of the hole. A simple validity check for the one-dimensional, radial flow assumption is to compute the diffusion length for the duration of the test, and compare this to the length of the hole. The diffusion length is defined by $L_d = \sqrt{ct}$ and represents the characteristic radial distance to which the pressure relaxation has propagated after time t. If $L_d/L << 1$, the zone of relaxed pressure near the borehole is still highly elongate, and the one-dimensional model is appropriate. The data for the Room D holes cover a period up to about $t = 7.5 \times 10^7$ s (868 days), while those from Room L4 cover a period up to about $t = 2.5 \times 10^7$ s (289 days). The corresponding diffusion lengths for various diffusivity values are shown in Table 4-7. Note that criterion $L_d/L << 1$ is satisfied for the holes under consideration only if c is 10^{-8} $\mathrm{m^2/s}$ or less. This condition holds for most of the fits for most of the holes.

Table 4-7. Diffusion Length Scales for Various Diffusivities

	Diffusion Length $L_d = \sqrt{ct}$(m)	
Diffusivity (c, m^2/s)	$t = 2.5 \times 10^7$s	$t = 7.5 \times 10^7$s
10^{-10}	0.050	0.087
10^{-9}	0.158	0.274
10^{-8}	0.500	0.866
10^{-7}	1.580	2.740
10^{-6}	5.000	8.660

The effect of the third dimension (e.g., a finite-length hole) is typically to weaken the flow relative to the radial case. This is a consequence of geometric spreading of the diffusive front. For example, while the radial flux to a very long hole decays according to $2/\ln(4t_* / C_s^2)$ at late time, the flux to a spherical cavity of radius r_w decays (over its entire history) according to:

$$\mathbf{q}_* = 1 + (\pi t_*)^{-1/2} \tag{4-51}$$

where the non-dimensionalizations are the same as those that were introduced in the cylindrical case. Thus, the effect of the third dimension is to allow the flux to decay more rapidly and to approach a non-zero, steady-state value. If a particular data set is influenced by such geometric effects, but is fit by the radial flow model, the fit will tend toward small values of the diffusivity so that the flux does not decay over a long period of time.

Additional multidimensional effects are introduced by the presence of the room from which a borehole is drilled. First, there is seepage toward the mined faces of the room. Second, the initial mean stress state penetrated by a borehole is influenced by the room; the mean stress is reduced near mined faces, and the initial, undrained brine pressure is consequently reduced as well. Work by Gelbard (1992) considers both seepage toward the room floor and a depth-varying initial brine pressure. Both effects tend to weaken the brine inflow to a borehole, and neglect of these effects results in underestimates of the permeability. Finally, creep of the salt results in a continued evolution of the mean stress field in the neighborhood of mined cavities, and this evolution is coupled to the brine flow as well.

COMPARISON OF FITS OVER VARIOUS TIME INTERVALS

This section provides a comparison of parameters derived from fits of both the flux and cumulative volume models to the observed data over various time intervals to provide a measure of the sensitivity of the results to various possible fitting schemes. Only data from DBT10 are treated; this is one of the archetypical data sets, insofar as the response of the hole was quite smooth, and the rate of decay of the flux decreased monotonically. Results are summarized in Table 4-8. The variation in the inferred material properties reflects comments made previously: The permeability is reasonably well constrained; all values fall within about a factor of two of $k \cong 10^{-21}$ m^2, whether from a fit to the flux or the volume, and whether the data span 830, 470, or 230 days. The inferred diffusivity, however, is one to two orders of magnitude larger for the cumulative-volume fits, and it increases significantly for fits to the shorter history. The fits to the flux are more sensitive to the early-time response, so that the inclusion of more data has relatively little influence, here decreasing the inferred diffusivity by only a factor of two. In contrast, the fits to the volume are more sensitive to the later response, and the continually decreasing apparent diffusivity with longer data sets reflects the fact that the observed flow decayed more slowly than predicted by the idealized model at late time. That is, the characteristic time for the decay of the flux appears to be increasing with time. Therefore, a fit to a longer data set arrives at a smaller value of the diffusivity, c.

These results emphasize that the permeability is fairly well constrained simply by the magnitude of the flows observed, while the diffusivity is more difficult to bound. Determination of the diffusivity depends on the details of the flow history, which was erratic for some holes. Furthermore, the flow histories are more likely to exhibit effects not accounted for by the idealized model for uniform, radial flow.

Table 4-8. Parameters for DBT10 by Various Fitting Schemes

Basis of Fit		Diffusivity c (m^2/s)	Permeability* k (m^2,)	Specific Capacitance* C_s (Pa^{-1})
Data type	Time period (d)			
flux	830	5.4×10^{-11}	4.1×10^{-22}	3.6×10^{-9}
flux	470	1.1×10^{-10}	5.2×10^{-22}	2.3×10^{-9}
flux	230	1.1×10^{-10}	5.4×10^{-22}	2.3×10^{-9}
cum. vol.	830	3.1×10^{-10}	6.7×10^{-22}	1.0×10^{-9}
cum. vol.	470	1.7×10^{-9}	1.1×10^{-21}	3.1×10^{-10}
cum. vol.	230	8.2×10^{-9}	1.7×10^{-21}	9.7×10^{-11}

* Assumes $p_\infty = 1.0 \times 10^{7}$ Pa, $\mu = 2.1 \times 10^{-3}$ Pa·s, $\rho = 1200$ kg/m^3.

COMPARISON OF FITS BY VARIOUS METHODS

Figures 4-43 and 4-44 provide a graphical comparison of the variation in the parameters inferred by the three fitting procedures summarized in Tables 4-5, 4-6, and 4-7. In each case, the parameters inferred from fits based on the first method named in the figure legends are plotted as “Fit 1,” and those from the second method are plotted as “Fit 2.” Identical results from each method, of course, plot on a line with unit slope. Departures from this line indicate the discrepancies among methods. As noted previously, the fits for permeability generally result in reasonably consistent results, and no systematic variations are apparent in Figure 4-43. The inferred capacitances shown in Figure 4-44 exhibit larger differences, depending on the fitting method. The plot shows that the fits based on the late-time-flux approximation tend to result in much smaller estimates of the capacitance.

4.3.5 Problem Areas

In McTigue's (1993) work, formation pressure was assumed to be 10 MPa in order to estimate the permeability. The error in the estimates of the permeability is proportional to the error in p_∞. Various independent estimates of p_∞ typically fall in the range of 0.5 to 12 MPa (Beauheim et al., 1991). In general, it appears that pressures of about 10 MPa are found for measurements taken in the far field (i.e., at distances of the order of 10 m or greater away from facility excavations). Measurements in salt within a few meters of mined faces typically yield smaller estimates of the pore pressure. Beauheim et al. (1991) inferred formation pressures from pressure-pulse tests from Room C2 in a setting similar to that of Room D. Pressures in three sections within the first few meters below the floor were inferred to be 0.5, 3.2, and 4.1 MPa, suggesting that stress relief due to the presence of the room caused a significant reduction in pore pressure.

The parameter estimates reported in McTigue (1993) for the small-scale brine-inflow experiments yield values for the product of the permeability and the initial pressure. The permeability has been separated only by making the additional assumption that $p_\infty = 10$ MPa. This choice may be appropriate for salt undisturbed by excavation effects, but is likely too large for the salt penetrated by the boreholes under consideration. If a better estimate of p_∞ is available, the estimates of k and C_s reported here can be rescaled accordingly. As noted previously, the adjustment is proportional to the changes in the assumed initial pressure. For example, given $p_\infty = 5$ MPa, the estimated permeabilities must be multiplied by a factor of two, and the estimated specific capacitances must also be multiplied by two.

The data reduction in McTigue (1993) assumed a mass density for the brine of 1.2 x 10^3 kg/m^3. Recent direct measurements on samples taken from the study holes indicated 1.224 to 1.240 x 10^3 kg/m^3 (Howarth et al., 1991). Thus, the volume, flux, and permeability estimates are too large by 2 to 3%. Diffusivity is unaffected, but specific capacitance, calculated from $C_s = k/\mu c$, is proportionately too large.

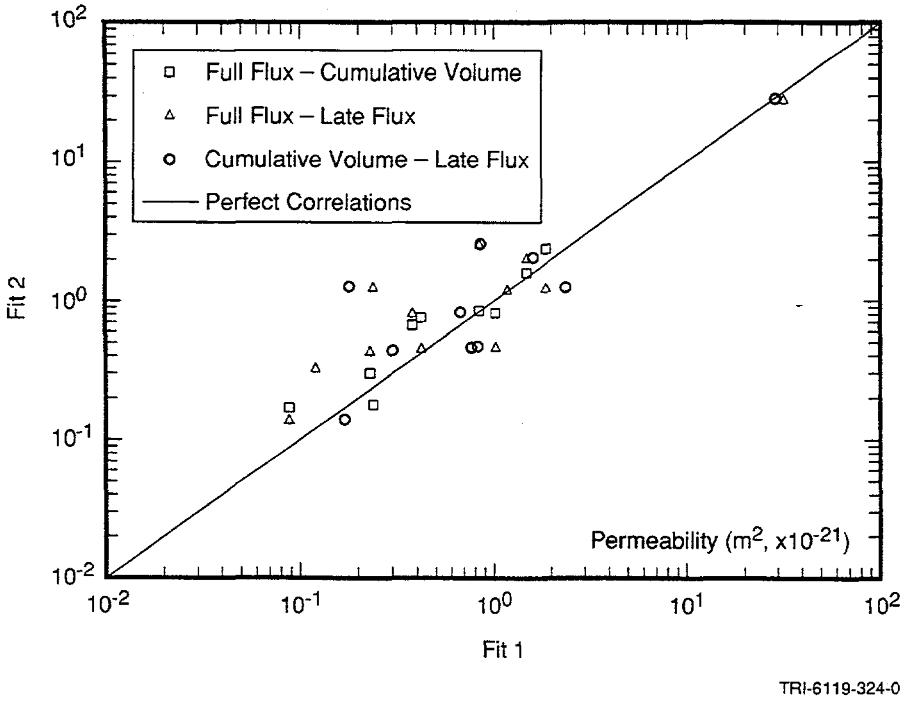

Figure 4-43. Comparison of permeability values determined by various methods. Perfect correlations lie on the solid line.

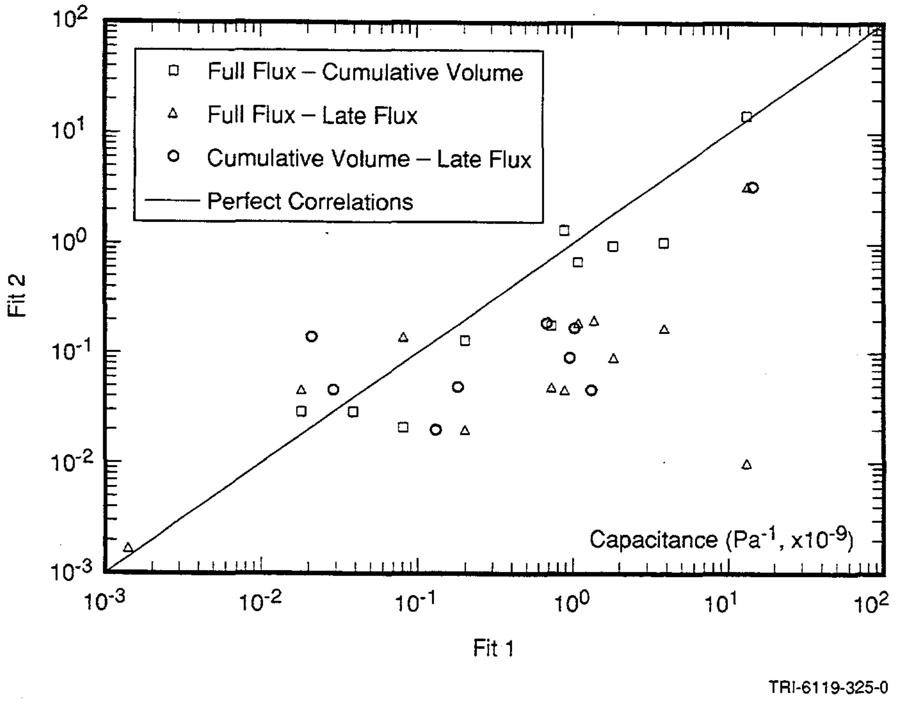

Figure 4-44. Comparison of capacitance values determined by various methods. Perfect correlations lie on the solid line line.

The estimates of the expected specific capacitance for an elastic matrix and fluid inferred in McTigue were quite large in comparison to values expected on the basis of classical models for elastic constituents. Eleven of 15 estimates of C_s fall in the range of 10^{-10} to 10^{-8} Pa^{-1}. Estimates based on the elastic moduli of the salt and brine are of the order of 10^{-11} Pa^{-1} (Nowak et al., 1988; Beauheim et al., 1991). Parameters that enter into such estimates are recorded in Table 4-10. Use of the moduli shown in Table 4-10 and ϕ = 0.01 in Eq. 4-16 yields $C_s \sim 0.8 \times 10^{-11}\,\mathrm{Pa}^{-1}$. The calculation is rather insensitive to the estimate of the connected porosity, ϕ; for example, the assumption of ϕ = 0.001 and the same moduli results in $C_s \sim 0.6 \times 10^{-11}\,\mathrm{Pa}^{-1}$.

Beauheim et al. (1991) report a more detailed compilation of ranges of properties by lithology. They compute weighted averages of the storage based on the fractions of the specific lithologies present in a given test interval. The resulting specific capacitances fall in the range (0.8 - 1.3) x 10^{-11} Pa^{-1}, consistent with the calculation based on the values given in Table 4-9.

Table 4-9. Elastic Properties of Salt and Brine

Parameter	Value	Units	Reference
Drained Bulk Modulus, K_m	20.7	GPa	Krieg (1984)
Poisson Ratio, υ	0.25	—	Krieg (1984)
Solid Bulk Modulus, K_s	23.5	GPa	Sumino and Anderson (1984)
Fluid Bulk Modulus, K_f	4.0	GPa	*
Porosity, ϕ	0.004 - 0.01	—	Stein and Kimball (1992)

*Determined from acoustic measurements.

The specific capacitances inferred in McTigue should be regarded as effective or apparent values. These fits yield large estimates of the specific capacitance that are difficult to reconcile with the classic model of storage due to elastic compressibility of the porous skeleton and the fluid. Recall that the large estimates of specific capacitance are a consequence of the relatively large time scale that characterizes the observed decay of the flux. This long time scale possibly arises from one or more mechanisms other than diffusive relaxation of pore pressure. Deformation of the salt in the neighborhood of excavations is one obvious candidate source for other time scales that may influence the brine flow (McTigue et al., 1989). It is known, for example, that the salt is subject to rate-dependent creep, crack growth, and other processes that may have a large influence on brine seepage. These processes can lead to various conditions, including time-dependent relaxation of the mean total stress σ, inelastic dilation of the salt, large permeability changes, and imbibition of air and consequent multiphase flow. Such coupling may introduce time scales longer than the expected diffusive time scale, which may be reflected in the data.

In this context, it is also important to note that the data collected from January 1990 through June 1991, which were not treated in McTigue (1993) but are summarized in Finley et al. (1992), indicate fluxes that either level off or increase slowly for most of the holes. This response is clearly not in accord with the idealized model used in this study to interpret the earlier data. The explanation may lie with the continued evolution of the state of stress and the microstructure of the salt surrounding the excavations.

4.4 Comparison and Summary of Project Teams' Interpretations

In comparing the parameters estimated by the three teams interpreting the small-scale brine-inflow experiments, allowances must be made for slight differences in the input parameters used by the three teams and the effects of those differences on the interpreted parameter values. The three input parameters for which the teams used different input values are initial formation pore pressure, brine density, and brine viscosity. The RIVM and SNL teams used an initial formation pore pressure estimate of 10.0 MPa while the EdM team used a value of about 11.2 MPa. Consequently, increasing the permeability values interpreted by the EdM team by 12% provides for better comparison to the values interpreted by the RIVM and SNL teams.

For brine density, the RIVM and EdM teams used a value of 1220 kg/m^3 while the SNL team used a value of 1200 kg/m^3. Based on measurements reported by Deal et al. (1987), the higher value is more representative of Salado brines. Therefore, the

SNL permeability and specific capacitance estimates should be decreased by 2% before being compared to the RIVM or EdM estimates.

With respect to brine viscosity, the RIVM team used a value of 1.6×10^{-3} Pa·s while the SNL team used a value of 2.1×10^{-3} Pa·s. The latter value is based on direct measurements and is, therefore, believed to be more accurate than the value used by the RIVM team, which was based on literature data. To be directly comparable to the SNL estimates, therefore, the RIVM estimates of permeability must be increased by 31%. The EdM simulations were done in terms of hydraulic conductivity rather than permeability and consequently did not involve an explicit value for brine viscosity. The EdM hydraulic conductivity values have been converted to permeabilities for this report using Eq. 4-9 and a brine viscosity of $2.1 \times 10^{-3}\,\mathrm{Pa \cdot s}$. All of the permeability and capacitance values discussed in the remainder of this section have been compensated for differences in pore pressure, brine density, and brine viscosity, as appropriate.

A major difference between the RIVM and EdM interpretations and the SNL interpretations is the treatment of the strata tested. The RIVM and EdM teams distinguished between pure and impure halite in estimating values for permeability. They assumed that pure halite would have a lower permeability than impure halite and sought single values for each that, when combined with the different thicknesses of pure and impure halite in the different test holes, would allow replication of the entire set of experimental results. The SNL team treated the strata penetrated by each hole as homogeneous and sought values for hydraulic properties, different at each hole, that would best match the observed data. Thus, the RIVM and EdM teams determined values for the permeability of pure and impure halite that provided the best overall match to the brine-inflow data in the aggregate, but not to the brine-inflow data from any individual hole, while the SNL team determined average permeability values for each borehole.

The RIVM team obtained good fits to data from all four of the DBT10 to DBT13 small-scale brine-inflow holes using permeability values of 5.25×10^{-22} and 5.25×10^{-21} m^2 for pure and impure halite, respectively. The EdM team used values of 6.6×10^{-23} and 3.5×10^{-21} m^2 for pure and impure halite, respectively, to fit the data from three of the four holes.

To compare the RIVM and EdM results to the SNL results, the pure and impure halite permeabilities were weighted according to each individual borehole's stratigraphy to determine an average permeability for each borehole. These average permeabilities are shown in Table 4-10, along with the average permeabilities calculated by the SNL team using different parts of the data. The teams agree about the average permeability at each of the boreholes within a factor of five. The total range of inferred permeability values spans only an order of magnitude, from 2.3×10^{-22} to 2.6×10^{-21} m^2. These values are slightly lower than the range of 10^{-21} to 10^{-20} m^2 used by Nowak et al. (1988) to predict brine inflows to WIPP disposal rooms.

Table 4-10. Comparison of Permeabilities Calculated by Different Teams

Borehole	Calculated Permeabilities*, m^2				
	RIVM	EdM	SNL		
			Full Flux	Cum. Vol.	Late-Time
DBT10	1.8×10^{-21}	9.9×10^{-22}	3.7×10^{-22}	6.6×10^{-22}	8.2×10^{-22}
DBT11	2.1×10^{-21}	1.2×10^{-21}	1.5×10^{-21}	1.6×10^{-21}	2.0×10^{-21}
DBT12	1.5×10^{-21}	--	8.3×10^{-22}	8.4×10^{-22}	2.6×10^{-21}
DBT13	8.5×10^{-22}	3.0×10^{-22}	2.3×10^{-22}	3.0×10^{-22}	4.3×10^{-22}

* Assumes $p_\infty = 1.0 \times 10^7$ Pa, $\mu = 2.1 \times 10^{-3}$ Pa·s, $\rho = 1200$ kg/m^3.

Interpretations by the RIVM and EdM teams were constrained by their determinations of reasonable values for specific capacitance, while the interpretations by the SNL team treated specific capacitance as a free parameter to be fitted. The RIVM and EdM teams used values of 3.0×10^{-11} and 6.7×10^{-11} Pa^{-1}, respectively, for specific capacitance in their simulations. Table 4-11 shows a comparison of these values to the different values obtained by the SNL team using different fitting approaches. With a few exceptions, the SNL values tend to be one to two orders of magnitude higher than specific capacitances calculated on the basis of the elastic moduli of the rock. As discussed in Section 4.3.5, these apparently high specific capacitances may reflect geomechanical effects that have not been considered directly in the modeling done by the different teams.

Table 4-11. Comparison of Specific Capacitances Calculated by Different Teams

Borehole	Specific Capacitance, Pa^{-1}				
	RIVM	EdM	SNL		
			Full Flux	Cum. Vol.	Late-Time
DBT10	3.0×10^{-11}	6.7×10^{-11}	3.8×10^{-9}	1.0×10^{-9}	1.7×10^{-10}
DBT11	3.0×10^{-11}	6.7×10^{-11}	2.0×10^{-10}	1.3×10^{-10}	1.9×10^{-11}
DBT12	3.0×10^{-11}	6.7×10^{-11}	3.8×10^{-11}	2.8×10^{-11}	8.4×10^{-16}
DBT13	3.0×10^{-11}	6.7×10^{-11}	1.8×10^{-9}	9.4×10^{-10}	9.0×10^{-11}

None of the teams attempted to model the late-time data from the brine-inflow experiments that showed increasing rates of brine flow (Figure 3-2). For brine-inflow rates to increase with time, either the permeability around the borehole must increase, or the driving pressure differential must increase, or both. Increasing permeability is the most likely explanation for the increased inflow. Permeability could increase as halite creeps towards the overlying room. Existing fractures may dilate, new fractures may form, and bedding planes may separate as the salt creeps. Increasing permeability in any of these ways would, in effect, allow a borehole to draw brine from a larger volume of rock. Continued evaluation of the rate of change of brine inflow may provide information about phenomena causing the permeability increase. If the increase in permeability occurred as a single discrete event, the brine inflow should increase abruptly, but then decay in a manner similar to that observed over the first 800+ days of the experiments. However, if the increase in permeability were a gradual, continuing process, the inflow rate could increase continually, or might decay more slowly than would be expected if the permeability were constant.

Simulation of creep-induced permeability changes and the resulting changes in brine-inflow rates would require coupling between a geomechanical model of salt behavior around the WIPP repository and a hydrological flow code. Such a study is eyond the scope of the INTRAVAL teams' efforts, but should be considered by SNL.

This page intentionally left blank.

5. SUMMARY

5.1 Status of Validation Issues

The goal of this test case was to evaluate the use of Darcy's law to describe brine flow through halite. In a Darcy-flow regime, pressure and flow behavior are largely governed by the parameters permeability and specific capacitance. The general approach taken to evaluate the applicability of Darcy's law was, therefore, to try to obtain values of permeability and specific capacitance that would be: (1) consistent with other available data; and (2) able to provide reasonable simulations of *all* of the brine-inflow experiments performed in the Salado Formation. It was not to be expected that single values of permeability and specific capacitance would lead to exact replication of all of the experiments because of factors such as geologic heterogeneity and excavation effects. However, if all of the experimental data could be matched by values within an order of magnitude, then the Darcy-flow model could be considered appropriate for describing brine flow through halite.

All of the test teams interpreting the brine-inflow experiments concluded that the average permeability of the halite strata penetrated by the holes was between approximately 10^{-22} and 10^{-21} m^2. The EdM team identified a single value of specific capacitance, 6.7×10^{-11} Pa^{-1}, from fitting to the DBT13 brine-inflow data, and used that value to simulate the other brine-inflow tests. The RIVM team also used a single value of specific capacitance, 3.0×10^{-11} Pa^{-1}, to simulate both the brine-inflow and permeability experiments. The SNL team found individual values of specific capacitance from each of the brine-inflow experiments ranging from 2.6×10^{-12} to 3.9×10^{-9} Pa^{-1}. Specific capacitances on the order of 10^{-10} and 10^{-9} Pa^{-1} are inconsistent with the known constitutive properties of halite and are attributed to deformation, possibly ongoing, of the halite around the WIPP excavations.

The interpretations performed by the different teams have demonstrated that models based on Darcy's law are able to replicate the experimental results within reasonable and acceptable bounds. The interpretations presented in this report cannot be considered unique in terms of representing the only possible model that could fit the data, but neither do they provide motivation to look for an alternative model that might fit the data better. To the extent that the simulations differ from the experimental results, refinements of the basic Darcy-flow model are suggested, rather than replacement with a fundamentally different model.

5.2 Recommendations

The project teams had a number of recommendations intended to: (1) provide more mechanistically complete (or realistic) simulations of the experiments; (2) provide further assurance that Darcy-flow models are actually appropriate; and (3) improve experimental design to aid in distinguishing relevant mechanisms and parameters.

A view shared by all the project teams is the need for coupling of hydrologic and geomechanical models to represent accurately all of the mechanisms and processes contributing to the responses observed during the experiments. This coupled modeling would, ideally, serve to demonstrate that the deviations observed to date between the experimental data and the Darcy-flow simulations were caused by factors *in addition to* Darcy flow, and not by a failure of the Darcy-flow assumption.

The coupled modeling needs to be performed on two scales. First, modeling needs to be performed on the scale of the repository, or possibly panel or room, to simulate the effects on both the stress and pore-pressure fields of excavation. Changes in the permeability of the rock near the excavations could also be simulated during this phase of modeling, if necessary. This modeling would provide the boundary and initial conditions for the second scale of modeling, which would consist of simulation of the brine-inflow and permeability experiments.

No direct measurements of pore pressures are made in conjunction with the brine-inflow tests, but such measurements are made as an integral part of permeability tests also being conducted at the WIPP site (Beauheim et al., 1991, 1993). These pore-pressure measurements could be used in calibration of the coupled models.

The project teams noted that all of the experiments conducted at the WIPP site involved hydraulic gradients much greater than unity, whereas the natural gradients within the Salado Formation would be expected to be two or more orders of magnitude lower. Further substantiation of the Darcy-flow assumption might, therefore, be provided by laboratory experiments to determine whether there was some threshold hydraulic gradient in halite below which no flow would occur. The existence of such a threshold gradient would represent a contradiction of Darcy's law, or at least limit the conditions under which it was applicable. If a threshold gradient exists, calculations of brine inflow to WIPP excavations based on Darcy's law would overestimate the actual amount of inflow.

The project teams also had specific recommendations with respect to improving the design of the brine-inflow experiments, many of which had already been identified and implemented by SNL between the time the test-case data were transmitted to the project teams and the completion of the teams' analyses. To improve the small-scale brine-inflow experiments, recommendations were made to: (1) try to identify directly the individual layers that were and were not providing inflow to the boreholes; (2) test farther from the excavations where growth of the disturbed rock zone around the excavations would be unlikely to affect the tests; and (3) test only distinct intervals within boreholes, perhaps by casing all parts of the holes except those parts to be tested. The first of these recommendations had already been implemented. The second recommendation had been considered by SNL, but was not implemented because of the termination of the small-scale brine-inflow program. The third recommendation was not implemented for the same reason.

5.3 Conclusions

The WIPP 1 Test Case involved the identification of mechanisms controlling the flow of brine through halite. Data from small-scale brine-inflow experiments were used to test the applicability of flow models based on Darcy's law, in which the rate of brine flow is directly proportional to the hydraulic gradient present. All project teams found that Darcy-flow models could replicate the experimental data in a consistent and reasonable manner. Discrepancies between the data and simulations are attributed to inadequate representation in the models of processes modifying the pore-pressure field in addition to the experiments themselves, such as ongoing deformation of the rock around the excavations. Therefore, the conclusion from the test case is that Darcy-flow models can reliably be used to predict brine flow to WIPP excavations, provided that the flow modeling is coupled with measurement and realistic modeling of the pore-pressure field around the excavations. This realistic modeling of the pore-pressure field would probably require coupling to a geomechanical model of the stress evolution around the repository.

6. REFERENCES

Aït-Chalal, A., S.-M. Tijani, and G. Vouille. 1993. *Modelling of the Small Scale Brine-Inflow Experiments.* R 93/6. Paris, France: École Nationale Supérieure des Mines de Paris. (Copy on file in the Sandia WIPP Central Files, Sandia National Laboratories, Albuquerque, NM as WPO#38850.)

Beauheim, R.L., G.J. Saulnier, Jr., and J.D. Avis. 1991. *Interpretation of Brine-Permeability Tests of the Salado Formation at the Waste Isolation Pilot Plant Site: First Interim Report.* SAND90-0083. Albuquerque, NM: Sandia National Laboratories.

Beauheim, R.L., R.M. Roberts, T.F. Dale, M.D. Fort, and W.A. Stensrud. 1993. *Hydraulic Testing of Salado Formation Evaporites at the Waste Isolation Pilot Plant Site: Second Interpretive Report.* SAND92-0533. Albuquerque, NM: Sandia National Laboratories.

Deal, D.E., J.B. Case, R.M. Deshler, P.E. Drez, J. Myers, and J.R. Tyburski. 1987. *Brine Sampling and Evaluation Program Phase II Report.* DOE-WIPP-87-010. Carlsbad, NM: Westinghouse Electric Corporation.

Deal, D.E., R.J. Abitz, D.S. Belski, J.B. Case, M.E. Crawley, R.M. Deshler, P.E. Drez, C.A. Givens, R.B. King, B.A. Lauctes, J. Myers, S. Niou, J.M. Pietz, W.M. Roggenthen, J.R. Tyburski, and M.G. Wallace. 1989. *Brine Sampling and Evaluation Program - 1988 Report.* DOE-WIPP-89-015. Carlsbad, NM: U.S. Department of Energy, Waste Isolation Pilot Plant Project Office.

Domski, P.S., D.T. Upton, and R.L. Beauheim. 1996. *Hydraulic Testing Around Room Q: Evaluation of the Effects of Mining on the Hydraulic Properties of Salado Evaporites.* SAND96-0435. Albuquerque, NM: Sandia National Laboratories.

Finley, S.J., D.J. Hanson, and R. Parsons. 1992. *Small-Scale Brine Inflow Experiments—Data Report Through 6/6/91.* SAND91-1956. Albuquerque, NM: Sandia National Laboratories.

Freeze, G.A., T.L. Christian-Frear, and S.W. Webb. 1997. *Modeling Brine Inflow to Room Q: A Numerical Investigation of Flow Mechanisms.* SAND96-0561. Albuquerque, NM: Sandia National Laboratories.

Freeze, R.A., and J.A. Cherry. 1979. *Groundwater.* Englewood Cliffs, NJ: Prentice-Hall.

Gelbard, F. 1992. *Exact Analysis of a Two-Dimensional Model for Brine Flow to a Borehole in a Disturbed Rock Zone.* SAND92-1303. Albuquerque, NM: Sandia National Laboratories.

Hassanizadeh, S.M., G.M. van der Giessen, H. Holtman, and P.N. Mollema. 1994. *INTRAVAL Phase 2, Test Case WIPP-l: Modelling Brine Migration in Rock Salt.* Final Report 715206003. Bilthoven, The Netherlands: National Institute of Public Health and Environmental Protection. (Copy on file in the Sandia WIPP Central Files, Sandia National Laboratories, Albuquerque, NM as WPO#38849.)

Hills, R.G. 1987. *ESTIM: A Parameter Estimation Computer Program.* SAND87-7063. Albuquerque, NM: Sandia National Laboratories.

Howarth, S.M., E.W. Peterson, P.L. Lagus, K-H. Lie, S.J. Finley, and E.J. Nowak. 1991. "Interpretation of In-Situ Pressure and Flow Measurements of the Salado Formation at the Waste Isolation Pilot Plant," *Proceedings 1991 SPE Rocky Mountain Regional Meeting and Low-Permeability Reservoirs Symposium, Denver, CO, April 15-17, 1991.* SPE 21840; SAND90-2334C. Richardson, TX: Society of Petroleum Engineers. 355-369.

Jaeger, J.C. 1958. "The Measurement of Thermal Conductivity and Diffusivity with Cylindrical Probes," *Transactions, American Geophysical Union.* Vol. 39, no. 4, 708-710.

Jaeger, J.C., and M. Clarke. 1942-1943. "A Short Table of $\int_0^\infty \frac{e^{-xu^2}}{J_0^2(u) + Y_0^2(u)} \frac{du}{u}$," *Proceedings of the Royal Society of Edinburgh.* Vol. A61, pt. 11, 229-230.

Jensen, A.L., C.L. Howard, R.L. Jones, and T.P. Peterson. 1993a. *Room Q Data Report: Test Borehole Data from April 1989 through November 1993.* SAND92-1172. Albuquerque, NM: Sandia National Laboratories.

Jensen, A.L., R.L. Jones, E.N. Lorusso, and C.L. Howard. 1993b. *Large-Scale Brine Inflow Data Report for Room Q Prior to November 25, 1991.* SAND92-1173. Albuquerque, NM: Sandia National Laboratories.

Jones, C.L., M.E. Cooley, and G.O. Bachman. 1973. *Salt Deposits of Los Medaños Area, Eddy and Lea Counties, New Mexico.* USGS-4339-7. Denver, CO: U.S. Geological Survey.

Kaufmann, D.W., ed. 1960. *Sodium Chloride, the Production and Properties of Salt and Brine.* Monograph no. 145. Washington, DC: American Chemical Society.

Krieg, R.D. 1984. *Reference Stratigraphy and Rock Properties for the Waste Isolation Pilot Plant (WIPP) Project.* SAND83-1908. Albuquerque, NM: Sandia National Laboratories.

McTigue, D.F. 1993. *Permeability and Hydraulic Diffusivity of Waste Isolation Pilot Plant Repository Salt Inferred from Small-Scale Brine Inflow Experiments.* SAND92-1911. Albuquerque, NM: Sandia National Laboratories.

McTigue, D.F., S.J. Finley, and E.J. Nowak. 1989. "Brine Transport in Polycrystalline Salt: Field Measurements and Model Considerations," *Eos Transactions, American Geophysical Union.* Vol. 70, no. 43, 1111.

Nowak, E.J., and D.F. McTigue. 1987. *Interim Results of Brine Transport Studies in the Waste Isolation Pilot Plant (WIPP).* SAND87-0880. Albuquerque, NM: Sandia National Laboratories.

Nowak, E.J., D.F. McTigue, and R. Beraun. 1988. *Brine Inflow to WIPP Disposal Rooms: Data, Modeling, and Assessment.* SAND88-0112. Albuquerque, NM: Sandia National Laboratories.

Plischke, B. 1988. "Rock Engineering Software: A Survey of Computer Programs in Rock Mechanics Research and Engineering Practice," *International Journal of Rock Mechanics and Mining Sciences & Geomechanics Abstracts.* Vol. 25, no. 4, 183-251.

Rutherford, B. 1992. Appendix F: "Statistical Analysis of Brine Inflow Data," *Small-Scale Brine Inflow Experiments—Data Report Through 6/6/91.* S.J. Finley, D.J. Hanson, and R. Parsons. SAND91-1956. Albuquerque, NM: Sandia National Laboratories. F-1 through F-31.

Sauter, F.J. 1987. *User's Manual METROPOL, Mathematical Description.* RIVM Interim Report 728514002. Bilthoven, The Netherlands: National Institute of Public Health and Environmental Protection. (Copy on file in the Sandia WIPP Central Files, Sandia National Laboratories, Albuquerque, NM as WPO#40261.)

Sauter, F.J., A. Leijnse, and A.H.W. Beusen. 1993. *METROPOL User's Guide.* RIVM Report 725205003. Bilthoven, The Netherlands: National Institute of Public Health and Environmental Protection. (Copy on file in the Sandia WIPP Central Files, Sandia National Laboratories, Albuquerque, NM as WPO#41402.)

Stein, C.L., and K.M. Kimball. 1992. Appendix D: "Water Content and Insoluble Residue Analyses of WIPP Samples," *Small-Scale Brine Inflow Experiments -- Data Report Through 6/6/91.* S.J. Finley, D.J. Hanson, and R. Parsons. SAND91-1956. Albuquerque, NM: Sandia National Laboratories. D-1 through D-10.

Sumino, Y., and O.L. Anderson. 1984. "Elastic Constants of Minerals," *CRC Handbook of Physical Properties of Rocks.* Ed. R.S. Carmichael. Boca Raton, FL: CRC Press, Inc. Vol. III, 39-138.

Webb, S.W. 1992. *Brine Inflow Sensitivity Study for Waste Isolation Pilot Plant Boreholes: Results of One-Dimensional Simulations.* SAND91-2296. Albuquerque, NM: Sandia National Laboratories.

WIPP
UC721 - DISTRIBUTION LIST
SAND97-0788

Federal Agencies

US Department of Energy (4)
Office of Civilian Radioactive Waste Mgmt.
Attn: Deputy Director, RW-2
Acting Director, RW-10
Office of Human Resources & Admin.
Director, RW-30
Office of Program Mgmt. & Integ.
Director, RW-40
Office of Waste Accept., Stor., & Tran.
Forrestal Building
Washington, DC 20585

Attn: Project Director
Yucca Mountain Site Characterization Office
Director, RW-3
Office of Quality Assurance
P.O. Box 30307
Las Vegas, NV 89036-0307

US Department of Energy
Albuquerque Operations Office
Attn: National Atomic Museum Library
P.O. Box 5400
Albuquerque, NM 87185-5400

US Department of Energy
Research & Waste Management Division
Attn: Director
P.O. Box E
Oak Ridge, TN 37831

US Department of Energy (5)
Carlsbad Area Office
Attn: G. Dials
D. Galbraith
M. McFadden
R. Lark
J. A. Mewhinney
P.O. Box 3090
Carlsbad, NM 88221-3090

US Department of Energy
Office of Environmental Restoration and
Waste Management
Attn: M Frei, EM-30
Forrestal Building
Washington, DC 20585-0002

US Department of Energy (3)
Office of Environmental Restoration and
Waste Management -
Attn: J. Juri, EM-34, Trevion II
Washington, DC 20585-0002

US Department of Energy
Office of Environmental Restoration and
Waste Management
Attn: S. Schneider, EM-342, Trevion II
Washington, DC 20585-0002

US Department of Energy (2)
Office of Environment, Safety & Health
Attn: C. Borgstrom, EH-25
R. Pelletier, EH-231
Washington, DC 20585

US Department of Energy (2)
Idaho Operations Office
Fuel Processing & Waste Mgmt. Division
785 DOE Place
Idaho Falls, ID 83402

US Environmental Protection Agency (2)
Radiation Protection Programs
Attn: M. Oge
ANR-460
Washington, DC 20460

Boards

Defense Nuclear Facilities Safety Board
Attn: D. Winters
625 Indiana Ave. NW, Suite 700
Washington, DC 20004

Nuclear Waste Technical Review Board (2)
Attn: Chairman
J. L. Cohon
1100 Wilson Blvd., Suite 910
Arlington, VA 22209-2297

State Agencies

Attorney General of New Mexico
P.O. Drawer 1508
Santa Fe, NM 87504-1508

Environmental Evaluation Group (3)
Attn: Library
7007 Wyoming NE
Suite F-2
Albuquerque, NM 87109

NM Energy, Minerals, and Natural
Resources Department
Attn: Library
2040 S. Pacheco
Santa Fe, NM 87505

NM Environment Department (3)
Secretary of the Environment
Attn: Mark Weidler
1190 St. Francis Drive
Santa Fe, NM 87503-0968

NM Bureau of Mines & Mineral Resources
Socorro, NM 87801

Laboratories/Corporations

Battelle Pacific Northwest Laboratories
Battelle Blvd.
Richland, WA 99352

Los Alamos National Laboratory
Attn: B. Erdal, INC-12
P.O. Box 1663
Los Alamos, NM 87544

Golder Associates
Attn: T. W. Doe
4104 148th Avenue, NE
Redmond, WA 98052

INTERA, Inc. (3)
Attn: G. A. Freeze
P. S. Domski
R. M. Roberts
1650 University Blvd. NE. Suite 300
Albuquerque, NM 87102

INTERA, Inc. (2)
Attn: J. F. Pickens
9111 Research Blvd.
Austin, TX 78758

L. Lehman and Associates, Inc.
Attn: L. Lehman
1103 W. Burnsville Parkway
Suite 209
Minneapolis, MN 55337

Tech Reps, Inc. (3)
Attn: J. Chapman (1)
Loretta Robledo (2)
5000 Marble NE, Suite 222
Albuquerque, NM 87110

Westinghouse Electric Corporation (5)
Attn: Library
J. Epstein
J. Lee
B. A. Howard
R. Kehrman
P.O. Box 2078
Carlsbad, NM 88221

S. Cohen & Associates
Attn: Bill Thurber
1355 Beverly Road
McLean, VA 22101

National Academy of Sciences, WIPP Panel

Howard Adler
Oxyrase, Incorporated
7327 Oak Ridge Highway
Knoxville, TN 37931

Tom Kiess
Board of Radioactive Waste Management
GF456
2101 Constitution Ave.
Washington, DC 20418

Rodney C. Ewing
Department of Geology
University of New Mexico
Albuquerque, NM 87131

Charles Fairhurst
Department of Civil and Mineral Engineering
University of Minnesota
500 Pillsbury Dr. SE
Minneapolis, MN 55455-0220

B. John Garrick
PLG Incorporated
4590 MacArthur Blvd., Suite 400
Newport Beach, CA 92660-2027

Leonard F. Konikow
US Geological Survey
431 National Center
Reston, VA 22092

Carl A. Anderson, Director
Board of Radioactive Waste Management
National Research Council
HA 456
2101 Constitution Ave. NW
Washington, DC 20418

Christopher G. Whipple
ICF Kaiser Engineers
1800 Harrison St., 7th Floor
Oakland, CA 94612-3430

John O. Blomeke
720 Clubhouse Way
Knoxville, TN 37909

Sue B. Clark
University of Georgia
Savannah River Ecology Lab
P.O. Drawer E
Aiken, SC 29802

Konrad B. Krauskopf
Department of Geology
Stanford University
Stanford, CA 94305-2115

Della Roy
Pennsylvania State University
217 Materials Research Lab
Hastings Road
University Park, PA 16802

David A. Waite
CH_2 M Hill
P.O. Box 91500
Bellevue, WA 98009-2050

Thomas A. Zordon
Zordan Associates, Inc.
3807 Edinburg Drive
Murrysville, PA 15668

Universities

University of New Mexico
Geology Department
Attn: Library
141 Northrop Hall
Albuquerque, NM 87131

University of Washington
College of Ocean & Fishery Sciences
Attn: G. R. Heath
583 Henderson Hall, HN-15
Seattle, WA 98195

New Mexico Tech
Department of Geoscience -
Attn: J. Wilson
Socorro, NM 87801

Texas A&M University
Department of Geology
Attn: P. A. Domenico
College Station, TX 77843

University of Arizona
Department of Hydrology
Attn: S. P. Neuman
Tucson, AZ 85721

University of California
Lawrence Berkeley Laboratory
Earth Sciences Division
Attn: C. F. Tsang
1 Cyclotron Road
Berkeley, CA 94720

University of Kansas
Kansas Geological Survey
Attn: J. Butler
1930 Constant Ave.
Campus West
Lawrence, KS 66046

University of Wisconsin-Madison (2)
Department of Geology and Geophysics
Attn: M. P. Anderson
H. F. Wang
1215 W. Dayton St.
Madison, WI 53706

Libraries

Thomas Brannigan Library
Attn: D. Dresp
106 W. Hadley St.
Las Cruces, NM 88001

Government Publications Department
Zimmerman Library
University of New Mexico
Albuquerque, NM 87131

New Mexico Junior College
Pannell Library
Attn: R. Hill
Lovington Highway
Hobbs, NM 88240

New Mexico State Library
Attn: N. McCallan
325 Don Gaspar
Santa Fe, NM 87503

New Mexico Tech
Martin Speere Memorial Library
Campus Street
Socorro, NM 87810

WIPP Public Reading Room
Carlsbad Public Library
101 S. Halagueno St.
Carlsbad, NM 88220

Foreign Addresses

Atomic Energy of Canada, Ltd. (2)
Whiteshell Laboratories
Attn: B. Goodwin
C. Davison
Pinawa, Manitoba, CANADA R0E 1L0

Environment Canada
National Water Research Institute
Canada Centre for Inland Lakes
Attn: K. S. Novakowski
867 Lakeshore Road
P. O. Box 5050
Burlington, Ontario, CANADA L7R 4A6

Francois Chenevier (2)
ANDRA
Route de Panorama Robert Schumann
B. P. 38
92266 Fontenay-aux-Roses, Cedex
FRANCE

Claude Sombret
Centre d'Etudes Nucleaires de la Vallee Rhone
CEN/VALRHO
S.D.H.A. B.P. 171
30205 Bagnols-Sur-Ceze, FRANCE

Commissariat a L'Energie Atomique
Attn: D. Alexandre
Centre d'Etudes de Cadarache
13108 Saint Paul Les Durance Cedex
FRANCE

Bundesanstalt fur Geowissenschaften und
Rohstoffe (2)
Attn: M. Langer
K. Schelkes
Postfach 510 153
D-30631 Hannover, GERMANY

Bundesministerium fur Forschung und
Technologie
Postfach 200 706
5300 Bonn 2, GERMANY

Institut fur Tieflagerung
Attn: K. Kuhn
Theodor-Heuss-Strasse 4
D-3300 Braunschweig, GERMANY

Gesellschaft fur Anlagen und Reaktorsicherheit
(GRS) mbH (2)
Attn: B. Baltes
P. Bogorinski
Schwertnergasse 1
D-50667 Cologne, GERMANY

Shingo Tashiro
Japan Atomic Energy Research Institute
Tokai-Mura, Ibaraki-Ken, 319-11
JAPAN

Netherlands Energy Research Foundation ECN
Attn: J. Prij
3 Westerduinweg
P.O. Box 1
1755 ZG Petten
THE NETHERLANDS

Svensk Karnbransleforsorjning AB
Attn: F. Karlsson
Project KBS (Karnbranslesakerhet)
Box 5864
S-102 48 Stockholm, SWEDEN

Conterra AB
Attn: A. Winberg
Ogardesvagen 4
S-433 30 Partille, SWEDEN

OECD Nuclear Energy Agency
Attn: Jean-Pierre Olivier
Division of Radiation Protection
and Waste Management
38, Boulevard Suchet
75016 Paris, FRANCE

Utrecht University (3)
Institute of Earth Sciences
Attn: G. M. Van der Gissen
H. Holtman
P. N. Mollema
Budapestlaan 4
P. O. Box 80.021
3508 TA Utrecht, THE NETHERLANDS

GEOSIGMA AB
Attn: P. Andersson
P. O. Box 894
S-751 08 Uppsala, SWEDEN

Kemakta Konsult AB
Attn: L. Birgersson
Box 12655
S-112 93 Stockholm, SWEDEN

Statens Karnkraftinspektion
Attn: B. Dverstorp
S-106 58 Stockholm, SWEDEN

Nationale Genossenschaft fur die Lagerung
Radioaktiver Abfalle (2)
Attn: S. Vomvoris
P. Zuidema
Hardstrasse 73
CH-5430 Wettingen
SWITZERLAND

AEA Technology
Attn: J. H. Rees
D5W/29 Culham Laboratory
Abington, Oxfordshire OX14 3DB
UNITED KINGDOM

AEA Technology
Attn: W. R. Rodwell
044/A31 Winfrith Technical Centre
Dorchester, Dorset DT2 8DH
UNITED KINGDOM

AEA Technology
Attn: J. E. Tinson
B4244 Harwell Laboratory
Didcot, Oxfordshire OX11 ORA
UNITED KINGDOM

John Porter
AEA Decommissioning and Waste Management
B22, Windscale
Seascale
Cumbria, CA20 1PF
UNITED KINGDOM

Ecole des Mines de Paris –C.G.E. S. (3)
Attn: G. Vouille
A. Ait-Chalal
S-M. Tijani
35 rue Saint Honore
77305 Fontainebleau Cedex
FRANCE

Martin Put
Studiecentrum Voor Kernenergie
Centre d'Etude de l'Energie Nucleaire
SCK. CEN
Boeretang 200
B-2400 Mol, BELGIUM

Christine Brun-Yaba
Commissariat a l'Energie Atomique
Institut de Protection et de Surete Nucleaire
BP 6 DPEI
92265 Fontenay-aux-Roses Cedex
FRANCE

Laboratory for Soil and Groundwater Research
RIVM (2)
Attn: S. Majid Hassanizadeh
T. Leijnse
P. O. Box 1
3720 BA Bilthoven, THE NETHERLANDS

Others

D. W. Powers
HC 12
Box 87
Anthony, TX 79821

Internal

MS	Org.	
1324	6115	P. B. Davies
1320	6831	E. J. Nowak
1322	6121	J. R. Tillerson
1328	6849	D. R. Anderson
1328	6848	H. N. Jow
1335	6801	M. Chu
1341	6832	J. T. Holmes
1395	6800	L. Shephard
1395	6821	M. Marietta
1395	6841	V. H. Slaboszewicz
1324	6115	A. R. Lappin
1395	6821	K. W. Larson
1324	6115	R. L. Beauheim (5)
1324	6115	T. Christian-Frear
1330	6811	K. Hart (2)
1330	4415	NWM Library (20)
9018	8940-2	Central Technical Files
0899	4414	Technical Library (5)
0619	12690	Review and Approval Desk (2), For DOE/OSTI